Dipl.-Ing. Gernot Kapper, BSc

Impact of finite plasma collisionality on the current drive efficiency in tokamaks and stellarators

DOCTORAL THESIS

to achieve the university degree of

Doktor der technischen Wissenschaften

submitted to

Graz University of Technology

Supervisor

Ao.Univ.-Prof. Dipl.-Ing. Dr.phil. Martin Heyn

Institute of Theoretical and Computational Physics

Co-Supervisor

Ass.Prof. Dipl.-Ing. Dr.techn. Winfried Kernbichler

Graz, July 2017

AFFIDAVIT

I declare that I have authored this thesis independently, that I have not used other than the declared sources/resources, and that I have explicitly indicated all material which has been quoted either literally or by content from the sources used. The text document uploaded to TUGRAZonline is identical to the present doctoral thesis.

Date	Signature

Abstract

The cyclotron resonant interaction of electrons with incident radio-frequency waves is used to drive parallel plasma currents in tokamaks and stellarators for the control of the rotational transform profile. This method, which is referred to as electron cyclotron current drive (ECCD), is usually modeled for plasmas in the collisionless limit. While such models are sufficient at rather low collisionality, they might underestimate the current drive efficiency in more collisional plasmas likely to occur at high density experiments. In this thesis, the impact of finite collisionality effects on the current drive efficiency is studied using the code NEO-2 which solves the linearized gyrokinetic equation for neoclassical diffusion coefficients and for the generalized Spitzer function which acts as current drive efficiency in phase space. This code uses the full linearized Coulomb collision model including energy and momentum conservation and there are no simplifications pertinent to the 3D device geometry. In this work, NEO-2 has been upgraded for expansion of the solved distribution function via a set of arbitrary, differentiable basis functions which can be chosen to be well-suited for the specific kind of problem. In addition, a fully relativistic Coulomb collision model has been implemented and successfully benchmarked against an already existing code in the long mean free path regime.

The generalized Spitzer function for finite collisionality exhibits features which can not be expected from simplified collision models. A newly developed code interface allows for the usage of precomputed NEO-2 results as input to the ray-tracing code TRAVIS in order to perform ECCD simulations with the full Coulomb collision model. As first application of this code combination a high-mirror configuration of the optimized stellarator Wendelstein 7-X using a realistic set of plasma parameter profiles has been studied. A significant difference of the total driven current when compared to commonly used collisionless models is observed for various ECCD scenarii. This is of special interest because even a small amount of bootstrap current in Wendelstein 7-X has to be balanced by ECCD in order to preserve its island divertor configuration.

In addition, a numerical study of the mono-energetic bootstrap coefficient in the $1/\nu$ regime, which is relevant at low collisionalities and low radial electric fields, has been performed using the standard configuration of Wendelstein 7-X as an example. It has been demonstrated that the collisionless Shaing-Callen limit is not reached even for very low collisionalities. A study on the gradient driven distribution function is presented in order to explain this behavior.

Kurzfassung

Die resonante Wechselwirkung von Elektronen mit einfallenden Hochfrequenz-Wellen treibt einen parallelen Plasmastrom in Tokamaks und Stellaratoren, um das Sicherheitsfaktor-Profil zu kontrollieren. Diese Methode wird Elektronenzyklotronresonanz-Stromtrieb genannt (kurz ECCD) und wird üblicherweise für kollisionsfreie Plasmen modelliert. Während solche vereinfachten Modelle bei niedriger Kollisionalität ausreichend sind, kann jedoch die Stromtrieb-Effizienz bei höheren Kollisionalitäten, so wie sie zum Beispiel in Experimenten mit höheren Dichten auftreten, unterschätzt werden. In dieser Dissertation wird deshalb der Einfluss von kollisionalen Effekten auf die Stromtrieb-Effizienz ("verallgemeinerte Spitzerfunktion") mit Hilfe des Codes NEO-2, welcher die gyrokinetische Gleichung zur Berechnung von neoklassischen Diffusionskoeffizienten sowie zur Berechnung der verallgemeinerten Spitzerfunktion löst, untersucht. Dieser Code verwendet den vollen linearisierten Coulomb-Stoßoperator welcher sowohl impuls- als auch energieerhaltend ist. Weiters werden keine Vereinfachungen an der 3D-Torusgeometrie vorgenommen. Im Zuge dieser Arbeit wurde NEO-2 erweitert, um die gelöste Verteilungsfunktion mit beliebigen, differenzierbaren Basisfunktionen zu entwickeln, welche für das jeweilige Problem passend gewählt werden können. Zusätzlich wurde ein relativistischer Stoßoperator in NEO-2 implementiert und erfolgreich mit einem bereits bestehenden Code im kollisionsfreien Limit validiert.

Wie gezeigt wird, weist die direkt berechnete verallgemeinerte Spitzerfunktion Effekte auf, welche nicht durch Ergebnisse von vereinfachten Modellen erwartet werden können. Eine neu entwickelte Schnittstelle erlaubt die Verwendung dieser Ergebnisse im Raytracing-Code TRAVIS um ECCD-Simulationen mit dem vollen Kollisionsoperator durchzuführen. Als erste Anwendung dieser gekoppelten Codes wurde eine High-Mirror-Konfiguration von Wendelstein 7-X mit zugehörigen realistischen Plasmaparameter-Profilen untersucht. Es wird gezeigt, dass ein signifikanter Unterschied zu einem üblichen kollisionsfreien Modell besteht. Dieses Resultat ist aufgrund der Insel-Divertor-Konfiguration dieses Stellarators von besonderem Interesse, da bereits ein kleiner Bootstrap-Strom am Plasmarand mit ECCD ausbalanciert werden muss, um die Konfiguration nicht zu stören.

Weiters wurde eine numerische Studie des monoenergetischen Bootstrap-Koeffizienten im $1/\nu$-Regime, welches bei niedrigen Kollisionalitäten und niedrigen radialen elektrischen Feldern relevant ist, für eine Standardkonfiguration von Wendelstein 7-X durchgeführt. Es wird demonstriert, dass das kollisionsfreie Shaing-Callen-Limit auch nicht bei extrem niedrigen Kollisionalitäten erreicht wird. Dies wird mittels einer Studie der durch Gradienten getriebenen Verteilungsfunktion erklärt.

Acknowledgments

This work could not have been written without the support of a number of persons. First I would like to thank my supervisor Prof. Martin Heyn as well as my co-supervisor Prof. Winfried Kernbichler for their guidance through this thesis and for establishing such a good working atmosphere in this group. Furthermore, I would like to express my gratitude to Dr. Sergei Kasilov for sharing his expert knowledge and ideas with me as well as for his support at every stage of this thesis. Special thanks go to Dr. Nikolai Marushchenko and Dr. Yuriy Turkin from IPP Greifswald for the joint work and for taking part in a lot of discussions.

Next I am grateful to all my colleagues at this institute for the seamless collaboration during the last years. My special thanks go to my office colleague Andreas Martitsch who shared all his experience with me and for the good teamwork on joint projects, to Christopher Albert for the instructive time spent together at summer schools and conferences, and to our administrator Andreas Hirczy for supporting me in all kinds of computer problems.

I am deeply grateful to my parents Emmy and Franz as well as to my sister Tanja. Without them I would never be there where I am today. Finally, my deepest appreciation goes to my beloved Annemarie for her endless patience and support.

This work has been carried out within the framework of the EUROfusion Consortium and has received funding from the Euratom research and training programme 2014-2018 under grant agreement No 633053. The views and opinions expressed herein do not necessarily reflect those of the European Commission. The author gratefully acknowledges support from NAWI Graz. The computational results presented have been achieved in part using the Vienna Scientific Cluster (VSC). I also gratefully acknowledge funding from the KKKÖ at ÖAW for a project for the continuation of the PhD thesis.

Table of contents

---

1 Introduction **7**

2 Basic definitions and formulation of the numerical problem **11**

- 2.1 Basic definitions 13
  - 2.1.1 Kinetic equation 13
  - 2.1.2 Gyrokinetic equation 14
- 2.2 Current drive problem 24
  - 2.2.1 Introduction to NEO-2 24
  - 2.2.2 Reduction of dimensionality 25
  - 2.2.3 Generalized Spitzer function 26
  - 2.2.4 Removal of the nullspace 28
- 2.3 Matrix elements of the full linearized Coulomb collision operator 33
  - 2.3.1 Overview 33
  - 2.3.2 Linearization and discretization 33
  - 2.3.3 Differential part of the collision operator 37
  - 2.3.4 Integral part of the collision operator 40
  - 2.3.5 Sets of basis functions 48
- 2.4 Fully relativistic collision model 56
  - 2.4.1 Transition of matrix elements to the form of Braams and Karney 56
  - 2.4.2 Direct evaluation of the Beliaev and Budker collision term . . . 58

3 Solution of the generalized Spitzer problem with NEO-2 **61**

- 3.1 Distribution function for full linearized collision model 63

3.2 Parallelized precomputation of a profile 64
3.3 Reconstruction of the generalized Spitzer function in phase space . . . 68
3.4 Summary 70

4 Benchmarking and studies of asymptotical limits 71
4.1 Mono-energetic neoclassical transport coefficients in the $1/\nu$ regime . . 73
4.1.1 Diffusion and bootstrap coefficients, effective ripple and Shaing-Callen limit 73
4.1.2 Convergence of NEO-2 with and without adaptive grid 76
4.2 Benchmarking of the distribution function 77
4.2.1 Overview 77
4.2.2 Collisionless limit 77
4.2.3 High-collisionality limit 84
4.2.4 Finite collisionality 86
4.3 Benchmarking with relativistic collision operator 90

5 ECCD simulations for finite collisionality in Wendelstein 7-X 97
5.1 Introduction 99
5.2 Studies of the current drive efficiency 100
5.3 ECCD simulations with a ray-tracing procedure 103
5.3.1 Low and moderate density scenario - X2-mode 106
5.3.2 High density scenario - O2-mode 112
5.3.3 Current drive mechanisms 119
5.3.4 Influence of ECCD on iota at the plasma edge 119
5.3.5 Preliminary results with relativistic collision operator 120
5.4 Conclusion 121

6 Synopsis 123

A Trubnikov potentials for perturbed distribution function 129

B Interface documentation 135

Publications

In the course of this thesis a number of articles as well as contributions to conferences in form of proceedings and posters have been authored and co-authored. In the following, these publications are listed, where for each an abstract describing the individual author contributions is given.

Peer reviewed journal articles

- G. Kapper, S. V. Kasilov, W. Kernbichler, A. F. Martitsch, M. F. Heyn, N. B. Marushchenko, and Y. Turkin, "Electron cyclotron current drive simulations for finite collisionality plasmas in Wendelstein 7-X using the full linearized collision model", Physics of Plasmas **23**, 112511 (2016)

  Author contributions: G. Kapper drafted and wrote the manuscript and provided all results with supervision from W. Kernbichler, M. F. Heyn, and S. V. Kasilov. The main author G. Kapper upgraded the drift kinetic equation solver NEO-2 and developed an interface between NEO-2 and the ray-tracing code TRAVIS. G. Kapper together with A. F. Martitsch generalized the evaluation of the collision operator to arbitrary basis functions allowing for stable computation of the generalized Spitzer function up to velocities which are of interest in current drive simulations. S. V. Kasilov and W. Kernbichler are the developers of the original version of the code NEO-2. N. B. Marushchenko and Y. Turkin are the main developers of the used ray-tracing code TRAVIS, provided the used plasma parameter profiles and took part in discussions.

- W. Kernbichler, S. V. Kasilov, G. Kapper, A. F. Martitsch, V. V. Nemov, C. Albert, and M. F. Heyn, "Solution of drift kinetic equation in stellarators and tokamaks with broken symmetry using the code NEO-2", Plasma Physics and Controlled Fusion **58**, 104001 (2016)

  Author contributions: W. Kernbichler and S. V. Kasilov drafted and wrote the manuscript with contributions to the results section from G. Kapper (stellarator) and A. F. Martitsch (tokamak). W. Kernbichler and S. V. Kasilov provided the theoretical background for the Spitzer function and bootstrap current computations. V. V. Nemov, W. Kernbichler and S. V. Kasilov are the original developers of the code NEO, which is the basis of NEO-2 and is used here for benchmarking. S. V. Kasilov and W. Kernbichler are the developers of the original version of the code NEO-2. G. Kapper and W. Kernbichler have developed the code parallelization pertinent to the stellarator branch of NEO-2. A. F. Martitsch provided all modeling results and figures for the plasma rotation in tokamaks. G. Kapper provided all modeling results and figures for the Spitzer function and bootstrap current. C. G. Albert and M. F. Heyn provided results from a semi-analytical model based on a Hamiltonian approach.

- A. F. Martitsch, S. V. Kasilov, W. Kernbichler, G. Kapper, C. G. Albert, M. F. Heyn, H. M. Smith, E. Strumberger, S. Fietz, W. Suttrop, M. Landreman, the ASDEX Upgrade Team, and the EUROfusion MST1 Team, "Effect of 3D magnetic perturbations on the plasma rotation in ASDEX Upgrade", Plasma Physics and Controlled Fusion **58**, 074007 (2016)

  Author contributions: A. F. Martitsch drafted and wrote the manuscript in collaboration with S. V. Kasilov and W. Kernbichler. All code developments in NEO-2 for the specific computation of plasma rotation, all numerical results, an extensive literature study and a study of numerous analytical benchmarking cases were provided by A. F. Martitsch. S. V. Kasilov and W. Kernbichler are the developers of the original version of the code NEO-2. G. Kapper together with A. F. Martitsch generalized the evaluation of the collision operator to arbitrary basis functions. C. G. Albert and M. F. Heyn provided results from a semi-analytical model based on a Hamiltonian approach. S. Fietz, E. Strumberger, W. Suttrop, the ASDEX Upgrade Team and the EUROfusion MST1 Team provided experimental data and took part in discussions. H. M. Smith and M. Landreman provided results from their code SFINCS and took part in discussions.

- C. G. Albert, M. F. Heyn, G. Kapper, S. V. Kasilov, W. Kernbichler, and A. F. Martitsch, "Evaluation of toroidal torque by non-resonant magnetic perturbations in tokamaks for resonant transport regimes using a Hamiltonian approach", Physics of Plasmas **23**, 082515 (2016)

  Author contributions: C. G. Albert drafted and wrote the manuscript in collaboration with S. V. Kasilov and M. F. Heyn. Based on preliminary work by S. V. Kasilov, C. G. Albert formulated the Hamiltonian approach to quasilinear resonant NTV transport regimes under the guidance of S. V. Kasilov and M. F. Heyn and performed analytical validations against literature results. C. G. Albert developed the code NEO-RT for the semi-analytical evaluation of toroidal torque in quasilinear resonant transport regimes and provided all numerical results from the Hamiltonian approach. A. F. Martitsch provided all benchmark results from the quasilinear version of the code NEO-2 developed by A. F. Martitsch, S. V. Kasilov and W. Kernbichler, where a generalized evaluation of the collision operator based on hat functions as derived and implemented together with G. Kapper was applied to resolve the resonant behavior of the solution.

Conference proceedings

- G. Kapper, W. Kernbichler, S. V. Kasilov, and N. B. Marushchenko, "Modeling of electron cyclotron current drive for finite collisionality plasmas in Wendelstein 7-X", in 42nd EPS Conference on Plasma Physics, Vol. 39E (2015), P1.164

  Author contributions: G. Kapper wrote the manuscript with supervision from W. Kernbichler and S. V. Kasilov. The main author G. Kapper upgraded the code NEO-2 and developed an interface for using precomputed results of NEO-2 in the ray-tracing code TRAVIS, where a first application is presented. N. B. Marushchenko provided the results from TRAVIS and took part in discussions.

- C. G. Albert, M. F. Heyn, G. Kapper, S. V. Kasilov, W. Kernbichler, and A. F. Martitsch, "Hamiltonian approach for evaluation of toroidal torque from finite amplitude non-axisymmetric perturbations of a tokamak magnetic field in resonant transport regimes", in *43rd EPS Conference on Plasma Physics* (2016), P1.051

Author contributions: C. G. Albert drafted and wrote the manuscript in collaboration with S. V. Kasilov and M. F. Heyn. Based on preliminary work by S. V. Kasilov, C. G. Albert formulated the Hamiltonian approach to non-linear resonant NTV transport regimes under the guidance of S. V. Kasilov and M. F. Heyn and performed analytical validations against literature results. C. G. Albert extended the code NEO-RT to account for non-linear attenuation and provided all numerical results from the Hamiltonian approach. A. F. Martitsch provided support by results from the quasilinear version of the code NEO-2 developed by A. F. Martitsch, S. V. Kasilov and W. Kernbichler, where a generalized evaluation of the collision operator based on hat functions as derived and implemented together with G. Kapper was applied to resolve the resonant behavior of the solution.

- W. Kernbichler, G. Kapper, S. V. Kasilov, and N. B. Marushchenko, "Computation of the Spitzer function in stellarators and tokamaks with finite collisionality", EPJ Web of Conferences **87**, 01006 (2015)

  Author contributions: W. Kernbichler and S. V. Kasilov wrote the manuscript. G. Kapper contributed to the results section with results for the generalized Spitzer function in tokamaks and stellarators. N. B. Marushchenko provided the results from the ray-tracing code TRAVIS and took part in discussions.

Poster presentations

- G. Kapper, S. V. Kasilov, W. Kernbichler, A. F. Martitsch, and N. B. Marushchenko, "Impact of finite collisionality effects on electron cyclotron current drive in stellarators", in 20th International Stellarator-Heliotron Workshop (2015), P2S3–39

  Author contributions: G. Kapper created the poster with supervision from W. Kernbichler and S. V. Kasilov and provided all results from NEO-2. G. Kapper together with A. F. Martitsch generalized the evaluation of the collision operator to arbitrary basis functions, where first benchmarks are shown here. S. V. Kasilov and W. Kernbichler are the developers of the original version of the code NEO-2.

N. B. Marushchenko provided results from the ray-tracing code TRAVIS, provided the used plasma parameter profiles and took part in discussions.

- G. Kapper, W. Kernbichler, S. V. Kasilov, and N. B. Marushchenko, "Modeling of electron cyclotron current drive for finite collisionality plasmas in Wendelstein 7-X", in 42nd EPS Conference on Plasma Physics (2015), P1.164

  Author contributions: See conference proceeding G. Kapper, *et al*, 42nd Conference on Plasma Physics (2015), P1.164.

- G. Kapper, S. V. Kasilov, and W. Kernbichler, "Investigation of the Generalized Spitzer Function in Tokamaks and Stellarators", in 51st Culham Plasma Physics Summer School (2014)

  Author contributions: G. Kapper created the poster with supervision from W. Kernbichler and S. V. Kasilov, where all results from NEO-2 have been provided by G. Kapper.

- C. G. Albert, M. F. Heyn, G. Kapper, S. V. Kasilov, W. Kernbichler, and A. F. Martitsch, "Hamiltonian approach for evaluation of toroidal torque from finite amplitude non-axisymmetric perturbations of a tokamak magnetic field in resonant transport regimes", in 43rd EPS Conference on Plasma Physics (2016), P1.051

  Author contributions: See conference proceeding C. G. Albert, *et al*, 43rd EPS Conference on Plasma Physics (2016), P1.051.

- A. F. Martitsch, S. V. Kasilov, W. Kernbichler, G. Kapper, C. G. Albert, M. F. Heyn, E. Strumberger, S. Fietz, W. Suttrop, the ASDEX Upgrade Team, and the EUROfusion MST1 Team, "Effect of 3D magnetic perturbations on the plasma rotation in tokamaks", in 20th International Stellarator-Heliotron Workshop (2015), P1S1–2

  Author contributions: See A. F. Martitsch, *et al*, Plasma Physics and Controlled Fusion **58**, 074007 (2016).

- W. Kernbichler, S. V. Kasilov, and G. Kapper, "Computation of the Spitzer function in a stellarator", in Joint 19th ISHW and 16th RFP Workshop (2013)

  Author contributions: W. Kernbichler and S. V. Kasilov created the poster with contributions to the results section from G. Kapper.

Technical reports

- G. Kapper, W. Kernbichler, S. V. Kasilov, and N. B. Marushchenko, *Interface to the generalized Spitzer function computed by NEO-2*, Technical Report (EUROfusion, 2015)
- G. Kapper, S. V. Kasilov, W. Kernbichler, A. F. Martitsch, and N. B. Marushchenko, *Implementation of the fully relativistic full linearized Coulomb collision model in the code NEO-2 for ECCD modeling in tokamaks and stellarators with finite plasma collisionality*, Technical Report (EUROfusion, 2017)

Chapter 1

Introduction

The diversification of energy sources over the last century allowed for the supply of the steadily increasing energy demands of our modern civilization. Today, fossil energy carriers, such as coal, oil, and gas, are still accounting for the major part of the energy supply while inevitably associated with their carbon footprint. Apart from the ongoing development and expansion of renewable energies, such as solar-, hydro-, and wind-power, also a lot of progress has been made in nuclear fusion research in the last decades. Power production by this technology turns out to be a serious option for the future [8, 9].

Fusion power arises from the release of binding energy when two light atomic nuclei are joined so that one heavier nucleus is formed. The mass difference between fusing nuclei and resulting fusion products and the respective release of energy was first explained with help of a liquid-drop model as introduced by C. F. v. Weizsäcker [10]. The energy gained from these atomic nuclei reactions is by 6–7 orders of magnitude above typical values as known from chemical reactions which only take place in the electron shells [8]. Such fusion reactions require very high temperatures so that the repulsive Coulomb forces of the charged particles can be overcome. Therefore, the creation of fusion relevant conditions in experiments on earth are connected with the need for efficient confinement of high-temperature plasmas. In contrast to stars, where gravitational forces confine the particles, on earth the main approaches are inertial and magnetic confinement. In the latter, a plasma is confined by strong magnetic fields either in magnetic mirrors or in toroidal devices. The two most promising concepts of such toroidal devices are the tokamak and the stellarator. In tokamaks a strong toroidal magnetic field, which is created by external toroidal field coils, is superimposed with a weaker poloidal field. This poloidal field is the result of an inductive toroidal current driven by pulsed operation of an ohmic transformer built up with a central solenoid as a primary coil and the plasma itself as a secondary coil. Such ohmic transformers are typically absent in stellarators because the necessary property of the magnetic field to form nested magnetic flux surfaces is achieved with help of a complex external coil system. In both types of devices the magnetic field lines are twisted, where the strength of this twist is defined by the rotational transform. One approach to control the radial rotational transform profile balancing if necessary an average parallel plasma equilibrium current arising with increased plasma temperature ("bootstrap current") is the electron cyclotron current drive (ECCD). This method is based on current drive by the cyclotron resonant interaction of electrons with incident radio-frequency waves [11]. The resonance region of such microwaves depends on the local magnetic field module and is therefore well localized. The current drive efficiency in phase space is related to the generalized Spitzer function, which has been well studied in asymptotical collisionality limits, namely for the collisionless limit where the 2D bounce averaged equation is solved [12] and in the high-collisionality limit where the classical Spitzer function [13] can be applied. However, in contrast to the collisionless limit, for finite collisionality the generalized Spitzer function has a finite value in the trapped particle region of velocity space [14]. It is smaller than in the high-collisionality limit, and in addition, exhibits an offset in the passing region [15]. These features can qualitatively be reproduced by interpolation between asymptotical limits [16], while the generalized Spitzer function obtained from direct calculation in the case of finite collisionality shows a feature which can not be expected from such an interpolation. This feature, resulting from the combined action of the magnetic mirroring force and collisions, is due to the symmetric part of this function with respect to the parallel velocity and is absent in asymptotical collisionality limits. This part, which is localized in velocity space around the trapped-passing boundary in the long mean free path regime, is also responsible for the bootstrap effect. As shown analytically in Ref. 17 and demonstrated later numerically in Refs. 5, 7, 18, this symmetric part of the generalized Spitzer function can be used for current drive by waves with symmetric spectra in the parallel wave number.

In this thesis, the impact of finite collisionality effects on the current drive efficiency is investigated for tokamaks and stellarators. This study requires the solution of the linearized drift kinetic equation using the code NEO-2 [2], which is developed at the Institute of Theoretical and Computational Physics at TU Graz in cooperation with the Institute of Plasma Physics, National Science Center "Kharkov Institute of Physics and Technology". In addition to the computation of neoclassical transport coefficients, this code also computes the distribution functions pertinent to different drives. Of special interest here is the generalized Spitzer function, which is driven by the parallel electric field. NEO-2 makes no simplifications to the full linearized Coulomb collision operator including energy and momentum conservation or to the 3D toroidal device geometry of tokamaks and stellarators. With help of this code the velocity-dependent Spitzer function is studied in asymptotical collisionality limits as well as for the finite collisionality case for various spatial points and different particle velocities. In order to perform these studies the collision model of NEO-2 has been upgraded for a generalized basis function expansion of the solution using the Galerkin method based on discretization of the drift kinetic equation over the energy variable. This allows for representation of the generalized Spitzer function via a complete set of arbitrary, differentiable basis functions which can be chosen to be well-suited for this specific kind of problem. Moreover, the collision operator has been extended to the fully relativistic Coulomb collision model based on the work of Braams and Karney [19] as well as on the collision operator by Beliaev and Budker [20]. For both, the non-relativistic and the relativistic case, the NEO-2 results have been benchmarked against the fully relativistic code SYNCH, which computes the generalized Spitzer function in the long mean free path limit for general toroidal geometry [12].

In order to perform ECCD simulations using the full linearized Coulomb collision model, NEO-2 has been coupled via the adjoint technique [21] with the ray-tracing code TRAVIS [22], which has been developed at the Max Planck Institute for Plasma Physics (IPP Greifswald). Due to the high dimensionality of the current drive problem in stellarators, the NEO-2 results have to be precomputed and used as an input for TRAVIS with an interface which has been newly developed in the course of this thesis. Using this code combination, various launch scenarii are investigated for the large optimized stellarator Wendelstein 7-X [23]. This stellarator has been optimized for good MHD (Magnetohydrodynamic) stability, a small bootstrap current with improved neoclassical confinement [24], and improved confinement of fast ions. In future operation phases this low-shear device, which avoids low-order rational flux surfaces in the core, uses an island divertor configuration where a resonant surface is placed by intention at the plasma edge (see e.g. Ref. 25). ECCD provides a powerful tool for the precise control of this surface by influencing the radial rotational transform profile. For the configuration studied in this thesis, a significant difference between ECCD simulations using a simplified collision model and the full collision model is seen.

This thesis is structured as follows:

- Chapter 1 gives a brief introduction into nuclear fusion with magnetic confinement and into the motivation of this work.
- In Chapter 2 the numerical problem is formulated where the linearized drift kinetic equation is introduced and discretized over the energy variable with focus on the numerical evaluation of the matrix elements of the full linearized Coulomb collision operator.
- Chapter 3 introduces the precomputation scheme for the generalized Spitzer function for a given magnetic equilibrium and pertinent plasma parameter profiles with an upgraded version of NEO-2.
- In Chapter 4 benchmarks of the upgraded version of NEO-2 against analytical models in asymptotical collisionality limits are presented. For the finite collisionality regime the special features of the generalized Spitzer function are discussed. Furthermore, a study of the mono-energetic neoclassical transport coefficients in the $1/\nu$ regime is presented.
- In Chapter 5 electron cyclotron current drive simulations in Wendelstein 7-X with the code combination NEO-2/TRAVIS using the full linearized Coulomb collision operator are presented with a detailed discussion of the impact of finite collisionality effects on the current drive efficiency.
- Chapter 6 summarizes the results of this thesis and gives an outlook.
- In the appendix a basis function expansion of Trubnikov potentials for a non-Maxwellian distribution function is presented. Moreover, a technical description of the interface between the codes NEO-2 and TRAVIS is given.

Chapter 2

Basic definitions and formulation of the numerical problem

In this chapter the fundamental equation to be solved for neoclassical transport computations, namely the linearized drift kinetic equation, is introduced. Furthermore, a generalized derivation of the matrix elements of the full linearized Coulomb collision operator, which results from discretization of this operator over the energy variable, is presented. In Section 2.2 the current drive problem is discussed, where parts of the methods described herein have been published in the following peer reviewed journal article, however in this thesis they are described in more detail:

- G. Kapper, S. V. Kasilov, W. Kernbichler, A. F. Martitsch, M. F. Heyn, N. B. Marushchenko, and Y. Turkin, “Electron cyclotron current drive simulations for finite collisionality plasmas in Wendelstein 7-X using the full linearized collision model”, Physics of Plasmas **23**, 112511 (2016)

The derivation of the fully relativistic Coulomb collision operator as described in Section 2.4 has been published in an internal EUROfusion report and is here described in more detail:

- G. Kapper, S. V. Kasilov, W. Kernbichler, A. F. Martitsch, and N. B. Marushchenko, *Implementation of the fully relativistic full linearized Coulomb collision model in the code NEO-2 for ECCD modeling in tokamaks and stellarators with finite plasma collisionality*, Technical Report (EUROfusion, 2017)

Contents of this chapter

2.1 Basic definitions 13
  2.1.1 Kinetic equation 13
  2.1.2 Gyrokinetic equation 14
2.2 Current drive problem 24
  2.2.1 Introduction to NEO-2 24
  2.2.2 Reduction of dimensionality 25
  2.2.3 Generalized Spitzer function 26
  2.2.4 Removal of the nullspace 28
2.3 Matrix elements of the full linearized Coulomb collision operator 33
  2.3.1 Overview 33
  2.3.2 Linearization and discretization 33
  2.3.3 Differential part of the collision operator 37
  2.3.4 Integral part of the collision operator 40
  2.3.5 Sets of basis functions 48
2.4 Fully relativistic collision model 56
  2.4.1 Transition of matrix elements to the form of Braams and Karney 56
  2.4.2 Direct evaluation of the Beliaev and Budker collision term . . . 58

2.1 Basic definitions

2.1.1 Kinetic equation

Following the book of Helander and Sigmar [26] an introduction to the plasma kinetic equation is given in this section. In general, a plasma is a gas consisting of many charged particles of different species fulfilling the quasi neutrality condition. Each particle of a specific species can be described by a point in a 6D phase space, represented by the distribution function $f_a(\mathbf{z}, t)$ with t being the time and $\mathbf{z} = (\mathbf{r}, \mathbf{v})$ being a phase space coordinate, where $\mathbf{r}$ is the radius vector and $\mathbf{v}$ is the velocity vector. For the description of transport processes, the time evolution of this function is of interest,

$$\frac{\mathrm{d}}{\mathrm{d}t} f_a(\mathbf{z}, t) = 0, \tag{2.1}$$

where the right hand side is zero because of particle conservation in phase space. The total time derivative is given by

$$\frac{\mathrm{d}}{\mathrm{d}t} f_a(\mathbf{z}, t) = \frac{\partial f_a}{\partial t} + \nabla_{\mathbf{z}} \cdot (\dot{\mathbf{z}} f_a) = \frac{\partial f_a}{\partial t} + f_a(\nabla_{\mathbf{z}} \cdot \dot{\mathbf{z}}) + \mathbf{z} \cdot (\nabla_{\mathbf{z}} f_a), \tag{2.2}$$

where $\nabla_{\mathbf{z}} = \partial/\partial\mathbf{z}$. According to Liouville's theorem the phase space flow velocity is divergence free, what can also be seen from Hamilton's equation [26, 27]. Thus, the kinetic equation is simplified to

$$\frac{\partial f_a}{\partial t} + \dot{\mathbf{z}} \cdot (\nabla_{\mathbf{z}} f_a) = 0. \tag{2.3}$$

The interaction of charged particles with electric and magnetic fields is described by the Lorentz force,

$$\ddot{\mathbf{r}} = \frac{e_a}{m_a}(\mathbf{E} + \frac{1}{c}\mathbf{v} \times \mathbf{B}), \tag{2.4}$$

with e_a being the particle charge, m_a the particle mass, $\mathbf{E}$ the total electric field, $\mathbf{B}$ the total magnetic field, and c the speed of light. Using Eq. (2.4) in the kinetic equation (2.3) the collisionless Vlasov equation is obtained,

$$\frac{\partial f_a}{\partial t} + \mathbf{v} \cdot (\nabla_{\mathbf{r}} f_a) + \frac{e_a}{m_a}(\mathbf{E} + \frac{1}{c}\mathbf{v} \times \mathbf{B}) \cdot (\nabla_{\mathbf{v}} f_a) = 0, \tag{2.5}$$

where $\mathbf{v} = \dot{\mathbf{r}}$ and $\nabla_{\mathbf{v}} = \partial/\partial\mathbf{v}$ as well as $\nabla_{\mathbf{r}} = \partial/\partial\mathbf{r}$ have been used.

The electric and magnetic fields strongly fluctuate due to the interaction with other charged particles within the Debye sphere. The so-called Debye sphere originates in a plasma due to shielding of charged particles by a surrounding cloud of particles with opposite charge (see e.g. Ref. 8). The radius of this sphere is called Debye length and defines the distance until the electric potential is decreased to the factor $1/e$. Introducing the fields $\overline{\mathbf{E}}$ and $\overline{\mathbf{B}}$, which are mean values of $\mathbf{E}$ and $\mathbf{B}$ over many Debye lengths, respectively, the mentioned fluctuations of the fields due to Coulomb collisions can be shifted to the right hand side of the equation as follows,

$$\frac{\partial f_a}{\partial t} + \mathbf{v} \cdot (\nabla_{\mathbf{r}} f_a) + \frac{e_a}{m_a}(\overline{\mathbf{E}} + \frac{1}{c}\mathbf{v} \times \overline{\mathbf{B}}) \cdot (\nabla_{\mathbf{v}} f_a) = \mathcal{C}_a(f_a), \tag{2.6}$$

so that $\mathcal{C}_a(f_a)$ is a collision term. The Coulomb forces in plasmas are long-range forces so that particles typically are deflected by a cumulative sum of small angle deflections instead of a few large angle deflections. The collision operator $\mathcal{C}_a(f_a)$ in its Fokker-Planck form [28] only depends on the velocity components of the particles,

$$\mathcal{C}_a(f_a) = -\nabla_{\mathbf{v}} \cdot \mathbf{j}_a, \tag{2.7}$$

where

$$\mathbf{j}_a = \sum_b \mathbf{j}_{ab} \tag{2.8}$$

is a velocity space flux caused by collisions. Here, self-collisions of same species as well as collisions with particles of species b are considered. This flux can be written as a sum of friction force $\mathbf{F}_{ab}$ and a diffusion tensor $\mathbf{D}_{ab}$ as follows,

$$\mathbf{j}_{ab} = \frac{\mathbf{F}_{ab}}{m_a} f_a - \mathbf{D}_{ab} \cdot \nabla f_a. \tag{2.9}$$

2.1.2 Gyrokinetic equation

Guiding center variables

Since particles in strong magnetic fields are studied, it is useful to introduce a coordinate system, where the guiding center position of the gyrating particle,

$$\mathbf{r}_g = \mathbf{r} - \frac{1}{\omega_c}\mathbf{h} \times \mathbf{v}, \tag{2.10}$$

is used as spatial coordinate. Here,

$$\mathbf{h} = \frac{\mathbf{B}}{B} \tag{2.11}$$

is a normalized vector in the direction of the magnetic field line and

$$\omega_c = \frac{e_a B}{m_a c} \tag{2.12}$$

is the cyclotron frequency defined via the magnetic field module $B = |\mathbf{B}|$. The 6D phase space variable $\mathbf{z} = (\mathbf{r}_g, J_\perp, \phi, w)$ is now written in terms of the guiding center position $\mathbf{r}_g$, the perpendicular adiabatic invariant $J_\perp$, the gyrophase angle ϕ, and the total energy w [2]. The perpendicular adiabatic invariant is given by

$$J_\perp \approx \frac{m_a v_\perp^2}{2\omega_c}, \tag{2.13}$$

where $v_\perp$ is the perpendicular velocity with respect to the magnetic field line on which the guiding center is located. The total energy w consists of a kinetic and a potential energy term,

$$w = \frac{m_a v^2}{2} + e_a \Phi = \frac{m_a v_\perp^2}{2} + \frac{m_a v_\parallel^2}{2} + e_a \Phi, \tag{2.14}$$

with the parallel velocity $v_\parallel$, and the electrostatic potential Φ. For the guiding center position flux coordinates are introduced so that the field lines are straight lines. Then, the guiding center position $\mathbf{r}_g = \mathbf{r}_g(r, \vartheta, \varphi)$ is given in terms of the effective radius r, which is used here as a flux surface label, the poloidal angle ϑ, and the toroidal angle φ. The kinetic equation (2.3) including the collision term written in terms of this 6D coordinate system is given as follows,

$$\frac{\partial f_a}{\partial t} + v_g^r \frac{\partial f_a}{\partial r} + v_g^\vartheta \frac{\partial f_a}{\partial \vartheta} + v_g^\varphi \frac{\partial f_a}{\partial \varphi} + \dot{w} \frac{\partial f_a}{\partial w} + \dot{J}_\perp \frac{\partial f_a}{\partial J_\perp} + \dot{\phi} \frac{\partial f_a}{\partial \phi} = \mathcal{C}_a(f_a), \tag{2.15}$$

where

$$v_g^r = \dot{\mathbf{r}}_g \cdot \nabla r, \tag{2.16}$$

$$v_g^\vartheta = \dot{\mathbf{r}}_g \cdot \nabla \vartheta, \tag{2.17}$$

$$v_g^\varphi = \dot{\mathbf{r}}_g \cdot \nabla \varphi, \tag{2.18}$$

are the contra-variant components of the guiding center velocity v_g. The high dimensionality of Eq. (2.15) can be simplified by neglecting terms which are orders of magnitude smaller than others what has been extensively studied in Ref. 29 using a variational principle and is discussed in the following section. In addition, it is shown that $J_\perp$ is indeed an adiabatic invariant what further simplifies the equation.

Equations of motion in guiding center variables

The derivations presented in this section follow the variational principle of Littlejohn [29]. Adaptions of the form of Littlejohn with respect to the coordinate system used here are discussed in the thesis of P. Leitner [30] for static fields and in the thesis of A. F. Martitsch [31] for time-dependent fields. Littlejohn presented in his work equations of the guiding center motion using an ordering parameter,

$$\epsilon \sim \frac{\rho_L}{L}, \tag{2.19}$$

which is proportional to the ratio of the Larmor radius ρ_L to characteristic scale lengths L. This ordering parameter is an artificial parameter to indicate the magnitude of a term, however, for physical results the parameter is set to unity. The Lagrangian for the guiding center motion is given here up to the first power in the ordering parameter ϵ by

$$\mathcal{L}(\mathbf{z}, \epsilon t) = \epsilon^{-1} \frac{e_a}{c} \mathbf{A}(\mathbf{r}_g, \epsilon t) \cdot \dot{\mathbf{r}}_g + m_a v_\parallel(\mathbf{z}, \epsilon t) \mathbf{h}(\mathbf{r}_g, \epsilon t) \cdot \dot{\mathbf{r}}_g - \epsilon J_\perp \dot{\phi} - w, \tag{2.20}$$

where $\mathbf{A} = \mathbf{A}(\mathbf{r}_g, \epsilon t) = \mathbf{A}(\mathbf{r}_g, \tau)$, with $\tau = \epsilon t$, is a weakly on time depending vector potential. For compactness the variable

$$v_\parallel(\mathbf{z}, \epsilon t) = \sigma \sqrt{\frac{2}{m_a}(w - e\Phi(\mathbf{r}_g, \epsilon t) - J_\perp \omega_c(\mathbf{r}_g, \epsilon t))} \tag{2.21}$$

has been introduced, however, it should be noted that $v_\parallel$ is not an independent variable. Here, the parallel velocity sign is given by $\sigma = \mathrm{sign}(v_\parallel)$. This Lagrangian is slightly different from Littlejohn [29] because here cgs units have been introduced and the total energy w is used as an independent variable instead of the parallel velocity $v_\parallel$ [30, 31]. The Euler-Lagrange equation

$$\frac{\mathrm{d}}{\mathrm{d}t}\left(\frac{\partial \mathcal{L}}{\partial \dot{z}_i}\right) = \frac{\partial \mathcal{L}}{\partial z_i} \tag{2.22}$$

is evaluated in the following for each component z_i with $i = 1, ..., 6$ of the phase space variable $\mathbf{z}$. Evaluating explicitly the left and right hand side of Eq. (2.22) for $z_i = w$ gives

$$\frac{\mathrm{d}}{\mathrm{d}t}\left(\frac{\partial \mathcal{L}}{\partial \dot{w}}\right) = 0, \tag{2.23}$$

and

$$\begin{aligned}\frac{\partial \mathcal{L}}{\partial w} &= \frac{m_a \sigma}{2}\left(\frac{2}{m_a}(w - e\Phi(\mathbf{r}_g, \epsilon t) - J_\perp \omega_c(\mathbf{r}_g, \epsilon t))\right)^{-1/2}\left(\frac{2}{m_a}\right)\mathbf{h}(\mathbf{r}_g, \epsilon t)\cdot \dot{\mathbf{r}}_g - 1 \\ &= \frac{\mathbf{h}(\mathbf{r}_g, \epsilon t)\cdot \dot{\mathbf{r}}_g}{v_\parallel(\mathbf{z}, \epsilon t)} - 1,\end{aligned} \tag{2.24}$$

respectively, where $\sigma^2 = 1$ has been used. Finally, Eq. (2.22) for $z_i = w$ results in

$$v_\parallel = \mathbf{h}\cdot \dot{\mathbf{r}}_g, \tag{2.25}$$

showing that the projection of the guiding center velocity on the field line vector is the parallel velocity. Performing the same steps for the perpendicular adiabatic invariant $z_i = J_\perp$ results in

$$\frac{\mathrm{d}}{\mathrm{d}t}\left(\frac{\partial \mathcal{L}}{\partial \dot{J}_\perp}\right) = 0, \tag{2.26}$$

and

$$\begin{aligned}\frac{\partial \mathcal{L}}{\partial J_\perp} &= \frac{m_a \sigma}{2}\left(\frac{2}{m_a}(w - e\Phi(\mathbf{r}_g, \epsilon t) - J_\perp \omega_c(\mathbf{r}_g, \epsilon t))\right)^{-1/2}\left(\frac{-2\omega_c(\mathbf{r}_g, \epsilon t)}{m_a}\right)\mathbf{h}(\mathbf{r}_g, \epsilon t)\cdot \dot{\mathbf{r}}_g - \epsilon\dot{\phi} \\ &= -\omega_c(\mathbf{r}_g, \epsilon t) - \epsilon\dot{\phi},\end{aligned} \tag{2.27}$$

where Eq. (2.25) has been used. Combination of these results gives an expression for the time evolution of the gyrophase angle,

$$\dot{\phi} = -\epsilon^{-1}\omega_c. \tag{2.28}$$

Recapitulating that $\epsilon \ll 1$, this result implies that the gyromotion acts on a very small time scale. This will be used later to justify averaging of the whole kinetic equation over the gyrophase. For $z_i = \phi$ the left and right hand sides of Eq. (2.22) are

$$\frac{\mathrm{d}}{\mathrm{d}t}\left(\frac{\partial \mathcal{L}}{\partial \dot{\phi}}\right) = -\epsilon\dot{J}_\perp, \tag{2.29}$$

and

$$\frac{\partial \mathcal{L}}{\partial \phi} = 0, \tag{2.30}$$

respectively, what results in

$$\dot{J}_\perp = 0, \tag{2.31}$$

showing that $J_\perp$ is indeed an adiabatic invariant.

For evaluating the Euler-Lagrange equation for the spatial coordinate components $z_{1,2,3} = \mathbf{r}_g$ it is important to notice that the fields $\mathbf{E} = \mathbf{E}(\mathbf{r}_g, \epsilon t)$, $\mathbf{B} = \mathbf{B}(\mathbf{r}_g, \epsilon t)$, and the potential $\Phi = \Phi(\mathbf{r}_g, \epsilon t)$ depend on the spatial position as well as weakly on time. The left hand side of Eq. (2.22) evaluates to

$$\begin{aligned}\frac{\mathrm{d}}{\mathrm{d}t}\left(\frac{\partial \mathcal{L}}{\partial \dot{\mathbf{r}}_g}\right) &= \frac{\mathrm{d}}{\mathrm{d}t}\Big(\epsilon^{-1}\frac{e_a}{c}\mathbf{A}(\mathbf{r}_g, \epsilon t) + m_a v_\parallel(\mathbf{z}, \epsilon t)\mathbf{h}(\mathbf{r}_g, \epsilon t)\Big) \\ &= \frac{e_a}{c}\left(\frac{\partial}{\partial \tau}\mathbf{A}(\mathbf{r}_g, \tau) + \epsilon^{-1}(\dot{\mathbf{r}}_g \cdot \nabla)\mathbf{A}(\mathbf{r}_g, \epsilon t)\right) + m_a \dot{v}_\parallel(\mathbf{z}, \epsilon t)\mathbf{h}(\mathbf{r}_g, \epsilon t) + \\ &\quad + m_a v_\parallel(\mathbf{z}, \epsilon t)\left(\epsilon\frac{\partial \mathbf{h}(\mathbf{r}_g, \tau)}{\partial \tau} + (\dot{\mathbf{r}}_g \cdot \nabla)\mathbf{h}(\mathbf{r}_g, \epsilon t)\right),\end{aligned} \tag{2.32}$$

where the Nabla operator $\nabla = \partial/\partial \mathbf{r}_g$ only acts on the guiding center position. Evaluating explicitly the right hand side of Eq. (2.22) results in

$$\begin{aligned}\frac{\partial \mathcal{L}}{\partial \mathbf{r}_g} &= \epsilon^{-1}\frac{e_a}{c}\dot{\mathbf{r}}_g \cdot (\nabla \mathbf{A}(\mathbf{r}_g, \epsilon t)) + m_a v_\parallel(\mathbf{z}, \epsilon t)\dot{\mathbf{r}}_g \cdot (\nabla \mathbf{h}(\mathbf{r}_g, \epsilon t)) + m_a(\dot{\mathbf{r}}_g \cdot \mathbf{h}(\mathbf{r}_g, \epsilon t))\nabla v_\parallel(\mathbf{r}_g, t) \\ &= \epsilon^{-1}\frac{e_a}{c}\dot{\mathbf{r}}_g \cdot (\nabla \mathbf{A}(\mathbf{r}_g, \epsilon t)) + m_a v_\parallel(\mathbf{z}, \epsilon t)\dot{\mathbf{r}}_g \cdot (\nabla \mathbf{h}(\mathbf{r}_g, \epsilon t)) - (e_a \nabla \Phi(\mathbf{r}_g, \epsilon t) + J_\perp \nabla \omega_c(\mathbf{r}_g, \epsilon t)) \\ &= \epsilon^{-1}\frac{e_a}{c}\Big((\dot{\mathbf{r}}_g \cdot \nabla)\mathbf{A}(\mathbf{r}_g, \epsilon t) + \dot{\mathbf{r}}_g \times (\nabla \times \mathbf{A}(\mathbf{r}_g, \epsilon t))\Big) + m_a v_\parallel(\mathbf{z}, \epsilon t)\Big((\dot{\mathbf{r}}_g \cdot \nabla)\mathbf{h}(\mathbf{r}_g, \epsilon t) + \\ &\quad + \dot{\mathbf{r}}_g \times (\nabla \times \mathbf{h}(\mathbf{r}_g, \epsilon t))\Big) - (e_a \nabla \Phi(\mathbf{r}_g, \epsilon t) + J_\perp \nabla \omega_c(\mathbf{r}_g, \epsilon t)).\end{aligned} \tag{2.33}$$

Here the relations

$$\begin{aligned}&\nabla v_\parallel(\mathbf{z}, \epsilon t) = -\frac{1}{v_\parallel(\mathbf{z}, \epsilon t) m_a}\left(e_a \nabla \Phi(\mathbf{r}_g, \epsilon t) + J_\perp \nabla \omega_c(\mathbf{r}_g, \epsilon t)\right), \\ &\dot{\mathbf{r}}_g \times (\nabla \times \mathbf{h}(\mathbf{r}_g, \epsilon t)) = \dot{\mathbf{r}}_g \cdot (\nabla \mathbf{h}(\mathbf{r}_g, \epsilon t)) - (\dot{\mathbf{r}}_g \cdot \nabla)\mathbf{h}(\mathbf{r}_g, \epsilon t), \\ &\dot{\mathbf{r}}_g \times (\nabla \times \mathbf{A}(\mathbf{r}_g, \epsilon t)) = \dot{\mathbf{r}}_g \cdot (\nabla \mathbf{A}(\mathbf{r}_g, \epsilon t)) - (\dot{\mathbf{r}}_g \cdot \nabla)\mathbf{A}(\mathbf{r}_g, \epsilon t),\end{aligned} \tag{2.34}$$

have been used (see e.g. the summary of vector identities in the book of D'Haeseleer [32]). Substitution of Eqs. (2.32) and (2.33) in (2.22) gives

$$\begin{aligned}
\frac{\mathrm{d}}{\mathrm{d}t}\left(\frac{\partial \mathcal{L}}{\partial \dot{\mathbf{r}}_g}\right) - \frac{\partial \mathcal{L}}{\partial \mathbf{r}_g} &= \frac{e_a}{c}\frac{\partial}{\partial \tau}\mathbf{A}(\mathbf{r}_g, \epsilon t) + m_a \dot{v}_\parallel(\mathbf{z}, \epsilon t)\mathbf{h}(\mathbf{r}_g, \epsilon t) + m_a v_\parallel(\mathbf{z}, \epsilon t)\epsilon \frac{\partial \mathbf{h}(\mathbf{r}_g, \tau)}{\partial \tau} - \\
&- \epsilon^{-1}\frac{e_a}{c}\dot{\mathbf{r}}_g \times (\nabla \times \mathbf{A}(\mathbf{r}_g, \epsilon t)) - m_a v_\parallel(\mathbf{z}, \epsilon t)(\dot{\mathbf{r}}_g \times (\nabla \times \mathbf{h}(\mathbf{r}_g, \epsilon t))) + \\
&+ e_a \nabla \Phi(\mathbf{r}_g, \epsilon t) + J_\perp \nabla \omega_c(\mathbf{r}_g, \epsilon t) \\
&= \frac{e_a}{c}\frac{\partial}{\partial \tau}\mathbf{A}(\mathbf{r}_g, \tau) + m_a \dot{v}_\parallel(\mathbf{z}, \epsilon t)\mathbf{h}(\mathbf{r}_g, \epsilon t) + m_a v_\parallel(\mathbf{z}, \epsilon t)\epsilon \frac{\partial \mathbf{h}(\mathbf{r}_g, \tau)}{\partial \tau} - \\
&- \epsilon^{-1}\frac{e_a}{c}\dot{\mathbf{r}}_g \times (\nabla \times \mathbf{A}^\star(\mathbf{r}_g, \epsilon t)) + m_a \dot{\mathbf{r}}_g \times (\nabla v_\parallel(\mathbf{z}, \epsilon t) \times \mathbf{h}(\mathbf{r}_g, \epsilon t)) + \\
&+ e_a \nabla \Phi(\mathbf{r}_g, \epsilon t) + J_\perp \nabla \omega_c(\mathbf{r}_g, \epsilon t) \\
&= \frac{e_a}{c}\frac{\partial}{\partial \tau}\mathbf{A}(\mathbf{r}_g, \tau) + m_a \dot{v}_\parallel(\mathbf{z}, \epsilon t)\mathbf{h}(\mathbf{r}_g, \epsilon t) + m_a v_\parallel(\mathbf{z}, \epsilon t)\epsilon \frac{\partial \mathbf{h}(\mathbf{r}_g, \tau)}{\partial \tau} - \\
&- \epsilon^{-1}\frac{e_a}{c}\dot{\mathbf{r}}_g \times \mathbf{B}^\star(\mathbf{r}_g, \epsilon t) + m_a \dot{\mathbf{r}}_g \times (\nabla v_\parallel(\mathbf{z}, \epsilon t) \times \mathbf{h}(\mathbf{r}_g, \epsilon t)) + \\
&+ e_a \nabla \Phi(\mathbf{r}_g, \epsilon t) + J_\perp \nabla \omega_c(\mathbf{r}_g, \epsilon t) = 0. \qquad (2.35)
\end{aligned}$$

In the equation above the product rule led to

$$\begin{aligned}
\dot{\mathbf{r}}_g \times (\nabla \times m_a v_\parallel(\mathbf{z}, \epsilon t)\mathbf{h}(\mathbf{r}_g, \epsilon t)) &= m_a v_\parallel(\mathbf{z}, \epsilon t)\dot{\mathbf{r}}_g \times (\nabla \times \mathbf{h}(\mathbf{r}_g, \epsilon t)) + \\
&+ m_a \dot{\mathbf{r}}_g \times (\nabla v_\parallel(\mathbf{z}, \epsilon t) \times \mathbf{h}(\mathbf{r}_g, \epsilon t)). \qquad (2.36)
\end{aligned}$$

In addition, the modified vector potential

$$\mathbf{A}^\star(\mathbf{r}_g, \epsilon t) = \mathbf{A}(\mathbf{r}_g, \epsilon t) + \epsilon \frac{m_a c}{e_a} v_\parallel(\mathbf{r}_g, t)\mathbf{h}(\mathbf{r}_g, \epsilon t), \qquad (2.37)$$

as well as the modified field

$$\mathbf{B}^\star(\mathbf{r}_g, \epsilon t) = \nabla \times \mathbf{A}^\star(\mathbf{r}_g, \epsilon t) = \mathbf{B}(\mathbf{r}_g, \epsilon t) + \epsilon \frac{m_a c}{e_a} \nabla \times v_\parallel(\mathbf{r}_g, t)\mathbf{h}(\mathbf{r}_g, \epsilon t) \qquad (2.38)$$

have been introduced [29, 33]. The fifth term of the last line of Eq. (2.35),

$$\begin{aligned}
m_a \dot{\mathbf{r}}_g \times (\nabla v_\parallel(\mathbf{z}, \epsilon t) \times \mathbf{h}(\mathbf{r}_g, \epsilon t)) = &- \nabla(e_a \Phi(\mathbf{r}_g, \epsilon t) + J_\perp \omega_c(\mathbf{r}_g, \epsilon t)) + \\
&+ \frac{\mathbf{h}(\mathbf{r}_g, \epsilon t)}{v_\parallel(\mathbf{z}, \epsilon t)}(\dot{\mathbf{r}}_g \cdot \nabla)(e_a \Phi(\mathbf{r}_g, \epsilon t) + J_\perp \omega_c(\mathbf{r}_g, \epsilon t)), \qquad (2.39)
\end{aligned}$$

is rewritten by application of the $\mathbf{B}(\mathbf{A}\cdot\mathbf{C})-\mathbf{C}(\mathbf{A}\cdot\mathbf{B})$ rule (see e.g. Ref. 32). Finally, Eq. (2.35) is cast to the following form,

$$\begin{aligned}&\frac{e_a}{c}\frac{\partial}{\partial\tau}\mathbf{A}(\mathbf{r}_g,\tau)+m_a\dot{v}_\parallel(\mathbf{z},\epsilon t)\mathbf{h}(\mathbf{r}_g,\epsilon t)+\epsilon m_a v_\parallel(\mathbf{z},\epsilon t)\frac{\partial\mathbf{h}(\mathbf{r}_g,\tau)}{\partial\tau}-\epsilon^{-1}\frac{e_a}{c}\dot{\mathbf{r}}_g\times\mathbf{B}^\star(\mathbf{r}_g,\epsilon t)\\&+\frac{\mathbf{h}(\mathbf{r}_g,\epsilon t)}{v_\parallel(\mathbf{z},\epsilon t)}(\dot{\mathbf{r}}_g\cdot\nabla)\left(e_a\Phi(\mathbf{r}_g,\epsilon t)+J_\perp\omega_c(\mathbf{r}_g,\epsilon t)\right)=0.\end{aligned}\tag{2.40}$$

Crossing this equation from the left with $\mathbf{h}$ results in

$$\begin{aligned}&\frac{e_a}{c}\mathbf{h}(\mathbf{r}_g,\epsilon t)\times\frac{\partial\mathbf{A}(\mathbf{r}_g,\tau)}{\partial\tau}+\epsilon m_a v_\parallel(\mathbf{z},\epsilon t)\mathbf{h}(\mathbf{r}_g,\epsilon t)\times\frac{\partial\mathbf{h}(\mathbf{r}_g,\tau)}{\partial\tau}-\\&-\epsilon^{-1}\frac{e_a}{c}\mathbf{h}(\mathbf{r}_g,\epsilon t)\times(\dot{\mathbf{r}}_g\times\mathbf{B}^\star(\mathbf{r}_g,\epsilon t))=0,\end{aligned}\tag{2.41}$$

and finally gives an equation of motion for the guiding center,

$$\dot{\mathbf{r}}_g=\mathbf{v}_g=v_\parallel\frac{\mathbf{B}^\star}{B_\parallel^\star}+\epsilon\frac{1}{B_\parallel^\star}\mathbf{h}\times\frac{\partial\mathbf{A}}{\partial\tau}+\mathcal{O}(\epsilon^2)\tag{2.42}$$

with $B_\parallel^\star=\mathbf{h}(\mathbf{r}_g,\epsilon t)\cdot\mathbf{B}^\star(\mathbf{r}_g,\epsilon t)$. In order to obtain an expression for the time evolution of the total energy, the Euler-Lagrange equation for the guiding center position (2.40) is scalar multiplied with $\dot{\mathbf{r}}_g$,

$$\begin{aligned}&\frac{e_a}{c}\dot{\mathbf{r}}_g\cdot\frac{\partial\mathbf{A}(\mathbf{r}_g,\tau)}{\partial\tau}+m_a\dot{v}_\parallel(\mathbf{z},\epsilon t)v_\parallel(\mathbf{z},\epsilon t)+\epsilon m_a v_\parallel(\mathbf{z},\epsilon t)\dot{\mathbf{r}}_g\cdot\frac{\partial\mathbf{h}(\mathbf{r}_g,\tau)}{\partial\tau}+\\&+(\dot{\mathbf{r}}_g\cdot\nabla)(e_a\Phi(\mathbf{r}_g,\epsilon t)+J_\perp\omega_c(\mathbf{r}_g,\epsilon t))=0,\end{aligned}\tag{2.43}$$

where $v_\parallel(\mathbf{z},\epsilon t)=\dot{\mathbf{r}}_g\cdot\mathbf{h}(\mathbf{r}_g,\epsilon t)$ was used. Explicit evaluation of the total time derivative of the parallel velocity (2.21) transforms the second term of this equation to

$$\begin{aligned}m_a\dot{v}_\parallel(\mathbf{z},\epsilon t)v_\parallel(\mathbf{z},\epsilon t)=\dot{w}-\epsilon e_a\frac{\partial\Phi(\mathbf{r}_g,\tau)}{\partial\tau}-e_a(\dot{\mathbf{r}}_g\cdot\nabla)\Phi(\mathbf{r}_g,\epsilon t)-\\-\epsilon J_\perp\frac{\partial\omega_c(\mathbf{r}_g,\tau)}{\partial\tau}-J_\perp(\dot{\mathbf{r}}_g\cdot\nabla)\omega_c(\mathbf{r}_g,\epsilon t).\end{aligned}\tag{2.44}$$

Thus, Eq. (2.43) can be transformed into an expression for the time evolution of the total energy,

$$\dot{w}=-\frac{e_a}{c}\dot{\mathbf{r}}_g\cdot\frac{\partial\mathbf{A}(\mathbf{r}_g,\tau)}{\partial\tau}+\mathcal{O}(\epsilon).\tag{2.45}$$

It has to be noted that for the case of static fields, the right hand side of Eq. (2.45) would vanish. The electric field can be expressed via the vector potential $\mathbf{A}$ and the electrostatic potential Φ as follows [26],

$$\mathbf{E}(\mathbf{r}_g, \epsilon t) = -\frac{1}{c}\frac{\partial \mathbf{A}(\mathbf{r}_g, \tau)}{\partial \tau} - \nabla\Phi(\mathbf{r}_g, \epsilon t) = \mathbf{E}^{(A)}(\mathbf{r}_g, \epsilon t) - \nabla\Phi(\mathbf{r}_g, \epsilon t), \tag{2.46}$$

transforming Eq. (2.45) in lowest order to

$$\dot{w} = e_a \dot{\mathbf{r}}_g \cdot \mathbf{E}^{(A)}(\mathbf{r}_g, \epsilon t), \tag{2.47}$$

where $\mathbf{E}^{(A)}$ is the inductive electric field. With the drift velocity (2.42) expressed in lowest order in ϵ,

$$\dot{\mathbf{r}}_g = v_\parallel(\mathbf{z}, \epsilon t)\mathbf{h}(\mathbf{r}_g, \epsilon t) + \mathcal{O}(\epsilon), \tag{2.48}$$

Eq. (2.47) can be rewritten as

$$\dot{w} = e_a v_\parallel E_\parallel \tag{2.49}$$

with the induced parallel electric field $E_\parallel = \mathbf{h} \cdot \mathbf{E}^{(A)}$.

Linearized gyrokinetic equation

The introduction of an ordering parameter ϵ is allowed when small gradients of density, temperature, fields, ... are assumed, which is valid in a typical fusion plasma. In such fusion plasmas, transport across magnetic flux surfaces is typically diffusive and can be described with a random walk model where the step size scales with the Larmor radius. A transport process is called diffusive when the step size is much smaller than macroscopic scale lengths (here gradient scale lengths). Diffusive transport is a slow phenomenon [26], therefore

$$\frac{\partial}{\partial t} \sim \epsilon^2 \nu, \tag{2.50}$$

where ν is a collision frequency. Therefore, the time derivatives in the kinetic equation (2.15) vanish, because they are of higher order than the other linearized terms.

The solution of the drift kinetic equation of lowest order is a local Maxwellian [34],

$$f_{a0} = f_{Ma}(r,w) = \frac{n_a}{\pi^{3/2} v_{Ta}^3} e^{-(w-e_a\Phi)/T_a}, \tag{2.51}$$

with the thermal velocity

$$v_{Ta} = \sqrt{\frac{2T_a}{m_a}}, \tag{2.52}$$

where n_a, m_a, and T_a are density, mass, and temperature, respectively. In the standard neoclassical ansatz the distribution function f_a is expanded in powers of ϵ, where for the linearized drift kinetic equation the series is truncated after the first power as follows,

$$f_a = f_{a0} + f_{a1}, \tag{2.53}$$

where f_{a1} is a small perturbation to the Maxwellian f_{a0} ($f_{a1} \ll f_{a0}$). Finally, using the equations of motion obtained by the variational principle in Eqs. (2.31) and (2.49), as well as the fact that $f_{a0} = f_{a0}(r,w)$ does not depend on the poloidal and toroidal angle, the kinetic equation (2.15) can be gyro-averaged and rewritten as,

$$v_g^\vartheta \frac{\partial f_{a1}}{\partial \vartheta} + v_g^\varphi \frac{\partial f_{a1}}{\partial \varphi} - \hat{L}_c f_{a1} = -v_g^r \frac{\partial f_{a0}}{\partial r} - e_a v_\parallel E_\parallel \frac{\partial f_{a0}}{\partial w}, \tag{2.54}$$

with $\hat{L}_c f_{a1}$ being the linearized collision operator as treated in Section 2.3. Due to the introduced ordering and the fact that diffusive transport is a slow phenomenon, $v_g^r \partial f_{a1}/\partial r$ as well as $\dot{w} \partial f_{a1}/\partial w$ are absent. The gyro-average of the kinetic equation as defined by

$$\langle F(\phi,\ldots)\rangle_\phi = \frac{1}{2\pi} \int\limits_0^{2\pi} \mathrm{d}\phi F(\phi,\ldots) \tag{2.55}$$

is meaningful because according to Eq. (2.28) the gyrophase evolves a lot faster in time ($\dot{\phi} \sim \epsilon^{-1}$) than the other terms. Due to the periodicity of the gyromotion, the term

$$\left\langle \dot{\phi} \frac{\partial f_a}{\partial \phi} \right\rangle_\phi = 0 \tag{2.56}$$

vanishes.

Thermodynamic forces

Following Ref. 2 the right hand side of Eq. (2.54) represents the total time derivative of a local Maxwellian, which can also be expressed as

$$\dot{f}_{a0} = -f_{a0} \sum_{k=1}^{3} q_k A_k + \frac{e_a f_{a0}}{T_a} v_{\parallel} \mathbf{h} \cdot \nabla \delta\Phi \tag{2.57}$$

introducing the thermodynamic forces

$$A_1 = \frac{1}{n_a}\frac{\partial n_a}{\partial r} - \frac{e_a E_r}{T_a} - \frac{3}{2T_a}\frac{\partial T_a}{\partial r}, \quad A_2 = \frac{1}{T_a}\frac{\partial T_a}{\partial r}, \quad A_3 = \frac{e_a \langle E_\parallel B \rangle}{T_a \langle B^2 \rangle}, \tag{2.58}$$

and the source terms

$$q_1 = -v_g^r, \qquad q_2 = -\frac{m_a v^2}{2T_a} v_g^r, \qquad q_3 = v_\parallel B. \tag{2.59}$$

Here, $\delta\Phi$ represents the fluctuation of the electrostatic potential and is the solution of the magnetic differential equation

$$\mathbf{h} \cdot \nabla \delta\Phi = B \frac{\langle E_\parallel B \rangle}{\langle B^2 \rangle} - E_\parallel \tag{2.60}$$

which also satisfies $\langle \delta\Phi \rangle = 0$. Multiplication of Eq. (2.60) with B and flux surface averaging shows that

$$\begin{aligned} \langle \mathbf{B} \cdot \nabla \delta\Phi \rangle =& \langle B^2 \rangle \frac{\langle E_\parallel B \rangle}{\langle B^2 \rangle} - \langle E_\parallel B \rangle \\ =& \langle E_\parallel B \rangle - \langle E_\parallel B \rangle \\ =& 0. \end{aligned} \tag{2.61}$$

The neoclassical flux surface average (average over the volume between neighboring flux surfaces) of a quantity F is defined as,

$$\langle F \rangle = \left(\int_{-\pi}^{\pi} \mathrm{d}\vartheta \int_{-\pi}^{\pi} \mathrm{d}\varphi \sqrt{g} \right)^{-1} \int_{-\pi}^{\pi} \mathrm{d}\vartheta \int_{-\pi}^{\pi} \mathrm{d}\varphi \sqrt{g} F \tag{2.62}$$

where $\sqrt{g}$ is the metric determinant. Definition of the operator

$$\hat{L} = v_g^{\vartheta} \frac{\partial}{\partial \vartheta} + v_g^{\varphi} \frac{\partial}{\partial \varphi} - \hat{L}_c \tag{2.63}$$

allows to recast the drift kinetic equation (2.54) in a compact notation as follows,

$$\hat{L} f_{a1} = -\dot{f}_{a0}. \tag{2.64}$$

According to Eq. (2.57), the perturbation f_{a1} can also be expanded using the thermodynamic forces,

$$f_{a1} = f_{a0} \sum_{k=1}^{3} g_k A_k - \frac{e_a \delta \Phi}{T_a} f_{a0}, \tag{2.65}$$

where g_k are solutions to

$$\hat{L} f_{a0} g_k = q_k f_{a0}. \tag{2.66}$$

The last term in (2.65) follows from the term with $\delta\Phi$ in (2.57) within the leading order in Larmor radius. The representation of f_{a1} in Eq. (2.65) via the thermodynamic forces is valid closed within a given species if the integral part of the collision operator for inter-species collisions is ignored (this is the case for the current drive problem). In the case of a multi-species problem, Eq. (2.55) has to be solved for each species, where the different species are coupled via the integral part of the collision operator. Then, the representation of f_{a1} for a given species a includes the thermodynamic forces of all species [2].

2.2 Current drive problem

2.2.1 Introduction to NEO-2

The code NEO-2, which is developed at the Institute of Theoretical and Computational Physics at TU Graz in cooperation with the Institute of Plasma Physics, National Science Center "Kharkov Institute of Physics and Technology", is a linearized drift kinetic equation solver for arbitrary 3D toroidal geometries. It has been developed for the computation of neoclassical transport coefficients and the generalized Spitzer function for plasmas with finite collisionality. It is therefore referred to as a finite collisionality extension to its predecessor NEO [35] which solves the drift kinetic kinetic equation in the $1/\nu$ regime where the cross-field rotation is negligible. Both codes use the field line integration technique as presented in Ref. 36. In contrast to codes which simplify the collision model for a particular collisionality regime, NEO-2 can use the full linearized Coulomb collision operator including energy and momentum conservation for a wide range of collisionalities. The dimensionality of the standard neoclassical transport problem is equal to four in stellarators and three in axisymmetric tokamaks. In application to the stellarator, NEO-2 is limited to the regimes with slow cross-field rotation. In these regimes the spatial dimensionality of the problem in stellarators can be further decreased by one, using the fact that each spatial point on a flux surface can be reached by tracing a field line which is long enough to densely cover the whole flux surface. This limitation of NEO-2 is not significant for applications of this code to the ECCD problem being the main topic of this thesis.

2.2.2 Reduction of dimensionality

This thesis is focused on the study of the generalized Spitzer function where the particle decorrelation due to cross-field drift is neglected because it has a small effect on the generalized Spitzer function in finite collisionality regimes as well as at low collisionalities where the electrons are mostly in the $1/\nu$ regime. This simplification on the drift kinetic equation is not an intrinsic limit of the solver NEO-2, which can treat plasma rotation in tokamaks with 3D magnetic perturbations if the perturbations are small enough to apply perturbation theory [31, 37].

If the guiding center position of a particle is traced along a magnetic field line, the position of the particle can be fully described by the radial position (flux surface label), the poloidal angle and a field line label $\varphi_0 = \varphi - q\vartheta$, where the safety factor $q = 1/\iota$ is the inverse of the rotational transform ι. The velocity space coordinates are now transformed from $(v_\parallel, v_\perp)$ to (v, η). Here, v is the velocity module, and

$$\eta = \frac{v_\perp^2}{v^2 B} = \frac{1 - \lambda^2}{B} \tag{2.67}$$

is the perpendicular adiabatic invariant, which can be defined by the pitch angle parameter $\lambda = v_\parallel / v$. Multiplication of Eq. (2.42) with $\nabla\vartheta$ gives in lowest order,

$$v_g^\vartheta = \frac{v_\parallel}{B_\parallel^\star} \mathbf{B}^\star \cdot \nabla\vartheta = v_\parallel h^\vartheta = v\lambda h^\vartheta \tag{2.68}$$

with h^ϑ being the contra-variant poloidal component of the unit vector along the magnetic field line. Using field aligned coordinates $(r, \vartheta, \varphi_0)$ as described above and Eq. (2.68), operator (2.63) takes the truncated integro-differential form,

$$\hat{L} \to \hat{L}_0 = v\lambda h^\vartheta \frac{\partial}{\partial\vartheta} - \hat{L}_C = v\lambda \frac{\partial}{\partial l} - \hat{L}_C, \tag{2.69}$$

where l is the distance counted along the field line and

$$\lambda = \sigma\sqrt{1 - \eta B}, \tag{2.70}$$

where σ is the parallel velocity sign. The problem

$$\hat{L}_0 f_M g_k = q_k f_M \tag{2.71}$$

is solved along a single field line which is long enough to densely cover the whole flux surface. It should be noted that operator (2.69) is written in terms of integrals of motion v and normalized perpendicular adiabatic invariant η which are conserved in zero order over the Larmor radius.

From Eq. (2.71) the current drive problem is obtained,

$$v\lambda h^\vartheta \frac{\partial}{\partial\vartheta} f_M g_3 - \hat{L}_C f_M g_3 = v_\parallel B f_M, \tag{2.72}$$

where only the source term representing the parallel flow $q_3 = v_\parallel B$ has to be considered. Here, g_3 is the distribution function driven by the parallel electric field.

2.2.3 Generalized Spitzer function

Eq. (2.72) is solved on a long enough field line, $0 < \vartheta < 2\pi\iota N_t$, where ι is the rotational transform and $N_t \gg 1$ is a number of toroidal periods large enough to cover the magnetic flux surface in a way allowing for a sufficiently accurate interpolation. The distribution function g_3 is related to the generalized Spitzer function g_{sp}, which is independent of collisionality in asymptotical limits, as follows,

$$g_{\mathrm{sp}} = \frac{1}{l_C B_{\mathrm{ref}}} g_3, \qquad l_C = \frac{T_e^2}{\pi n_e e^4 \ln \Lambda_{ee}}, \tag{2.73}$$

where l_C is the mean free path, B_{ref} is a reference magnetic field module, T_e is the electron temperature, n_e is the electron density, e is the electron charge, and $\ln \Lambda_{ee}$ is the Coulomb logarithm as defined in Ref. 38. The thermodynamic flux connected to the current drive problem is defined as,

$$I_3 = n_e \left\langle V_{e\|} B \right\rangle = - \left\langle \int \mathrm{d}^3 v q_3^\dagger \delta f_{\mathrm{RF}} \right\rangle, \tag{2.74}$$

where $V_{e\|}$ is the electron parallel flow velocity, $< \ldots >$ denotes neoclassical flux surface average (average over the volume between neighboring flux surfaces), the cross denotes an opposite parallel velocity sign, and the distribution function δf_{RF} is the solution to the linear current drive problem

$$\hat{L}_0 \delta f_{\mathrm{RF}} = Q_{\mathrm{RF}}, \tag{2.75}$$

where

$$Q_{\mathrm{RF}} = \hat{L}_{\mathrm{QL}} f_M = -\frac{1}{J} \frac{\partial}{\partial v^i} \left(J \Gamma^i_{\mathrm{RF}} \right) \tag{2.76}$$

is the quasilinear particle source in phase space due to the resonant interaction with radio-frequency waves, Γ^i_{RF} is the wave-induced quasilinear diffusion flux density, and $\hat{L}_{\mathrm{QL}}$ is the quasilinear diffusion operator acting on the local Maxwellian f_M. Here, a co- and contra-variant notation with respect to the velocity space components v^i is used, and J is the phase space Jacobian.

Using the same adjoint approach as in Ref. 21, the averaged parallel electron current density $j_{e\|}$ can be expressed as follows,

$$\begin{aligned}
\left\langle j_{e\|} B \right\rangle &= -e \left\langle \int \mathrm{d}^3 v q_3^\dagger \delta f_{\mathrm{RF}} \right\rangle \\
&= -e \left\langle \int \mathrm{d}^3 v \delta f_{\mathrm{RF}} f_M^{-1} (q_3^\dagger f_M) \right\rangle \\
&= -e \left\langle \int \mathrm{d}^3 v \delta f_{\mathrm{RF}} f_M^{-1} (\hat{L}_0^\dagger f_M g_3^\dagger) \right\rangle
\end{aligned}$$

$$= -e \left\langle \int \mathrm{d}^3 v g_3^\dagger \hat{L}_0 \delta f_{\mathrm{RF}} \right\rangle , \tag{2.77}$$

where $\hat{L}_0^\dagger f_M g_3^\dagger = q_3^\dagger f_M$ and the adjointness relation,

$$\left\langle \int \mathrm{d}^3 v G \hat{L}_0 f_M F \right\rangle = \left\langle \int \mathrm{d}^3 v F \hat{L}_0^\dagger f_M G \right\rangle , \tag{2.78}$$

was used. Finally, the parallel current density can be directly linked to the source term in Eq. (2.75),

$$\left\langle j_{e\parallel} B \right\rangle = -e l_C B_{\mathrm{ref}} \left\langle \int \mathrm{d}^3 v g_{\mathrm{sp}}^\dagger Q_{\mathrm{RF}} \right\rangle = -e l_C B_{\mathrm{ref}} \left\langle \int \mathrm{d}^3 v \frac{\partial g_{\mathrm{sp}}^\dagger}{\partial v^i} \Gamma_{\mathrm{RF}}^i \right\rangle , \tag{2.79}$$

where the adjoint generalized Spitzer function is expressed through the generalized Spitzer function (2.73) as follows, $g_{\mathrm{sp}}^\dagger(v_\parallel) = g_{\mathrm{sp}}(-v_\parallel)$.

2.2.4 Removal of the nullspace

Besides Eq. (2.72), function g_3 must satisfy two additional constraints which remove the nullspace of this equation,

$$\left\langle \int \mathrm{d}^3 v \; a_k f_M g_3 \right\rangle = 0, \tag{2.80}$$

where $k = 1, 2$ with $a_1 = 1$ and $a_2 = v^2$. This nullspace appears due to approximate particle conservation (cross-field transport is ignored in the kinetic equation) and energy conservation (energy is conserved within the electron component whose energy exchange with ions is ignored). In the following derivations, species index and source index are dropped for better readability. In general the direct current drive problem

$$\frac{\partial f}{\partial t} + v_\parallel \mathbf{h} \cdot \nabla f - \hat{L}_C f = Q \tag{2.81}$$

does not have a steady state solution. Integration of Eq. (2.81) with $\int \mathrm{d}^3 v a_k$ and subsequent flux surface average leads to

$$\frac{\partial}{\partial t} \left\langle \int \mathrm{d}^3 v a_k f \right\rangle = \left\langle \int \mathrm{d}^3 v a_k Q \right\rangle , \tag{2.82}$$

where the second term of (2.81) vanishes because $\nabla a = 0$, and the third term vanishes because of particle and energy conservation of the collision operator (a_1 corresponds to particle conservation where a_2 corresponds to energy conservation). Therefore, a steady state is only possible if the right hand side of Eq. (2.82) becomes zero,

$$\left\langle \int \mathrm{d}^3 v a_k Q \right\rangle = 0. \tag{2.83}$$

For a source of the form

$$\overline{Q} = (c_0 + c_2 v^2) f_M \tag{2.84}$$

with the constants c_0 and c_2 ($\nabla c_0 = \nabla c_2 = 0$), a solution to (2.82) is

$$\begin{aligned} \overline{f} &= (c_0 + c_2 v^2) f_M t \\ &= \overline{Q} t. \end{aligned} \tag{2.85}$$

If this solution is used in Eq. (2.81), then indeed $\mathbf{h} \cdot \nabla \overline{Q} = 0$ because $\mathbf{h} \cdot (\partial f_M / \partial r) \nabla r = 0$. Also $\hat{L}_C \overline{Q} = 0$ due to particle and energy conservation and so Eq. (2.85) satisfies Eq. (2.81). Function (2.85) produces no parallel current because it is an even function in $v_\parallel$. A steady state source can now be formed by

$$\widetilde{Q} = Q - \overline{Q}, \tag{2.86}$$

which also satisfies

$$\left\langle \int \mathrm{d}^3 v a_k \widetilde{Q} \right\rangle = 0. \tag{2.87}$$

Using Eq. (2.85) in Eq. (2.82) gives

$$\frac{\partial}{\partial t} \left\langle \int \mathrm{d}^3 v a_k (c_0 + c_2 v^2) f_M t \right\rangle = \left\langle \int \mathrm{d}^3 v a_k Q \right\rangle \tag{2.88}$$

what finally results in the following set of equations defining the constants c_0 and c_2,

$$\left\langle \int \mathrm{d}^3 v (c_0 + c_2 v^2) f_M \right\rangle = \left\langle \int \mathrm{d}^3 v Q \right\rangle, \tag{2.89}$$

$$\left\langle \int \mathrm{d}^3 v (c_0 v^2 + c_2 v^4) f_M \right\rangle = \left\langle \int \mathrm{d}^3 v v^2 Q \right\rangle . \tag{2.90}$$

Using the abbreviations

$$a_{00} = \left\langle \int \mathrm{d}^3 v f_M \right\rangle , \tag{2.91}$$

$$a_{02} = a_{20} = \left\langle \int \mathrm{d}^3 v v^2 f_M \right\rangle , \tag{2.92}$$

$$a_{22} = \left\langle \int \mathrm{d}^3 v v^4 f_M \right\rangle , \tag{2.93}$$

$$b_0 = \left\langle \int \mathrm{d}^3 v v Q \right\rangle , \tag{2.94}$$

$$b_2 = \left\langle \int \mathrm{d}^3 v v^2 Q \right\rangle , \tag{2.95}$$

the set of equations (2.89)–(2.90) can be written as,

$$a_{00} c_0 + a_{02} c_2 = b_0, \tag{2.96}$$

$$a_{20} c_0 + a_{22} c_2 = b_2, \tag{2.97}$$

with the solution

$$c_0 = \frac{a_{22} b_0 - a_{02} b_2}{a_{00} a_{22} - a_{02} a_{20}}, \tag{2.98}$$

$$c_2 = \frac{a_{20} b_0 - a_{00} b_2}{a_{02} a_{20} - a_{00} a_{22}}. \tag{2.99}$$

For a non-relativistic Maxwellian Eq. (2.91)–(2.93) can be evaluated analytically as follows,

$$a_{00} = n_0, \tag{2.100}$$

$$a_{02} = a_{20} = \frac{3}{2} n_0 v_T^2, \tag{2.101}$$

$$a_{22} = \frac{15}{4} n_0 v_T^4, \tag{2.102}$$

so that the constants can be expressed by

$$c_0 = \frac{5}{2n_0}\left\langle \int \mathrm{d}^3 v Q \right\rangle - \frac{1}{n_0}\left\langle \int \mathrm{d}^3 v \left(\frac{v}{v_T}\right)^2 Q \right\rangle, \tag{2.103}$$

$$c_2 = -\frac{1}{n_0 v_T^2}\left\langle \int \mathrm{d}^3 v Q \right\rangle + \frac{2}{3n_0 v_T^2}\left\langle \int \mathrm{d}^3 v \left(\frac{v}{v_T}\right)^2 Q \right\rangle. \tag{2.104}$$

Substitution of (2.103) and (2.104) in (2.84) allows to express the source term in integral form as follows,

$$\overline{Q} = \left\langle \int \mathrm{d}^3 v' K(v, v') Q \right\rangle, \tag{2.105}$$

where for reasons of readability the function

$$K(v, v') = \frac{1}{n_0} f_M(v) \left(\frac{5}{2} - \left(\frac{v}{v_T}\right)^2 - \left(\frac{v'}{v_T}\right)^2 + \frac{2}{3}\left(\frac{v}{v_T}\right)^2 \left(\frac{v'}{v_T}\right)^2\right) \tag{2.106}$$

has been introduced. Then, the steady state source is

$$\widetilde{Q} = Q - \overline{Q} = \left\langle \int \mathrm{d}^3 v' \mathit{\Pi}(\mathbf{r}, \mathbf{v}, \mathbf{r}', \mathbf{v}') Q \right\rangle', \tag{2.107}$$

where $< \cdots >'$ denotes flux surface average over $\mathbf{r}'$ and

$$\mathit{\Pi}(\mathbf{r}, \mathbf{v}, \mathbf{r}', \mathbf{v}') = \frac{1}{\langle \delta(\mathbf{r}) \rangle} \delta(\mathbf{r} - \mathbf{r}') \delta(\mathbf{v} - \mathbf{v}') - K(v, v'). \tag{2.108}$$

As defined in Eq. (2.77) the parallel current is defined via the adjoint generalized Spitzer function and a steady state source as follows,

$$\begin{aligned}
\langle j_\parallel B \rangle &= -e \left\langle \int \mathrm{d}^3 v \; g(\mathbf{r}, -\mathbf{v}) \widetilde{Q}(\mathbf{r}, \mathbf{v}) \right\rangle \\
&= -e \left\langle \int \mathrm{d}^3 v \; g(\mathbf{r}, -\mathbf{v}) \left\langle \int \mathrm{d}^3 v' \mathit{\Pi}(\mathbf{r}, \mathbf{v}, \mathbf{r}', \mathbf{v}') Q(\mathbf{r}', \mathbf{v}') \right\rangle' \right\rangle \\
&= -e \left\langle \int \mathrm{d}^3 v' \; Q(\mathbf{r}', \mathbf{v}') \left\langle \int \mathrm{d}^3 v g(\mathbf{r}, -\mathbf{v}) \mathit{\Pi}(\mathbf{r}, \mathbf{v}, \mathbf{r}', \mathbf{v}') \right\rangle \right\rangle' \\
&= -e \left\langle \int \mathrm{d}^3 v \; \widetilde{g}(\mathbf{r}, -\mathbf{v}) Q(\mathbf{r}, \mathbf{v}) \right\rangle,
\end{aligned} \tag{2.109}$$

with

$$\begin{aligned}\widetilde{g}(\mathbf{r},\mathbf{v}) &= \left\langle \int \mathrm{d}^3 v g(\mathbf{r},\mathbf{v}) \mathit{\Pi}(\mathbf{r},\mathbf{v},\mathbf{r}',\mathbf{v}') \right\rangle \\ &= g(\mathbf{r},\mathbf{v}) - \left\langle \int \mathrm{d}^3 v' \, K(v',v) g(\mathbf{r}',\mathbf{v}') \right\rangle' \\ &= g(\mathbf{r},\mathbf{v}) - c_{g0} - c_{g2} \left(\frac{v}{v_T}\right)^2 \end{aligned} \tag{2.110}$$

and the constants

$$c_{g0} = \frac{5}{2n_0} \left\langle \int \mathrm{d}^3 v g(\mathbf{r},\mathbf{v}) f_M(v) \right\rangle - \frac{1}{n_0} \left\langle \int \mathrm{d}^3 v \left(\frac{v}{v_T}\right)^2 g(\mathbf{r},\mathbf{v}) f_M(v) \right\rangle, \tag{2.111}$$

$$c_{g2} = -\frac{1}{n_0 v_T^2} \left\langle \int \mathrm{d}^3 v g(\mathbf{r},\mathbf{v}) f_M(v) \right\rangle + \frac{2}{3 n_0 v_T^2} \left\langle \int \mathrm{d}^3 v \left(\frac{v}{v_T}\right)^2 g(\mathbf{r},\mathbf{v}) f_M(v) \right\rangle. \tag{2.112}$$

Thus, the solution of the Spitzer problem (2.72) is defined up to the nullspace,

$$g_0(v) = \bar{c_0} + \bar{c_2} \left(\frac{v}{v_T}\right)^2, \tag{2.113}$$

which is used to form a corrected solution as follows,

$$\widetilde{g}(\mathbf{r},\mathbf{v}) = g(\mathbf{r},\mathbf{v}) - g_0(v). \tag{2.114}$$

It is seen that $\bar{c_0} = c_{g0}$ and $\bar{c_2} = c_{g2}$ for $g = g_0$ so that $\widetilde{g}(\mathbf{r},\mathbf{v}) = 0$.

In the case of the relativistic collision operator as introduced in Section 2.4 the integrals in Eq. (2.91)–(2.93) have to be solved numerically and the nullspace has the form

$$g_0(u) = \bar{c_0} + 2\bar{c_2} \left(\frac{u}{v_T}\right)^2 (\gamma+1)^{-1}, \tag{2.115}$$

where $u = \gamma v$ is the normalized momentum, $\gamma = \sqrt{1 + u^2/c^2}$ is the relativistic factor, and c is the speed of light.

The described nullspace correction removes a constant and quadratic (in the velocity module) offset of the generalized Spitzer function as computed by NEO-2. If this correction is not taken into account, a wrong current in ECCD simulations, where this function is used as ECCD efficiency in phase space, would be the result. The constant offset would result in a fake current if the source term Q_{RF} delivers particles in the system, what is not the case for ECCD, and the quadratic offset would result in a fake current if the source term Q_{RF} delivers energy, what is always the case for ECCD.

2.3 Matrix elements of the full linearized Coulomb collision operator

2.3.1 Overview

The code NEO-2 solves the drift kinetic equation using the full linearized Coulomb collision operator including energy and momentum conservation. In this code, the dependence of the distribution function on energy is discretized using an expansion over basis functions. Respectively, the energy space in the collision operator is represented by matrix elements independent of the energy variable. This representation using the associated Laguerre polynomials of the order 3/2 as a basis has been presented in Ref. 39 and has been extensively derived in the thesis of G. Leitold [40]. In this chapter a more general derivation of the matrix elements of the collision operator is presented which is not limited to a particular set of basis functions.

2.3.2 Linearization and discretization

As described in Section 2.1.2, in first order the solution of the drift kinetic equation is represented as a perturbation f_{a1} to a Maxwellian f_{a0} as follows,

$$f_a = f_{a0} + f_{a1} = f_{a0} + f_{a0} g_a, \tag{2.116}$$

where $f_{a1} = f_{a0} g_a$. The non-relativistic local Maxwellian is cast into a form depending on the radial position r and the velocity module v,

$$f_{a0}(v) = \frac{n_a}{\pi^{3/2} v_{Ta}^3} e^{-(v/v_{Ta})^2}, \tag{2.117}$$

where n_a is the particle density, $v_{Ta} = \sqrt{2T_a/m_a}$ is the thermal velocity, T_a is the particle temperature, and m_a is the particle mass. In the collision integral describing scattering of test species a by field species b,

$$\mathcal{C}[f_a, f_b] = \mathcal{C}[f_{a0}, f_{b0}] + \mathcal{C}[f_{a1}, f_{b0}] + \mathcal{C}[f_{a0}, f_{b1}] + \mathcal{C}[f_{a1}, f_{b1}], \tag{2.118}$$

two terms of different order of magnitude can be neglected. First, the non-linear term $\mathcal{C}[f_{a1}, f_{b1}]$ is of quadratic order and is therefore neglected. Second, the lowest order term $\mathcal{C}[f_{a0}, f_{b0}]$ is omitted, which is exactly zero if the two species a and b have the same temperature. However, for different temperatures as they might occur in simulations for plasmas with ion impurities, two different cases have to be considered. First, in a simple plasma (electrons + one ion species) the temperature equilibration process between electrons and ions is a very slow process because it scales with a factor $m_e/m_i \ll 1$ as compared to the usual electron-ion collision time. Therefore, this term is of the order of the profile relaxation time which is quadratic in Larmor radius ordering. Second, in a multi-species plasma where different ion sorts with comparable masses have different temperatures, the temperature equilibration time is very short what results in almost the same temperatures of interacting species. The difference between these temperatures is of the order of the ratio of collision time and transport time, and, respectively, the zero order term is of the same order. Therefore it is ignored in computations of neoclassical transport coefficients. Furthermore, the collision term of two Maxwellians with different temperatures is an isotropic source which does not have any contribution to flux surface averaged neoclassical diffusion coefficients as they are computed with NEO-2.

Following the simplifications described above the linearized collision operator

$$\begin{aligned}\hat{L}_c[f_a, f_b] &= \mathcal{C}[f_{a1}, f_{b0}] + \mathcal{C}[f_{a0}, f_{b1}] \\ &= \hat{L}_{ab}^{(D)} f_{a1} + \hat{L}_{ab}^{(I)} f_{b1}\end{aligned} \tag{2.119}$$

is split into a differential operator $\hat{L}_{ab}^{(D)}$ ("test particle part"), and into an integral operator $\hat{L}_{ab}^{(I)}$ ("field particle part"), respectively. In the field aligned coordinates $(r, \vartheta, \varphi_0)$, where $\varphi_0 = \varphi - q\vartheta$ labels the field line (q is a safety factor), the single-drive gyrokinetic equation including in case of weakly perturbed tokamak equilibria also the toroidal rotation term with rotation frequency ω is written as,

$$v\lambda h^{\vartheta} f_{a0} \frac{\partial g_a}{\partial \vartheta} + i\omega f_{a0} g_a - \sum_b \left(\hat{L}_{ab}^{(D)} f_{a1} + \hat{L}_{ab}^{(I)} f_{b1} \right) = q_a f_{a0}, \tag{2.120}$$

where the sum is over the different species (see also Ref. 2).

The energy dependence of the solution $g_a(\vartheta, v, \eta, \sigma)$, where a labels here all ion species and electrons, is modeled using the Galerkin method as follows,

$$g_a(\vartheta, x, \eta, \sigma) = \sum_{m'=0}^{M} g_{a,m'}(\vartheta, \eta, \sigma)\varphi_{m'}(x), \tag{2.121}$$

where the solution is expanded via $M+1$ arbitrary, differentiable basis functions $\varphi_m(v)$, and the normalized velocity module

$$x = \frac{v}{v_{Ta}} \tag{2.122}$$

has been introduced. Here, $\eta = v_\perp^2/(v^2 B) = (1-\lambda^2)/B$ is the normalized perpendicular adiabatic invariant, B is the magnetic field module, ϑ is the poloidal angle along the field line, and σ is the parallel velocity sign. Multiplication of Eq. (2.120) with $(n_a v_{Ta}^{2+\alpha})^{-1}\varphi_m(v/v_{Ta})v^{3+\alpha}e^{-\beta(v/v_{Ta})^2}$, where α and β are constants defined below, followed by subsequent integration over the velocity module reduces the kinetic equation to a coupled set of 2D equations for $g_{a,m}$,

$$\sum_{m'=0}^{M} \left[\rho_{mm'} \lambda h^\vartheta \frac{\partial}{\partial \vartheta} g_{a,m'} + i\omega_{mm'} g_{a,m'} - \sum_b \left(\hat{L}_{mm'}^{(D),ab} g_{a,m'} + \hat{L}_{mm'}^{(I),ab} g_{b,m'} \right) \right] = q_{a,m}, \tag{2.123}$$

where abbreviations for the matrix elements $\rho_{mm'}$, $\omega_{mm'}$, $\hat{L}_{mm'}^{(D),ab}$, $\hat{L}_{mm'}^{(I),ab}$, and $q_{a,m}$ have been introduced. These matrix elements are given in compact notation as follows,

$$\rho_{mm'} = \left\langle \varphi_m\left(\frac{v}{v_{Ta}}\right) \middle| v f_{a0}(v) \varphi_{m'}\left(\frac{v}{v_{Ta}}\right) \right\rangle, \tag{2.124}$$

$$\omega_{mm'} = \left\langle \varphi_m\left(\frac{v}{v_{Ta}}\right) \middle| f_{a0}(v) \omega \varphi_{m'}\left(\frac{v}{v_{Ta}}\right) \right\rangle, \tag{2.125}$$

$$\hat{L}_{mm'}^{(D),ab} = \left\langle \varphi_m\left(\frac{v}{v_{Ta}}\right) \middle| \hat{L}_{ab}^{(D)} f_{a0}(v) \varphi_{m'}\left(\frac{v}{v_{Ta}}\right) \right\rangle, \tag{2.126}$$

$$\hat{L}_{mm'}^{(I),ab} = \left\langle \varphi_m\left(\frac{v}{v_{Ta}}\right) \middle| \hat{L}_{ab}^{(I)} f_{b0}(v) \varphi_{m'}\left(\frac{v}{v_{Tb}}\right) \right\rangle, \tag{2.127}$$

$$q_{a,m} = \left\langle \varphi_m\left(\frac{v}{v_{Ta}}\right) \middle| q_a \right\rangle, \tag{2.128}$$

where the scalar product is defined by

$$\langle f \,|\, g\rangle = \frac{1}{n_a v_{Ta}^{2+\alpha}} \int\limits_0^\infty \mathrm{d}v v^{3+\alpha} e^{-\beta(v/v_{Ta})^2} f(v) g(v) \tag{2.129}$$

with the constants α and β which allow weighting in velocity space ($\alpha = \beta = 0$ is the default case). For orthogonal basis functions Eq. (2.124), which corresponds to the factor before the derivative along the field line, is expressed as a constant times a Kronecker symbol,

$$\rho_{mm'} = \left\langle \varphi_m \left(\frac{v}{v_{Ta}}\right) \middle| v f_{a0}(v) \varphi_{m'} \left(\frac{v}{v_{Ta}}\right) \right\rangle = C_m \delta_{mm'} \tag{2.130}$$

with $C_m = 1$ for an orthonormal basis. This feature should be preserved also for non-orthogonal basis functions, therefore, the whole Eq. (2.123) is multiplied with the inverse matrix of (2.130), ρ^{-1}, resulting in

$$\begin{aligned} &\lambda h^\vartheta \frac{\partial g_{a,m}}{\partial \vartheta} + \sum_{m''=0}^{M} \sum_{m'=0}^{M} \rho^{-1}_{mm''} \left[i\omega_{m''m'} g_{a,m'} - \sum_b \left(\hat{L}^{(D),ab}_{m''m'} g_{a,m'} + \hat{L}^{(I),ab}_{m''m'} g_{b,m'} \right) \right] \\ &= \sum_{m'=0}^{M} \rho^{-1}_{mm'} q_{a,m'}, \end{aligned} \tag{2.131}$$

where

$$\sum_{m''=0}^{M} \rho^{-1}_{mm''} \rho_{m''m'} = \delta_{mm'}. \tag{2.132}$$

The definitions of the sources (2.59) and the drift velocity (2.42) are used to write explicitly the matrix elements for the source terms (2.128) in compact form,

$$\begin{aligned} q_{a,k,m} &= \frac{1}{n_a v_{Ta}^{2+\alpha}} \int\limits_0^\infty \mathrm{d}v v^{4+\alpha} f_{a0}(v) \left(\frac{v}{v_{Ta}}\right)^{2k-1-5\delta_{3k}} \varphi_m \left(\frac{v}{v_{Ta}}\right) \\ &= \pi^{-3/2} \int\limits_0^\infty \mathrm{d}x x^{4+\alpha} e^{-(1+\beta)x} x^{2k-1-5\delta_{3k}} \varphi_m(x), \end{aligned} \tag{2.133}$$

where k labels the drive.

2.3.3 Differential part of the collision operator

The differential part describing the collisions of test particles with a Maxwellian background is cast in terms of three characteristic collision frequencies as follows [26],

$$\begin{aligned}\hat{L}_{ab}^{(D)} f_{a1} &= 2\nu_D^{ab} f_{a0}(v)\lambda \frac{\partial}{\partial\eta}\frac{\lambda\eta}{B}\frac{\partial}{\partial\eta} g_a(\vartheta, v, \eta, \sigma) \\ &+ \frac{1}{v^2}\frac{\partial}{\partial v}\left[v^3 \frac{m_a}{m_a + m_b}\nu_s^{ab} + v^4 \frac{1}{2}\nu_\parallel^{ab}\frac{\partial}{\partial v}\right] f_{a0}(v) g_a(\vartheta, v, \eta, \sigma), \end{aligned} \tag{2.134}$$

where $f_{a1} = f_{a0} g_a$ as follows from Eq. (2.116). The deflection frequency

$$\begin{aligned}\nu_D^{ab} &= \hat{\nu}_{ab}\frac{\mathrm{erf}(y) - G(y)}{x^3} \\ &= \frac{3\sqrt{\pi}}{4\tau_{ab}}\frac{\mathrm{erf}(y) - G(y)}{x^3}\end{aligned} \tag{2.135}$$

defines the rate at which the direction of the velocity vector changes, where

$$G(y) = \frac{\mathrm{erf}(y) - y\frac{\partial}{\partial y}\mathrm{erf}(y)}{2y^2} \tag{2.136}$$

is the Chandrasekhar function defined via the error function $\mathrm{erf}(y)$. Here the normalized velocity module

$$y = \frac{v}{v_{Tb}} = \gamma_{ab} x \tag{2.137}$$

has been introduced with

$$\gamma_{ab} = \frac{v_{Ta}}{v_{Tb}} \tag{2.138}$$

being the ratio of the thermal velocities of different species (which is unity for equal species).

The collision time for inter-species collisions is given by

$$\tau_{ab} = \frac{3 m_a^2 v_{Ta}^3}{16\sqrt{\pi} n_b e_a^2 e_b^2 \ln\Lambda_{aa}} \tag{2.139}$$

with the Coulomb logarithm $\ln\Lambda_{aa}$ as defined in Ref. 38.

The slowing down frequency

$$\nu_s^{ab} = \frac{3\sqrt{\pi}}{4\tau_{ab}} \frac{2T_a}{T_b} \left(1 + \frac{m_b}{m_a}\right) \frac{G(y)}{x} \tag{2.140}$$

represents the deceleration rate of particles of species a by particles of species b. The parallel velocity diffusion frequency is defined by

$$\nu_\parallel^{ab} = 2\hat{\nu}_{ab} \frac{G(y)}{x^3} = \frac{3\sqrt{\pi}}{2\tau_{ab}} \frac{G(y)}{x^3}. \tag{2.141}$$

The differential part of the collision operator in Eq. (2.123) can be recast to

$$\begin{aligned}
\sum_{m'=0}^{M} \hat{L}_{mm'}^{(D),ab} g_{a,m'}(\vartheta,\eta,\sigma) &= \sum_{m'=0}^{M} \left\langle \varphi_m\left(\frac{v}{v_{Ta}}\right) \middle| \hat{L}_{mm'}^{(D),ab} f_{a0}(v) \varphi_{m'}\left(\frac{v}{v_{Ta}}\right) \right\rangle g_{a,m'}(\vartheta,\eta,\sigma) \\
&= \sum_{m'=0}^{M} \left[\left\langle \varphi_m\left(\frac{v}{v_{Ta}}\right) \middle| 2\nu_D^{ab} f_{a0}(v) \varphi_{m'}\left(\frac{v}{v_{Ta}}\right) \right\rangle \lambda \frac{\partial}{\partial\eta} \frac{\lambda\eta}{B} \frac{\partial}{\partial\eta} + \right. \\
&\quad + \left\langle \varphi_m\left(\frac{v}{v_{Ta}}\right) \middle| \frac{1}{v^2}\frac{\partial}{\partial v}\left[v^3 \frac{m_a}{m_a+m_b} \nu_s^{ab} + \right.\right. \\
&\quad \left.\left. + v^4 \frac{1}{2}\nu_\parallel^{ab} \frac{\partial}{\partial v} \right] f_{a0}(v) \varphi_{m'}\left(\frac{v}{v_{Ta}}\right) \right\rangle \Bigg] g_{a,m'}(\vartheta,\eta,\sigma) \\
&= \kappa \sum_{m'=0}^{M} \left[2\nu_{mm'}^{ab} \lambda \frac{\partial}{\partial\eta} \frac{\lambda\eta}{B} \frac{\partial}{\partial\eta} + D_{mm'}^{ab} \right] g_{a,m'}(\vartheta,\eta,\sigma),
\end{aligned} \tag{2.142}$$

where $\nu_{mm'}^{ab}$ and $D_{mm'}^{ab}$ are constants corresponding to pitch-angle scattering and energy scattering by field particles, respectively. Those constants are independent of plasma parameters, like density and temperature, which enter the equation only via ratios and the inverse mean free path length

$$\kappa = \frac{1}{l_c} = \frac{1}{v_{Ta}\tau_{aa}}, \tag{2.143}$$

with the mean free path

$$l_c = \frac{3T_a^2}{4\sqrt{\pi} n_a e_a^4 \ln\Lambda_{aa}}, \tag{2.144}$$

and the collision time for self-collisions [26]

$$\tau_{aa} = \frac{3m_a^2 v_{Ta}^3}{16\sqrt{\pi} n_a e_a^4 \ln\Lambda_{aa}}. \tag{2.145}$$

From Eq. (2.142) it is found that

$$\nu^{ab}_{mm'} = \frac{1}{\kappa}\left\langle \varphi_m\left(\frac{v}{v_{Ta}}\right) \middle| f_{a0}(v)\nu_D^{ab}\varphi_{m'}\left(\frac{v}{v_{Ta}}\right)\right\rangle, \tag{2.146}$$

where evaluation of the scalar product (2.129) and transformation of the integration variable v to the dimensionless normalized velocity module x results in

$$\begin{aligned}\nu^{ab}_{mm'} &= \frac{v_{Ta}\tau_{aa}}{n_a v_{Ta}^{2+\alpha}} \int\limits_0^\infty \mathrm{d}v v^{3+\alpha} e^{-\beta(v/v_{Ta})^2} f_{a0}(v)\varphi_m\left(\frac{v}{v_{Ta}}\right)\nu_D^{ab}\varphi_{m'}\left(\frac{v}{v_{Ta}}\right) \\ &= \frac{3}{4\pi}\frac{\tau_{aa}}{\tau_{ab}} \int\limits_0^\infty \mathrm{d}x x^\alpha e^{-(1+\beta)x^2}\varphi_m(x)\left[\mathrm{erf}(x\gamma_{ab}) - G(x\gamma_{ab})\right]\varphi_{m'}(x). \end{aligned} \tag{2.147}$$

The constant $D^{ab}_{mm'}$ of Eq. (2.142) is defined by

$$D^{ab}_{mm'} = \frac{1}{\kappa}\left\langle \varphi_m\left(\frac{v}{v_{Ta}}\right) \middle| \frac{1}{v^2}\frac{\partial}{\partial v}\left[v^3\frac{m_a}{m_a+m_b}\nu_s^{ab} + v^4\frac{1}{2}\nu_\parallel^{ab}\frac{\partial}{\partial v}\right] f_{a0}(v)\varphi_{m'}\left(\frac{v}{v_{Ta}}\right)\right\rangle. \tag{2.148}$$

Following the same procedure as for $\nu^{ab}_{mm'}$, the scalar product of Eq. (2.148) evaluates to

$$\begin{aligned}D^{ab}_{mm'} &= \frac{v_{Ta}\tau_{aa}}{n_a v_{Ta}^{2+\alpha}} \int\limits_0^\infty \mathrm{d}v v^{3+\alpha} e^{-\beta(v/v_{Ta})^2}\varphi_m\left(\frac{v}{v_{Ta}}\right)\frac{1}{v^2}\frac{\partial}{\partial v}\left[v^3\frac{m_a}{m_a+m_b}\nu_s^{ab} + \right. \\ &\quad \left. + v^4\frac{1}{2}\nu_\parallel^{ab}\frac{\partial}{\partial v} f_{a0}(v)\right]\varphi_{m'}\left(\frac{v}{v_{Ta}}\right) \\ &= \frac{3}{4\pi}\frac{\tau_{aa}}{\tau_{ab}} \int\limits_0^\infty \left[\mathrm{d}x x^{1+\alpha}e^{-\beta x^2}\varphi_m(x)\frac{2T_a}{T_b}\frac{\partial}{\partial x}\left[x^2 G(x\gamma_{ab})e^{-x^2}\varphi_{m'}(x)\right] + \right. \\ &\quad \left. + x^{1+\alpha}e^{-\beta x^2}\varphi_m(x)\frac{\partial}{\partial x}\left[xG(x\gamma_{ab})\frac{\partial}{\partial x}(e^{-x^2}\varphi_{m'}(x))\right]\right], \end{aligned} \tag{2.149}$$

where integration by parts gives

$$
\begin{aligned}
D^{ab}_{mm'} = & -\frac{3}{4\pi}\frac{\tau_{aa}}{\tau_{ab}}\int\limits_0^\infty \mathrm{d}x \frac{\partial}{\partial x}\left(x^{1+\alpha}e^{-\beta x^2}\varphi_m(x)\right) \times \\
& \times xG(x\gamma_{ab})\left[\frac{2T_a}{T_b}xe^{-x^2}\varphi_{m'}(x) + \frac{\partial}{\partial x}(e^{-x^2}\varphi_{m'}(x))\right], \qquad (2.150)
\end{aligned}
$$

assuming that

$$
\varphi_m(x)x^{3+\alpha}e^{-(1+\beta)x^2}G(x\gamma_{ab})\frac{\partial\varphi_{m'}(x)}{\partial x}\bigg|_0^\infty = 0. \qquad (2.151)
$$

2.3.4 Integral part of the collision operator

The integral part ("field particle part") of the collision operator, which is responsible in particular for momentum and energy conservation, is given by [26],

$$
\begin{aligned}
\hat{L}^{(I)}_{ab} f_{b1} &= L^{ab} f_{a0}\left[\frac{m_a}{m_b}f_{b1} + \frac{2}{v^2_{Ta}}\varphi_{b1} + \left(1-\frac{m_a}{m_b}\right)\frac{2v}{v^2_{Ta}}\frac{\partial\varphi_{b1}}{\partial v} - \frac{4v^2}{v^4_{Ta}}\frac{\partial^2\psi_{b1}}{\partial v^2}\right] \\
&= L^{ab} f_{a0}\left[\frac{m_a}{m_b}f_{b1} + \frac{2}{v^2_{Ta}}\varphi_{b1} + \left(1-\frac{m_a}{m_b}\right)\frac{2y}{v^2_{Ta}}\frac{\partial\varphi_{b1}}{\partial y} - \frac{4y^2}{v^4_{Ta}}\frac{\partial^2\psi_{b1}}{\partial y^2}\right] \qquad (2.152)
\end{aligned}
$$

with

$$
L^{ab} f_{a0} = \left(\frac{4\pi e_a e_b}{m_a}\right)^2 \ln\Lambda_{ab} f_{a0} = \frac{3n_a e^{-x^2}}{\tau_{ab} n_b}. \qquad (2.153)
$$

Here, the Trubnikov potentials φ_{b1} and ψ_{b1} of the non-Maxwellian distribution f_{b1} are involved, which are defined in Ref. 28 as follows,

$$
\begin{aligned}
\varphi_{b1}(\vartheta, \mathbf{v}) &= -\frac{1}{4\pi}\int \mathrm{d}^3v' \frac{f_{b1}(\vartheta, \mathbf{v}')}{|\mathbf{v}-\mathbf{v}'|}, \qquad (2.154) \\
\psi_{b1}(\vartheta, \mathbf{v}) &= -\frac{1}{8\pi}\int \mathrm{d}^3v' |\mathbf{v}-\mathbf{v}'| f_{b1}(\vartheta, \mathbf{v}'). \qquad (2.155)
\end{aligned}
$$

The pitch angle dependence of the perturbed field particle distribution function is given as an expansion over $L+1$ Legendre polynomials $P_l(\lambda)$ of the degree l,

$$
f_{b1}(\vartheta, \lambda, y) = f_{b0}(y)\sum_{m'=0}^{M} g_{b,m'}(\vartheta, \eta(\lambda), \sigma(\lambda))\varphi_{m'}(y)
$$

$$= f_{b0}(y) \sum_{m'=0}^{M} \sum_{l=0}^{L} g_{b,m',l}(\vartheta) P_l(\lambda) \varphi_{m'}(y), \tag{2.156}$$

with

$$g_{b,m'}(\vartheta, \eta(\lambda), \sigma(\lambda)) = \sum_{l=0}^{L} g_{b,m',l}(\vartheta) P_l(\lambda). \tag{2.157}$$

As derived in Appendix A the Trubnikov potentials for the perturbation f_{b1} are given as follows,

$$\begin{aligned} \varphi_{b1}(\vartheta, \mathbf{v}) = & -\frac{1}{2} \sum_{m'=0}^{M} \sum_{l=0}^{L} g_{b,m',l}(\vartheta) \frac{2}{2l+1} P_l(\lambda) \times \\ & \times \left[v^{-l-1} \int\limits_0^v \mathrm{d}v' v'^2 f_{b0}(v') v'^l \varphi_{m'}\left(\frac{v'}{v_{Tb}}\right) + \right. \\ & \left. + v^l \int\limits_v^\infty \mathrm{d}v' v'^2 f_{b0}(v') \frac{1}{v'^{l+1}} \varphi_{m'}\left(\frac{v'}{v_{Tb}}\right) \right], \end{aligned} \tag{2.158}$$

and

$$\begin{aligned} \psi_{b1}(\vartheta, \mathbf{v}) = & -\frac{1}{4} \sum_{m'=0}^{M} \sum_{l=0}^{L} g_{b,m',l}(\vartheta) \frac{2}{2l+1} P_l(\lambda) \times \\ & \times \left[\frac{1}{2l+3} v^{-l-1} \int\limits_0^v \mathrm{d}v' v'^{l+4} f_{b0}(v') \varphi_{m'}\left(\frac{v'}{v_{Tb}}\right) - \right. \\ & - \frac{1}{2l-1} v^{-l+1} \int\limits_0^v \mathrm{d}v' v'^{l+2} f_{b0}(v') \varphi_{m'}\left(\frac{v'}{v_{Tb}}\right) + \\ & + \frac{1}{2l+3} v^{l+2} \int\limits_v^\infty \mathrm{d}v' \frac{1}{v'^{l-1}} f_{b0}(v') \varphi_{m'}\left(\frac{v'}{v_{Tb}}\right) - \\ & \left. - \frac{1}{2l-1} v^l \int\limits_v^\infty \mathrm{d}v' \frac{1}{v'^{l-3}} f_{b0}(v') \varphi_{m'}\left(\frac{v'}{v_{Tb}}\right) \right]. \end{aligned} \tag{2.159}$$

In NEO-2 the integral part is taken into account by means of direct or pre-conditioned iterations using an expansion of the solution over Legendre polynomials within each iteration [2],

$$\begin{aligned}\sum_{m'=0}^{M}\hat{L}^{(I),ab}_{mm'}g_{b,m'}(\vartheta,\eta,\sigma) &= \left\langle \varphi_m\left(\frac{v}{v_{Ta}}\right)\middle|\hat{L}^{(I)}_{ab}f_{b1}(v)\right\rangle \\ &= \kappa\sum_{m'=0}^{M}\sum_{l=0}^{L}I^{(l),ab}_{mm'}P_l(\lambda)\int\limits_{-1}^{1}\mathrm{d}\lambda' P_l(\lambda')g_{b,m'}(\vartheta,\eta(\lambda'),\sigma(\lambda')) \\ &= \kappa\sum_{m'=0}^{M}\sum_{l=0}^{L}\frac{2}{2l+1}I^{(l),ab}_{mm'}P_l(\lambda)g_{b,m',l}(\vartheta),\end{aligned} \tag{2.160}$$

where Eq. (2.156) as well as the orthogonality of Legendre polynomials

$$\int_{-1}^{+1}\mathrm{d}\lambda P_{l'}(\lambda)P_l(\lambda) = \frac{2}{2l+1}\delta_{l',l} \tag{2.161}$$

have been used. For reasons of readability in the following the four terms of Eq. (2.152) are treated separately from each other, so that

$$\sum_{m'=0}^{M}\hat{L}^{(I),ab}_{mm'}g_{b,m'} = \sum_{m'=0}^{M}\left(\hat{L}^{(I,1),ab}_{mm'}+\hat{L}^{(I,2),ab}_{mm'}+\hat{L}^{(I,3),ab}_{mm'}+\hat{L}^{(I,4),ab}_{mm'}\right)g_{b,m'}. \tag{2.162}$$

Substituting the first term of the right hand side of Eq. (2.152) in the first line of Eq. (2.160) leads to

$$\begin{aligned}\sum_{m'=0}^{M}\hat{L}^{(I,1),ab}_{mm'}g_{b,m'} &= \left\langle \varphi_m\left(\frac{v}{v_{Ta}}\right)\middle|L^{ab}f_{a0}(v)\frac{m_a}{m_b}f_{b1}(v)\right\rangle \\ &= \sum_{m'=0}^{M}\sum_{l=0}^{L}\left\langle \varphi_m\left(\frac{v}{v_{Ta}}\right)\middle|L^{ab}f_{a0}(v)\frac{m_a}{m_b}f_{b0}(v)\varphi_{m'}\left(\frac{v}{v_{Tb}}\right)\right\rangle P_l(\lambda)g_{b,m',l} \\ &= \kappa\sum_{m'=0}^{M}\sum_{l=0}^{L}\frac{2}{2l+1}I^{(l,1),ab}_{mm'}P_l(\lambda)g_{b,m',l}\end{aligned} \tag{2.163}$$

with

$$I^{(l,1),ab}_{mm'} = \frac{1}{\kappa}\frac{2l+1}{2}\left\langle \varphi_m\left(\frac{v}{v_{Ta}}\right)\middle|L^{ab}f_{a0}(v)\frac{m_a}{m_b}f_{b0}(v)\varphi_{m'}\left(\frac{v}{v_{Tb}}\right)\right\rangle. \tag{2.164}$$

Similar as done for the differential part, the scalar product (2.129) is now evaluated,

$$\begin{aligned}
I^{(l,1),ab}_{mm'} &= \frac{2l+1}{2}\frac{1}{v_{Ta}^{1+\alpha}}\frac{\tau_{aa}}{\tau_{ab}}\frac{m_a}{m_b}\frac{3}{\pi^{3/2}v_{Tb}^3}\int\limits_0^\infty \mathrm{d}v v^{3+\alpha} e^{-(1+\beta)(v/v_{Ta})^2-(v/v_{Tb})^2}\varphi_m\left(\frac{v}{v_{Ta}}\right)\varphi_{m'}\left(\frac{v}{v_{Tb}}\right) \\
&= \frac{2l+1}{2}\frac{3}{\pi^{3/2}}\frac{\tau_{aa}}{\tau_{ab}}\frac{m_a}{m_b}\gamma_{ab}^3\int_0^\infty \mathrm{d}x x^{3+\alpha}e^{-(\beta+\gamma_{ab}^2+1)x^2}\varphi_m(x)\varphi_{m'}(\gamma_{ab}x),
\end{aligned} \tag{2.165}$$

where the ratio of the thermal velocities for species a and species b as defined in Eq. (2.138) has been used. In the same way, the second term of (2.162) is treated as follows,

$$\begin{aligned}
\sum_{m'=0}^{M}\hat{L}^{(I,2),ab}_{mm'}g_{b,m'} &= \left\langle \varphi_m\left(\frac{v}{v_{Ta}}\right)\middle| L^{ab}f_{a0}(v)\frac{2}{v_{Ta}^2}\varphi_{b1}\right\rangle \\
&= -\frac{1}{v_{Ta}^2}\sum_{m'=0}^{M}\sum_{l=0}^{L}\frac{2}{2l+1}\left\langle \varphi_m\left(\frac{v}{v_{Ta}}\right)\middle| L^{ab}f_{a0}(v)\times\right. \\
&\quad\times\left[v^{-l-1}\int\limits_0^v \mathrm{d}v'v'^2f_{b0}(v')v'^l\varphi_{m'}\left(\frac{v'}{v_{Tb}}\right)+\right. \\
&\quad\left.\left.+\,v^l\int\limits_v^\infty \mathrm{d}v'v'^2f_{b0}(v')\frac{1}{v'^{l+1}}\varphi_{m'}\left(\frac{v'}{v_{Tb}}\right)\right]\right\rangle P_l(\lambda)g_{b,m',l} \\
&= \kappa\sum_{m'=0}^{M}\sum_{l=0}^{L}\frac{2}{2l+1}I^{(l,2),ab}_{mm'}P_l(\lambda)g_{b,m',l},
\end{aligned} \tag{2.166}$$

where the coefficient $I^{(l,2),ab}_{mm'}$ is defined by

$$\begin{aligned}
I^{(l,2),ab}_{mm'} &= -\frac{1}{\kappa}\frac{1}{v_{Ta}^2}\left\langle \varphi_m\left(\frac{v}{v_{Ta}}\right)\middle| L^{ab}f_{a0}(v)\times\right. \\
&\quad\times\left[v^{-l-1}\int\limits_0^v \mathrm{d}v'v'^2f_{b0}(v')v'^l\varphi_{m'}\left(\frac{v'}{v_{Tb}}\right)+\right. \\
&\quad\left.\left.+\,v^l\int\limits_v^\infty \mathrm{d}v'v'^2f_{b0}(v')\frac{1}{v'^{l+1}}\varphi_{m'}\left(\frac{v'}{v_{Tb}}\right)\right]\right\rangle.
\end{aligned} \tag{2.167}$$

Evaluation of the scalar product results in

$$\begin{aligned}
I_{mm'}^{(l,2),ab} = &-\frac{3}{\pi^{3/2}}\frac{\tau_{aa}}{\tau_{ab}}\gamma_{ab}^{3}\int_{0}^{\infty}\mathrm{d}x x^{3+\alpha}e^{-(\beta+1)x^{2}}\varphi_{m}(x)\times \\
&\times\left[x^{-l-1}\int_{0}^{x}\mathrm{d}x' e^{-(\gamma_{ab}x')^{2}}x'^{l+2}\varphi_{m'}(\gamma_{ab}x')+\right. \\
&+\left. x^{l}\int_{x}^{\infty}\mathrm{d}x' e^{-(\gamma_{ab}x')^{2}}x'^{-l+1}\varphi_{m'}(\gamma_{ab}x')\right]. \qquad (2.168)
\end{aligned}$$

The third term of Eq. (2.162) involves the first derivative of the Trubnikov potential φ_{b1} with respect to the velocity module and is treated as follows,

$$\begin{aligned}
\sum_{m'=0}^{M}\hat{L}_{mm'}^{(I,3),ab}g_{b,m'} &= \left\langle\varphi_{m}\left(\frac{v}{v_{Ta}}\right)\middle| L^{ab}f_{a0}(v)\left(1-\frac{m_a}{m_b}\right)\frac{2v}{v_{Ta}^{2}}\frac{\partial\varphi_{b1}}{\partial v}\right\rangle \\
&= -\frac{1}{2}\sum_{m'=0}^{M}\sum_{l=0}^{L}\frac{2}{2l+1}\left\langle\varphi_{m}\left(\frac{v}{v_{Ta}}\right)\middle| L^{ab}f_{a0}(v)\left(1-\frac{m_a}{m_b}\right)\frac{2v}{v_{Ta}^{2}}\times\right. \\
&\quad\times\frac{\partial}{\partial v}\left[v^{-l-1}\int_{0}^{v}\mathrm{d}v' v'^{2}f_{b0}(v')v'^{l}\varphi_{m'}\left(\frac{v'}{v_{Tb}}\right)+\right. \\
&\quad+\left.\left. v^{l}\int_{v}^{\infty}\mathrm{d}v' v'^{2}f_{b0}(v')\frac{1}{v'^{l+1}}\varphi_{m'}\left(\frac{v'}{v_{Tb}}\right)\right]\right\rangle P_{l}(\lambda)g_{b,m',l} \\
&= \kappa\sum_{m'=0}^{M}\sum_{l=0}^{L}\frac{2}{2l+1}I_{mm'}^{(l,3),ab}P_{l}(\lambda)g_{b,m',l}, \qquad (2.169)
\end{aligned}$$

where

$$\begin{aligned}
I_{mm'}^{(l,3),ab} = &-\frac{1}{\kappa}\left(1-\frac{m_a}{m_b}\right)\left\langle\varphi_{m}\left(\frac{v}{v_{Ta}}\right)\middle| L^{ab}f_{a0}(v)\frac{v}{v_{Ta}^{2}}\times\right. \\
&\times\frac{\partial}{\partial v}\left[v^{-l-1}\int_{0}^{v}\mathrm{d}v' v'^{2}f_{b0}(v')v'^{l}\varphi_{m'}\left(\frac{v'}{v_{Tb}}\right)+\right. \\
&+\left.\left. v^{l}\int_{v}^{\infty}\mathrm{d}v' v'^{2}f_{b0}(v')\frac{1}{v'^{l+1}}\varphi_{m'}\left(\frac{v'}{v_{Tb}}\right)\right]\right\rangle \\
= &-\frac{3}{\pi^{3/2}}\frac{\tau_{aa}}{\tau_{ab}}\left(1-\frac{m_a}{m_b}\right)\gamma_{ab}^{3}\int_{0}^{\infty}\mathrm{d}x\frac{\partial}{\partial x}\left[x^{4+\alpha}e^{-(\beta+1)x^{2}}\varphi_{m}(x)\right]\times
\end{aligned}$$

$$
\times \left(x^{-l-1} \int\limits_0^x \mathrm{d}x' e^{-(\gamma_{ab}x')^2} \varphi_{m'}(\gamma_{ab}x') x'^{l+2} + \right.
$$
$$
\left. + x^l \int\limits_x^\infty \mathrm{d}x' e^{-(\gamma_{ab}x')^2} \varphi_{m'}(\gamma_{ab}x') x'^{-l+1} \right) . \tag{2.170}
$$

In Eq. (2.170) integration by parts has been applied in order to avoid the necessity of the numerical derivative of the integral. Finally, the fourth term of Eq. (2.162) evaluates to

$$
\begin{aligned}
\sum_{m'=0}^{M} \hat{L}_{mm'}^{(I,4),ab} g_{b,m'} = & - \left\langle \varphi_m \left(\frac{v}{v_{Ta}} \right) \middle| L^{ab} f_{a0}(v) \frac{4v^2}{v_{Ta}^4} \frac{\partial \psi_{b1}^2}{\partial v^2} \right\rangle \\
= & \frac{1}{4} \sum_{m'=0}^{M} \sum_{l=0}^{L} \frac{2}{2l+1} \left\langle \varphi_m \left(\frac{v}{v_{Ta}} \right) \middle| L^{ab} f_{a0}(v) \frac{4v^2}{v_{Ta}^4} \times \right. \\
& \times \frac{\partial^2}{\partial v^2} \left[\frac{1}{2l+3} v^{-l-1} \int\limits_0^v \mathrm{d}v' v'^{l+4} f_{b0}(v') \varphi_{m'} \left(\frac{v'}{v_{Tb}} \right) - \right. \\
& - \frac{1}{2l-1} v^{-l+1} \int\limits_0^v \mathrm{d}v' v'^{l+2} f_{b0}(v') \varphi_{m'} \left(\frac{v'}{v_{Tb}} \right) + \\
& + \frac{1}{2l+3} v^{l+2} \int\limits_v^\infty \mathrm{d}v' \frac{1}{v'^{l-1}} f_{b0}(v') \varphi_{m'} \left(\frac{v'}{v_{Tb}} \right) - \\
& \left. \left. - \frac{1}{2l-1} v^{l} \int\limits_v^\infty \mathrm{d}v' \frac{1}{v'^{l-3}} f_{b0}(v') \varphi_{m'} \left(\frac{v'}{v_{Tb}} \right) \right] \right\rangle P_l(\lambda) g_{b,m',l} \\
= & \, \kappa \sum_{m'=0}^{M} \sum_{l=0}^{L} \frac{2}{2l+1} I_{mm'}^{(l,4),ab} P_l(\lambda) g_{b,m',l},
\end{aligned} \tag{2.171}
$$

with

$$
\begin{aligned}
I_{mm'}^{(l,4),ab} = & \frac{1}{\kappa} \left\langle \varphi_m \left(\frac{v}{v_{Ta}} \right) \middle| L^{ab} f_{a0}(v) \frac{v^2}{v_{Ta}^4} \times \right. \\
& \times \frac{\partial^2}{\partial v^2} \left[\frac{1}{2l+3} v^{-l-1} \int\limits_0^v \mathrm{d}v' v'^{l+4} f_{b0}(v') \varphi_{m'} \left(\frac{v'}{v_{Tb}} \right) - \right.
\end{aligned}
$$

$$
\begin{aligned}
&-\frac{1}{2l-1}v^{-l+1}\int\limits_0^v \mathrm{d}v' v'^{l+2} f_{b0}(v')\varphi_{m'}\left(\frac{v'}{v_{Tb}}\right)+\\
&+\frac{1}{2l+3}v^{l+2}\int\limits_v^\infty \mathrm{d}v'\frac{1}{v'^{l-1}} f_{b0}(v')\varphi_{m'}\left(\frac{v'}{v_{Tb}}\right)-\\
&-\frac{1}{2l-1}v^{l}\int\limits_v^\infty \mathrm{d}v'\frac{1}{v'^{l-3}} f_{b0}(v')\varphi_{m'}\left(\frac{v'}{v_{Tb}}\right)\Bigg]\Bigg\rangle\\
=&-\frac{3}{\pi^{3/2}}\frac{\tau_{aa}}{\tau_{ab}}\gamma_{ab}^3\int_0^\infty \mathrm{d}x\frac{\partial}{\partial x}\left[\varphi_m(x)x^{5+\alpha}e^{-(\beta+1)x^2}\right]\times\\
&\times\frac{\partial}{\partial x}\left[\frac{1}{2l+3}x^{-l-1}\int\limits_0^x \mathrm{d}x' x'^{l+4}e^{-(\gamma_{ab}x')^2}\varphi_{m'}(\gamma_{ab}x')-\right.\\
&-\frac{1}{2l-1}x^{-l+1}\int\limits_0^x \mathrm{d}x' x'^{l+2}e^{-(\gamma_{ab}x')^2}\varphi_{m'}(\gamma_{ab}x')+\\
&+\frac{1}{2l+3}x^{l+2}\int\limits_x^\infty \mathrm{d}x' x'^{-l+1}e^{-(\gamma_{ab}x')^2}\varphi_{m'}(\gamma_{ab}x')-\\
&\left.-\frac{1}{2l-1}x^{l}\int\limits_x^\infty \mathrm{d}x' x'^{-l+3}e^{-(\gamma_{ab}x')^2}\varphi_{m'}(\gamma_{ab}x')\right]
\end{aligned}
\tag{2.172}
$$

The evaluation of (2.172) requires a set of basis functions with continues second derivatives, which would not allow the usage of non-smooth local basis functions. Therefore, the integral is split at the discontinues t_i, where $i = 1, ..., N$, of a general basis with discontinues derivatives, where the inner integrals are substituted by the symbol

$$
\begin{aligned}
K(x)=&\left[\frac{1}{2l+3}x^{-l-1}\int\limits_0^x \mathrm{d}x' x'^{l+4}e^{-(\gamma_{ab}x')^2}\varphi_{m'}(\gamma_{ab}x')-\right.\\
&-\frac{1}{2l-1}x^{-l+1}\int\limits_0^x \mathrm{d}x' x'^{l+2}e^{-(\gamma_{ab}x')^2}\varphi_{m'}(\gamma_{ab}x')+\\
&+\frac{1}{2l+3}x^{l+2}\int\limits_x^\infty \mathrm{d}x' x'^{-l+1}e^{-(\gamma_{ab}x')^2}\varphi_{m'}(\gamma_{ab}x')-
\end{aligned}
$$

$$- \frac{1}{2l-1} x^l \int\limits_x^\infty \mathrm{d}x' x'^{-l+3} e^{-(\gamma_{ab} x')^2} \varphi_{m'}(\gamma_{ab} x') \Bigg] \tag{2.173}$$

for reasons of readability. Then, integration by parts and evaluation of the definite integral at the boundaries using the first derivative of φ_m leads to

$$\begin{aligned} I_{mm'}^{(l,4),ab} &= -\frac{3}{\pi^{3/2}} \frac{\tau_{aa}}{\tau_{ab}} \gamma_{ab}^3 \int_0^\infty \mathrm{d}x \frac{\partial}{\partial x} \left[\varphi_m(x) x^{5+\alpha} e^{-(\beta+1)x^2} \right] \frac{\partial}{\partial x} K(x) \\ &= -\frac{3}{\pi^{3/2}} \frac{\tau_{aa}}{\tau_{ab}} \gamma_{ab}^3 \sum_{i=1}^{N-1} \int\limits_{t_i}^{t_{i+1}} \mathrm{d}x \frac{\partial}{\partial x} \left[\varphi_m(x) x^{5+\alpha} e^{-(\beta+1)x^2} \right] \frac{\partial}{\partial x} K(x) \\ &= -\frac{3}{\pi^{3/2}} \frac{\tau_{aa}}{\tau_{ab}} \gamma_{ab}^3 \sum_{i=1}^{N-1} \left(\frac{\partial}{\partial x} \left[x^{5+\alpha} e^{-(\beta+1)x^2} \varphi_m(x) \right] K(x) \Bigg|_{t_i}^{t_{i+1}} - \right. \\ &\quad \left. - \int\limits_{t_i}^{t_{i+1}} \mathrm{d}x \frac{\partial^2}{\partial x^2} \left[x^{5+\alpha} e^{-(\beta+1)x^2} \varphi_m(x) \right] K(x) \right) . \end{aligned} \tag{2.174}$$

Finally, according to Eq. (2.162), the matrix elements for the integral part of Eq. (2.160) are given by

$$I_{mm'}^{(l),ab} = I_{mm'}^{(l,1),ab} + I_{mm'}^{(l,2),ab} + I_{mm'}^{(l,3),ab} + I_{mm'}^{(l,4),ab} . \tag{2.175}$$

While the integrals of the matrix elements can be solved analytically for generalized Laguerre polynomials using efficient recursion relations (see Ref. 40), this is not possible for generalized basis functions. Therefore, in the code NEO-2 the matrix elements are precomputed using numerical integration based on an adaptive open quadrature rule where no sampling points are placed at the integral boundaries. The matrix elements are integrated up to an relative and absolute precision of 10^{-10}. Since the matrix elements are independent of each other, parallelization of the precomputation routines is possible and implemented in the multi-species version of NEO-2.

2.3.5 Sets of basis functions

Generalized Laguerre polynomials

A common set of basis functions for the representation of the velocity module dependence of the distribution function are orthogonal polynomials. Before the extension to arbitrary sets of basis functions as presented in this thesis, NEO-2 used a set of generalized Laguerre polynomials $L_m^{(3/2)}$ of the order 3/2 (Sonine polynomials) as a basis,

$$\varphi_m(x) \equiv C_m L_m^{(3/2)}(x^2) \tag{2.176}$$

with a normalization coefficient making the basis orthonormal,

$$C_m = \pi^{3/4} \sqrt{\frac{2\Gamma(m+1)}{\Gamma(m+5/2)}} \tag{2.177}$$

where $\Gamma(m)$ is the gamma function. While this set of basis functions has turned out to be well-suited for the computation of neoclassical diffusion coefficients in stellarators, the distribution functions represented by these polynomials tend to diverge at higher particle velocities ($> 3.5 v_T$). In Figure 2.1 the basis functions of Eq. (2.176) as functions of the normalized velocity are shown. The impact of the divergence of these basis functions at higher velocities is extensively discussed in Chapter 4.

B-splines

In order to overcome this divergence a more localized set of basis functions is introduced. In contrast to Sonine polynomials, locally defined basis functions are only non-zero for a certain velocity domain,

$$\varphi_m(x) \equiv M_{m,k}(x), \tag{2.178}$$

where

$$M_{i,1}(x) = \begin{cases} 1 & \text{for } t_i \leq x < t_{i+1} \\ 0 & \text{otherwise} \end{cases} \tag{2.179}$$

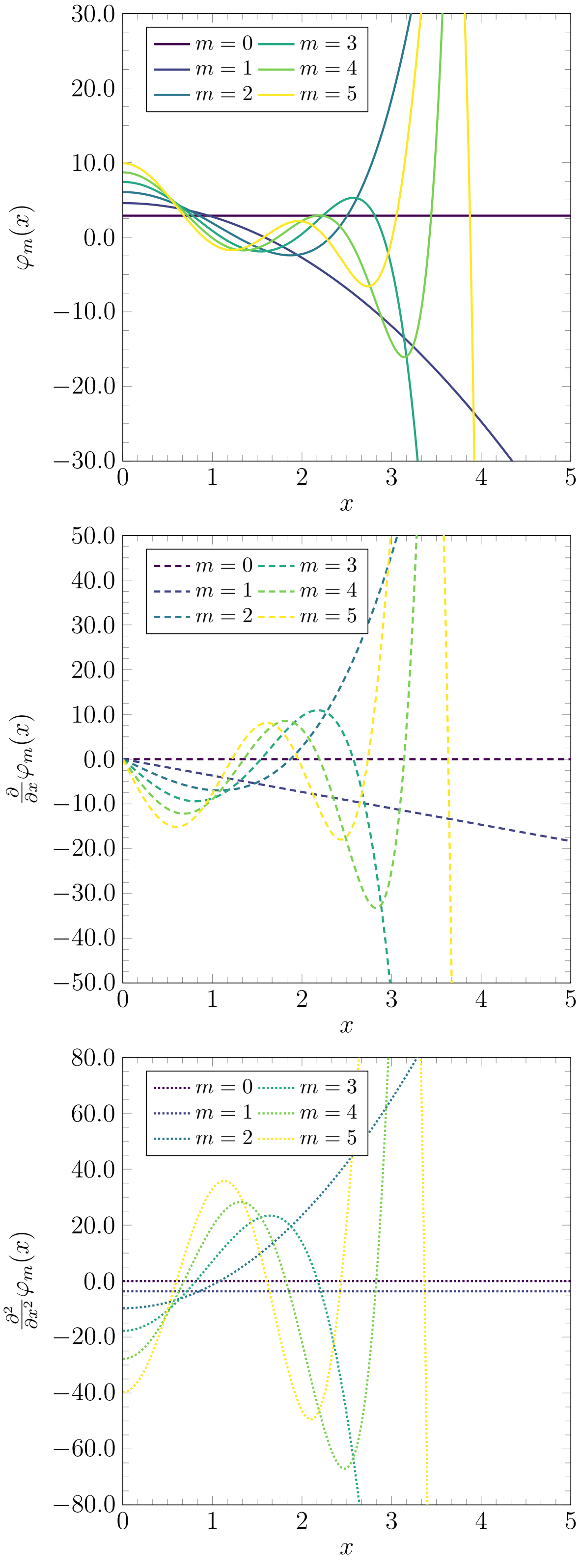

Figure 2.1: Basis functions based on Sonine polynomials (Eq. (2.176)) as functions of the normalized velocity module and their derivatives with respect to x.

are B-splines [41] of the order k. These B-splines are defined via the recursion formula

$$M_{i,k}(x) = \frac{x - t_i}{t_{i+k} - t_i} M_{i,k-1}(x) + \frac{t_{i+k} - x}{t_{i+k} - t_i} M_{i+1,k-1}(x), \tag{2.180}$$

where t_i are N predefined knots with $1 \leq i < N$ (see Ref. 42). The linear combination

$$S_k(x) = \sum_{i=1}^{N+k-2} \alpha_i M_{i,k}(x) \tag{2.181}$$

results in a spline function $S_k(x)$ of order k, where the coefficients α_i are the solutions to the interpolation problem. Eq. (2.181) can be cast to the NEO-2 form as follows,

$$g(\vartheta, \eta, x, \sigma) = \sum_{i=1}^{N+k-2} g_m(\vartheta, \eta, \sigma) M_{i,k}(x) \tag{2.182}$$

with the substitution $\alpha_i \rightarrow g_m(\vartheta, \eta, \sigma)$.
The main difference to generalized Laguerre polynomials can be seen in Figures 2.2, 2.3, and 2.4, where B-splines are shown for orders $k = 2, 3,$ and 4 corresponding to hat functions, quadratic splines, and cubic splines, respectively. The lower the order of the B-splines, the more localized is the basis, i.e., the greater the domain where each basis function is zero. This results in high resolution for resolving the velocity dependence of distribution functions, however, requires the usage of more basis functions in Eq. (2.121) in order to obtain a smooth solution. As shown in Chapter 4, cubic splines are well-suited for the solution of the current drive problem using the same number of basis functions as with Laguerre polynomials.

B-spline extrapolation

Two different approaches which define the behavior of the basis functions based on B-splines outside the interval containing their knots have been implemented in NEO-2. First, the basis functions and respective derivatives are set to zero outside the defined domain. This approach is valid if the last knot is in a region where it does not significantly contribute to the integral kernels of the matrix elements of the collision operator. Such upper velocity limits are in the region of five times the thermal velocity for solution of the current drive problem in a simple plasma (electrons + one ion species with infinite mass). For the solution of multi-species plasmas, as done with the quasilinear version of NEO-2 for tokamaks with 3D perturbations, this upper velocity limit significantly increases for plasmas due to impurities. The reason for this can be found in the momentum conservation part of the collision operator, e.g. in Eq. (2.165). Here, the ratio of the thermal velocities of different species $\gamma_{ab} = v_{Ta}/v_{Tb}$ enters the power of the exponential part of the Maxwell distribution. This pushes the tail of the Maxwellian to much higher velocities, therefore, basis functions also have to be defined up to these velocities. The second approach to treat the B-splines outside their knots is to extend them using a Taylor expansion of the same order k as the B-spline,

$$\varphi_m(x) \equiv \begin{cases} M_{m,k}(x) & \text{for } x \leq t_N \\ \sum_{j=0}^{k-1} \frac{1}{j!} \left.\frac{\partial^j M_{m,k}(x)}{\partial x^j}\right|_{x=t_N} (x - t_N)^j & \text{for } x > t_N, \end{cases} \tag{2.183}$$

where t_N is the last knot. In Figure 2.5 cubic B-splines defined up to $t_N = 4$ with subsequent Taylor expansion are presented. Such choice of basis functions has the advantage that the knots at lower velocities are closer together resulting in higher velocity resolution in this domain, while the expanded domain is well suited for representation of the high velocity limit. Results of the code NEO-2 with different sets of basis functions are presented in Chapter 4.

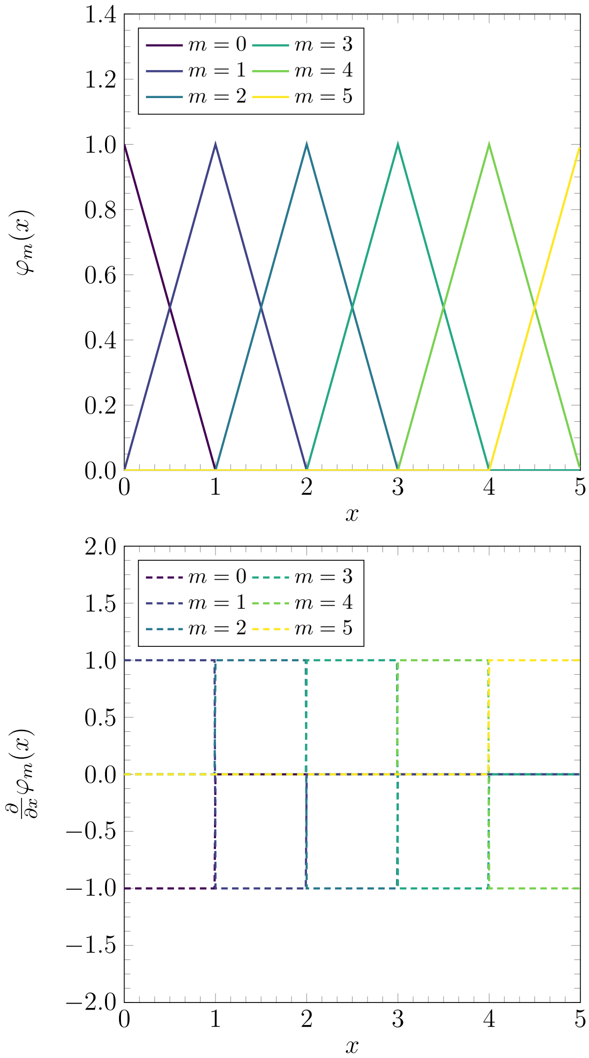

Figure 2.2: B-splines of order $k = 2$ (hat functions) as functions of the normalized velocity module and their derivatives with respect to x. The second derivative is not continues and therefore not shown.

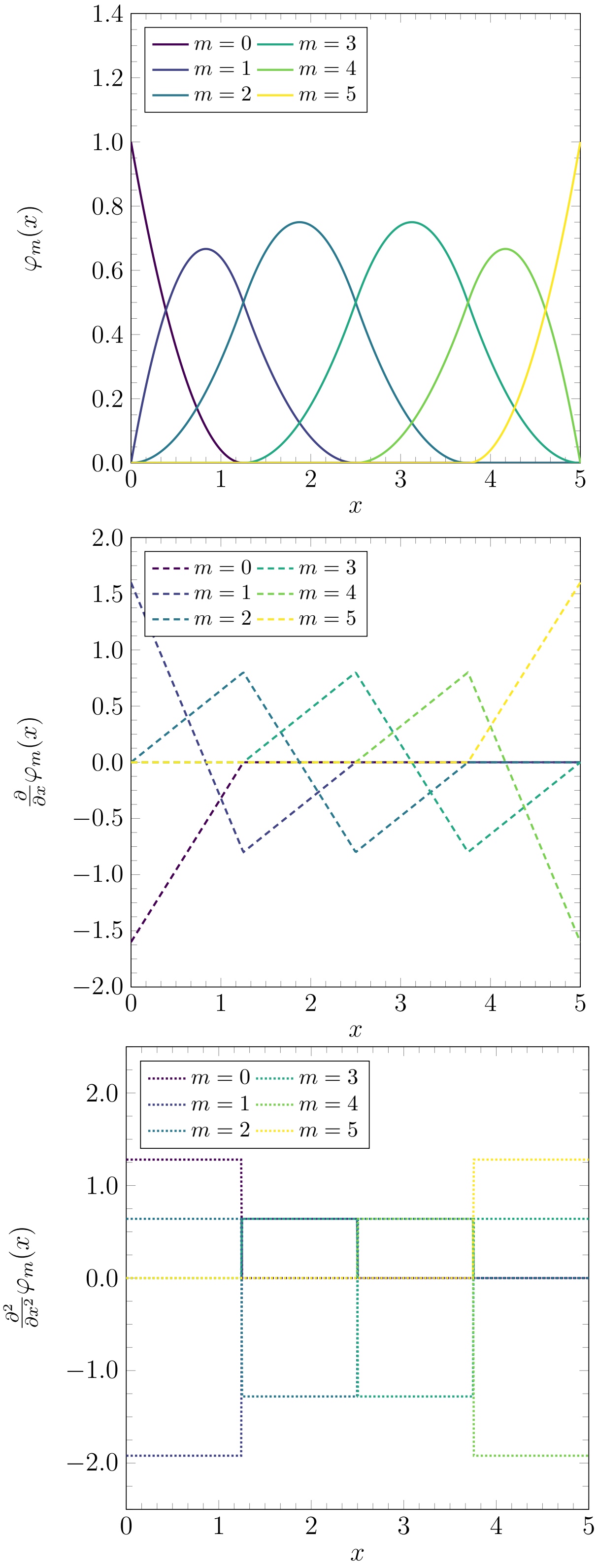

Figure 2.3: B-splines of order $k = 3$ (quadratic B-splines) as functions of the normalized velocity module and their derivatives with respect to x.

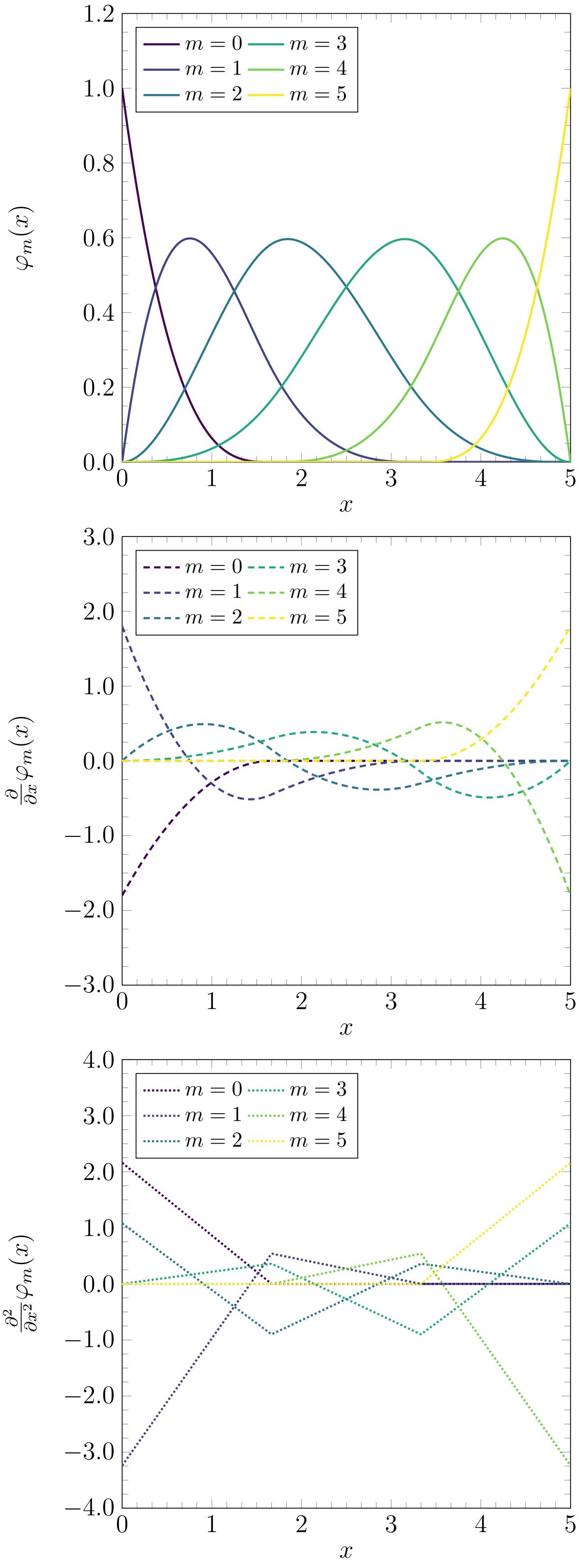

Figure 2.4: B-splines of order $k = 4$ (cubic B-splines) as functions of the normalized velocity module and their derivatives with respect x.

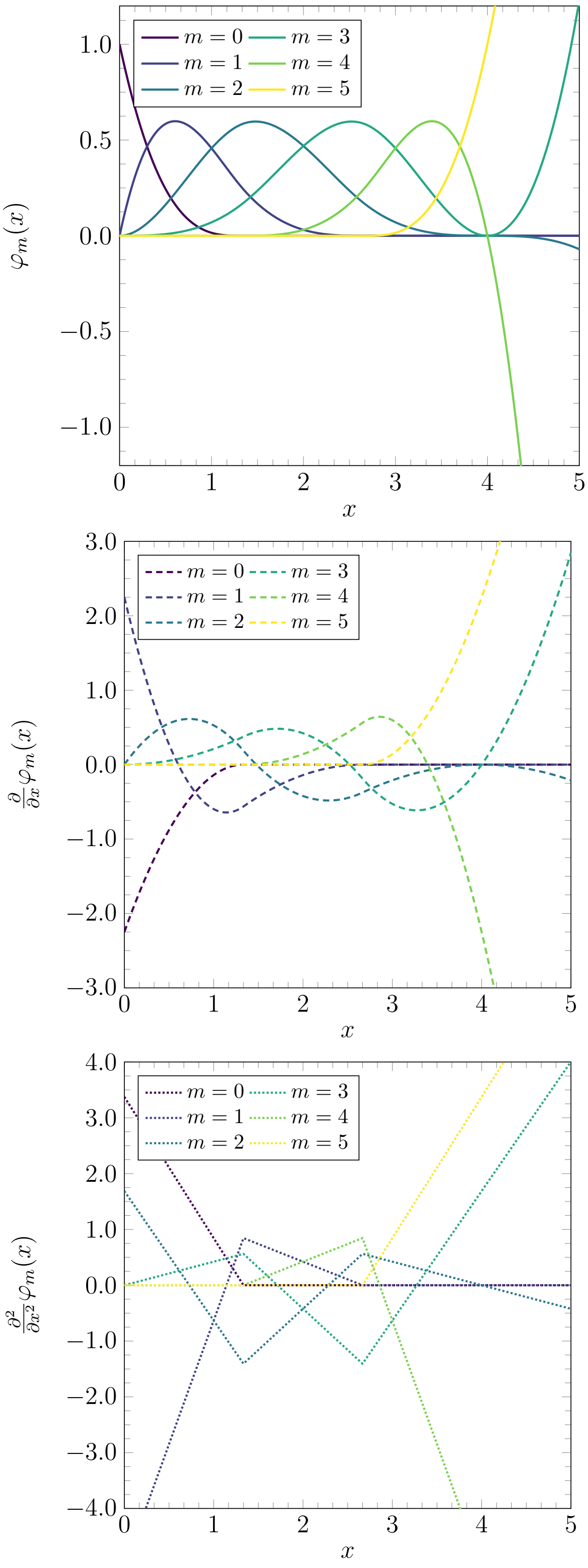

Figure 2.5: B-splines of order $k = 4$ (cubic B-splines) defined up to $x = 4$ as functions of the normalized velocity module with subsequent Taylor expansion and their derivatives with respect to the normalized velocity module.

2.4 Fully relativistic collision model

Up to now the code NEO-2 used the full linearized Coulomb collision operator in the non-relativistic limit including energy and momentum conservation. This limitation to the non-relativistic limit comes from the usage of the Coulomb collision operator given by Trubnikov et al. [28] and Rosenbluth et al. [43] who recast the problem into the form of two scalar potentials. However, Beliaev and Budker [20] derived a general relativistic form as used by Braams and Karney [19] to recast the fully relativistic operator in terms of five scalar potentials. Since the modular design of NEO-2 allows simple exchange of the collision operator, it is possible to upgrade the code to a fully relativistic drift kinetic equation solver without code changes in the well benchmarked core routines. In the following the changes to the matrix elements as derived in Section 2.3 are presented.

2.4.1 Transition of matrix elements to the form of Braams and Karney

In the following, a plasma consisting of electrons and one ion species with infinite mass and an effective ionization stage is considered. The linearized drift kinetic equation retains in the general relativistic case a form similar to Eq. (2.120),

$$v\lambda h^{\vartheta} f_M \frac{\partial g}{\partial \vartheta} + i\omega f_M g - \left(\hat{L}^{(D)} + \hat{L}^{(I)}\right) f_M g = q f_M, \tag{2.184}$$

where v is the velocity module, $\lambda = v_{\parallel}/v$ is a pitch angle parameter, $v_{\parallel}$ is the parallel velocity module, h^{ϑ} is the contra-variant poloidal component of the unit vector along the magnetic field line, f_M is a local Maxwellian, ϑ is the field line parameter, ω is the cross-field rotation frequency, $\hat{L}^{(D)}$ and $\hat{L}^{(I)}$ are the differential and integral part of the Coulomb collision operator, respectively, and q is the source term. The pitch angle dependence of the integral part of the integro-differential equation (2.160) is represented as an expansion over Legendre polynomials. Braams and Karney [19] have reformulated the relativistic collision operator from Beliaev and Budker in terms of five scalar potentials and have given the Legendre expansion up to the first harmonic explicitly. The drift kinetic equation as given in Eq. (2.184) is already in relativistic form, but with ω, $\hat{L}^{(D)}$, $\hat{L}^{(I)}$, and q replaced by their respective relativistic expressions, and with the normalized momentum $u = \gamma v$ used as an independent variable, where $\gamma(u) = \sqrt{1 + u^2/c^2}$ is the relativistic factor, and c is the speed of light. The matrix elements (2.125)–(2.128) are redefined so that they keep the same form if v is simply replaced with u. In order to integrate along a dimensionless variable the substitution to the normalized variable $x = u/v_T$ is applied, where the definition of the thermal velocity remains unchanged. In the following the matrix elements are given for self-collisions only,

$$\omega_{mm'} = \Theta(\mu) \int_0^\infty \mathrm{d}x x^3 \varphi_m(x) \omega(\vartheta, x, \eta) e^{-\mu(\gamma-1)} \varphi_{m'}(x), \tag{2.185}$$

$$\hat{L}^{(D)}_{mm'} = \Theta(\mu) \int_0^\infty \mathrm{d}x x^3 \varphi_m(x) \hat{L}^{(D)} e^{-\mu(\gamma-1)} \varphi_{m'}(x), \tag{2.186}$$

$$\hat{L}^{(I)}_{mm'} = \Theta(\mu) \int_0^\infty \mathrm{d}x x^3 \varphi_m(x) \hat{L}^{(I)} e^{-\mu(\gamma-1)} \varphi_{m'}(x), \tag{2.187}$$

$$q_m = \Theta(\mu) \int_0^\infty \mathrm{d}x x^3 \varphi_m(x) q(\vartheta, x, \eta, \sigma) e^{-\mu(\gamma-1)}, \tag{2.188}$$

where the weighting factors α and β from the scalar product (2.129) have been set to zero for simplicity. Here, the local Maxwellian was replaced by the relativistic Maxwell-Jüttner distribution,

$$f_{MJ}(r, u) = \frac{n}{v_T^3 \pi^{3/2}} \Theta(\mu) e^{-\mu(\gamma-1)}, \tag{2.189}$$

where $\mu = mc^2/T$ is the inverse relativistic temperature and

$$\Theta(\mu) = \sqrt{\frac{\pi}{2}} \frac{1}{\sqrt{\mu} K_2(\mu) e^{\mu}}, \tag{2.190}$$

is a normalization factor using the second order modified Bessel function of second kind K_2. For the numerical evaluation the Maxwellian form

$$\exp\left(-\mu(\gamma-1)\right) = \exp\left(-\frac{2x^2}{1 + \sqrt{1 + 2x^2/\mu}}\right) \tag{2.191}$$

is used, which is numerically more stable at low temperatures, i.e. where $\mu \gg 1$. It should be noted that in the non-relativistic case the initial (non-relativistic) form of the matrix elements is obtained because,

$$\lim_{T\to 0} \Theta(\mu) = 1, \tag{2.192}$$

$$\lim_{T\to 0} e^{-\mu(\gamma-1)} = e^{-x^2}. \tag{2.193}$$

Source term $q = q_3 = v\lambda B$, which is relevant for the Spitzer problem [2], stays unchanged in the relativistic case. Eq. (2.130) is finally modified to

$$\rho_{mm'} = \Theta(\mu) \int\limits_0^\infty \mathrm{d}x x^4 \gamma^{-1}(x) e^{-\mu(\gamma(x)-1)} \varphi_m(x) \varphi_{m'}(x) \tag{2.194}$$

resulting in multiplication of the whole drift kinetic equation with γ^{-1}.
While the differential part of Braams and Karney is complete (see Eq. (34) in Ref. 19), the integral part is given explicitly only for the first Legendre harmonic (see Eq. (38) in Ref. 19). However, in NEO-2 the Legendre expansion of the momentum conservation part is not restricted to an upper limit of L in Eq. (2.157). In previous investigations it has been observed that high order Legendre harmonics do not significantly influence the solution of the generalized Spitzer function, therefore, the implementation of the Braams and Karney collision operator is an important step for benchmarking to the code SYNCH which also uses an fully relativistic collision operator up to the first harmonic. Benchmarks of this upgraded collision model are presented in Chapter 4.

2.4.2 Direct evaluation of the Beliaev and Budker collision term

In order to investigate the influence of higher order Legendre harmonics a direct evaluation of the relativistic collision operator of Beliaev and Budker for an arbitrary upper limit of the Legendre expansion was derived by S. V. Kasilov [44]. The author of this thesis, G. Kapper, has implemented the matrix elements of this collision operator for NEO-2 following the procedure presented in Section 2.3.
While the differential part is the same as from Braams and Karney, the integral part consists of two-fold integrals which are numerically evaluated in the precomputation routine for the collision operator matrix elements of NEO-2. In this direct evaluation and in contrast to Eq. (38) from Ref. 19 the integral part takes the form,

$$
\begin{aligned}
\frac{n_b}{4\pi\Gamma}\hat{L}^{(I)} f_{b1} = & \frac{n_b}{4\pi\Gamma}\frac{\mathrm{St}(f_M(u), f_M(u) g_l(u) P_l(\lambda))}{P_l(\lambda)} \\
= & -\frac{1}{u^2}\frac{\partial}{\partial u} u^2 f_M(u) \int\limits_0^\infty \mathrm{d}u' u'^2 f_M(u') \left(\frac{1}{c} R_{11}^{(l)}(z,z') \frac{\partial g_l(u')}{\partial u'} + \frac{1}{c^2} R_{10}^{(l)}(z,z') g_l(u')\right) + \\
& + f_M(u) \int\limits_0^\infty \mathrm{d}u' u'^2 f_M(u') \left(\frac{1}{c^2} R_{01}^{(l)}(z,z') \frac{\partial g_l(u')}{\partial u'} + \frac{1}{c^3} R_{00}^{(l)}(z,z') g_l(u')\right),
\end{aligned}
\tag{2.195}
$$

where $\mathrm{St}(f_M, f_M g_l(u) P_l(\lambda))$ is the collision integral, and

$$
\Gamma = \frac{4\pi n_b e_a^2 e_b^2 \ln \Lambda_{ab}}{m_a^2}
$$

with n_b is the particle density of the background species, $\ln \Lambda_{ab}$ is the Coulomb logarithm, and respective functions in terms of $z = u/c$ variables are

$$
\begin{aligned}
R_{11}^{(l)}(z,z') &= \frac{1}{4}\int\limits_{-1}^{1} \frac{\mathrm{d}\xi}{\sqrt{r^2-1}} \left[\left(2r\xi + zz'\left(1-\xi^2\right)\right) P_l\left(\xi\right) - r\left(1-\xi^2\right) P_l'\left(\xi\right)\right], \\
R_{10}^{(l)}(z,z') &= \frac{1}{4z'}\int\limits_{-1}^{1} \frac{\mathrm{d}\xi}{\sqrt{r^2-1}} \left[r\left(\frac{\gamma z'}{\gamma' z} - \xi\right) l(l+1) P_l\left(\xi\right) + \right. \\
& \left. + \left(r + zz'\left(\frac{\gamma z'}{\gamma' z} - \xi\right)\right)\left(1-\xi^2\right) P_l'\left(\xi\right)\right], \\
R_{01}^{(l)}(z,z') &= R_{10}^{(l)}(z',z), \\
R_{00}^{(l)}(z,z') &= \frac{1}{4zz'\gamma\gamma'}\int\limits_{-1}^{1} \frac{\mathrm{d}\xi}{\sqrt{r^2-1}} \left(1-\xi^2\right) r \left[r l(l+1) P_l'(\xi) + \right. \\
& \left. + \ 2zz'\left(\xi P_l'(\xi) - l(l+1) P_l(\xi)\right)\right],
\end{aligned}
\tag{2.196}
$$

where $r = \gamma\gamma' - zz'\xi$. The numerical integration should be performed in terms of variable $y = \sqrt{r-1} = \sqrt{\gamma\gamma' - 1 - zz'\xi}$,

$$\int\limits_{-1}^{1} \frac{\mathrm{d}\xi}{\sqrt{r^2-1}} [\ldots] = \frac{2}{zz'} \int\limits_{\sqrt{\gamma\gamma'-1-zz'}}^{\sqrt{\gamma\gamma'-1+zz'}} \frac{\mathrm{d}y}{\sqrt{r+1}} [\ldots] , \tag{2.197}$$

so that $r = 1 + y^2$ and $\xi = (\gamma\gamma' - 1 - y^2)/(zz')$. For numerics it is better to present

$$\gamma\gamma' - 1 = \frac{z^2 + z'^2 + z^2 z'^2}{\gamma\gamma' + 1}. \tag{2.198}$$

It can be analytically verified that for $l = 1$ the form of Braams and Karney is obtained. The representation (2.196) of the integral kernel is numerically more stable as compared to the analytical result of Braams and Karney where cancellations of large numbers occur at mild relativistic energies, and this problem gets more severe with the increase of the Legendre polynomial index. In Chapter 4 the influence of these higher order Legendre harmonics on the solution is discussed.

Chapter 3

Solution of the generalized Spitzer problem with an upgraded NEO-2 code package

In this chapter the solution of the generalized Spitzer problem with an upgraded NEO-2 code package is described. Parts of Sections 3.1, 3.2, and 3.3 have been published in the meantime in the following journal publication, however they are described in this thesis in more detail:

- G. Kapper, S. V. Kasilov, W. Kernbichler, A. F. Martitsch, M. F. Heyn, N. B. Marushchenko, and Y. Turkin, "Electron cyclotron current drive simulations for finite collisionality plasmas in Wendelstein 7-X using the full linearized collision model", Physics of Plasmas **23**, 112511 (2016)

Contents of this chapter

3.1 Distribution function for full linearized collision model 63
3.2 Parallelized precomputation of a profile 64
3.3 Reconstruction of the generalized Spitzer function in phase space . . . 68
3.4 Summary 70

3.1 Distribution function for full linearized collision model

As introduced in Section 2.3 the velocity module dependence of the NEO-2 solution to the integro-differential current drive problem,

$$v\lambda h^{\vartheta}\frac{\partial f_M g_3}{\partial \vartheta} - \hat{L}_C f_M g_3 = v_{\parallel} B f_M \tag{3.1}$$

is expanded over a complete set of test functions $\varphi_m(x)$ based on the Galerkin method,

$$g_3(\vartheta, x, \lambda) = \sum_{m=0}^{M} g_{3,m}^{\sigma}(\vartheta, \eta(\vartheta, \lambda))\varphi_m(x), \tag{3.2}$$

where x is the normalized velocity (see Eq. (2.122)), $M+1$ is the number of basis functions, and σ is the parallel velocity sign. The expansion coefficients $g_{3,m}^{\sigma}(\vartheta, \eta)$ of the generalized Spitzer function are computed by NEO-2 using a conservative 2D finite difference scheme of third order over the normalized perpendicular adiabatic invariant η and of the first order over the field line parameter ϑ with an adaptively refined η-grid in order to resolve all local boundary layers of different classes of trapped particles as well as the global trapped-passing boundary. Such an adaptive grid is especially required in the long mean free path regime, where the collisionality parameter $L_c/l_c \ll 1$, where $L_c = 2\pi R_0$ is the connection length with R_0 being the major radius of the device. While in axisymmetric tokamaks all trapped particles are separated from passing particles by the global trapped-passing boundary defined by the global field maximum, in stellarators local magnetic field maxima form additional boundaries for different classes of trapped particles. Resolution of all local boundaries of classes of trapped particles with one global grid would lead to unfeasible memory consumption and as a consequence thereof to very long computation times. This adaptive grid is built using a base grid uniformly distributed in η with subsequent binary splitting of domains of two neighboring levels. The density of levels around local boundaries depends on the collisionality parameter because the scale of the solution over η is given as $\delta\eta B \sim \sqrt{L_c/l_c}$ so that lower collisionality requires denser levels. For small collisionalities, levels of constant η have to reach deeper into neighboring field ripples because of smaller scattering probability. Examples of the adaptively refined η-grid are shown in Figure 3.1 for a standard configuration as well as for a high-mirror configuration of Wendelstein 7-X for two different collisionalities. In addition, in these figures the field period boundaries (solid vertical lines) and field ripple boundaries (solid dotted lines) are depicted. The latter ones can be solved independently and are finally joined to a final solution based on multiple domain decomposition allowing for parallelization of the code [2].

As described in Section 2.3 in previous versions of NEO-2, the basis functions $\varphi_m(x)$ in Eq. (3.2) were fixed to generalized Laguerre polynomials of order 3/2 (Sonine polynomials). This choice was not an intrinsic limitation of the code and has been overcome in the course of this thesis allowing the usage of an arbitrary complete set of basis functions, which are not necessarily orthogonal. For the computation of flux surface averaged neoclassical diffusion coefficients in stellarators, the typical number of basis functions required is 4 to 6, corresponding to $M = 3$ to $M = 5$, respectively. As also shown in Section 2.3, a further increase of the number of Sonine polynomials results in an expansion of the solution by high order polynomials which tend to diverge at higher velocities. However, for the computation of the distribution function for ECCD applications, a stable computation up to five times the thermal velocity is necessary, which is computationally a rather difficult task when using a polynomial basis. In contrast to Sonine polynomials, which are globally defined on the whole velocity space, the usage of local basis functions, such as B-splines, allows to increase the upper velocity limit and the velocity resolution using the same number of basis functions as with the Sonine basis. For the computations of the generalized Spitzer function it turned out that cubic B-splines form a well-suited basis. Another application of NEO-2 such as the investigation of neoclassical toroidal viscosity (NTV) in non-axisymmetric tokamaks [3] make it necessary to use low order basis splines, e.g., first order splines (hat functions), in order to resolve resonances accurately. These approaches and the pertinent numerical schemes are presented in detail in Ref. 2 while benchmarks are presented in Chapter 4 of this thesis.

3.2 Parallelized precomputation of a profile

Starting from a given magnetic equilibrium with pertinent plasma parameter profiles for temperature, density, and effective charge, the high dimensionality of the problem makes the precomputation of NEO-2 results inevitable. Therefore, the local NEO-2 solutions are precomputed on a prescribed set of flux surfaces, where on each flux surface the drift

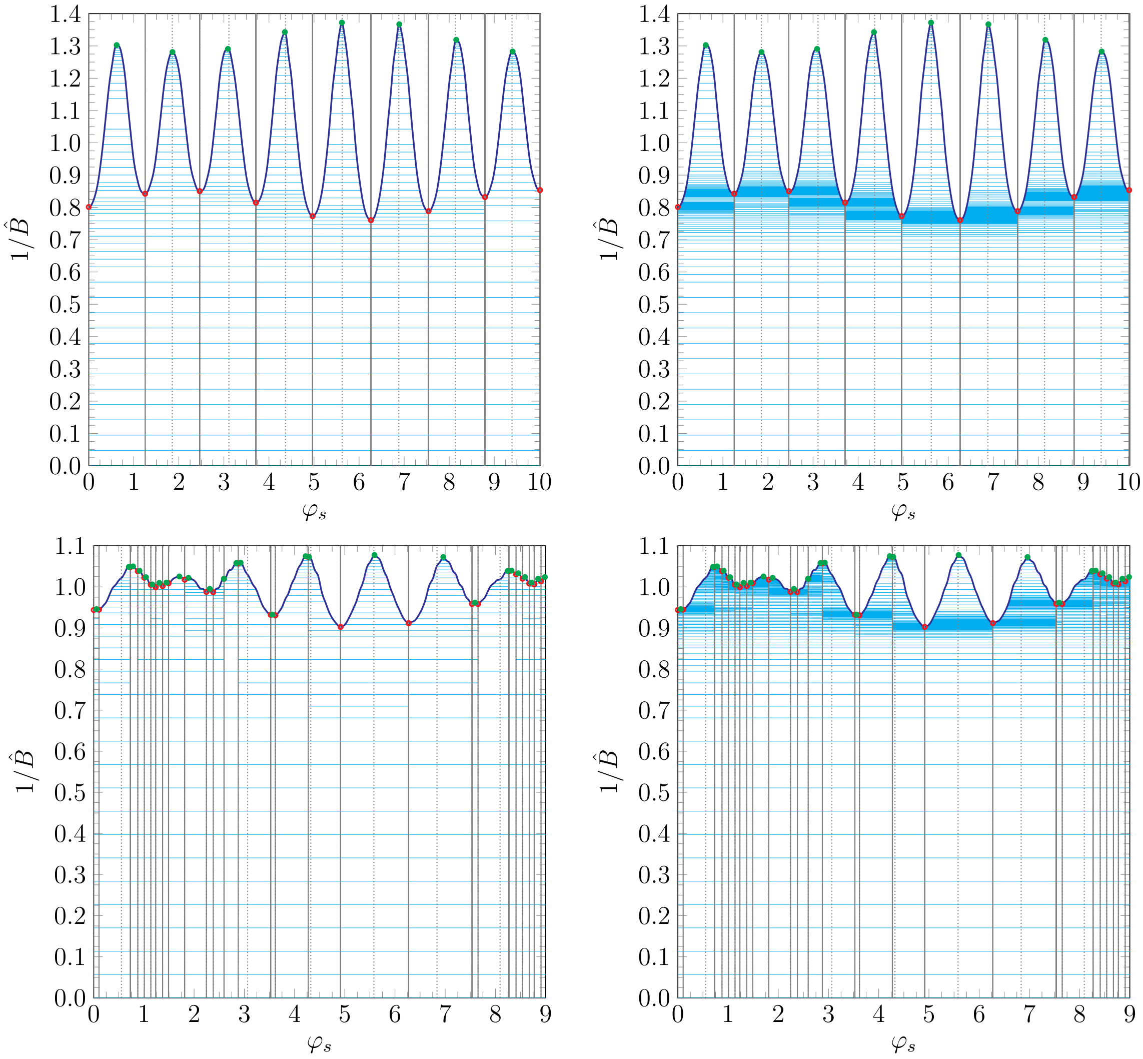

Figure 3.1: Distribution of adaptively refined η-levels along the field line at collisionality $L_c/l_c = 1$ (left) and $L_c/l_c = 10^{-3}$ (right) in a standard configuration (upper plots) and a high-mirror configuration (lower plots) of Wendelstein 7-X. Ripple boundaries and toroidal field period boundaries are depicted as vertical solid and dashed lines, respectively. Local field minima of $\hat{B} = B/B_{\text{ref}}$ are indicated as green dots, while local field maxima are indicated as red circles.

kinetic equation is solved along a single field line with plasma collisionality according to the given profiles. The number of traced toroidal field periods N_t until the field line is closed artificially, defines the poloidal accuracy of the reconstruction process of the distribution function. The prescribed set of flux surfaces is chosen in such a way that $N_t \gg 1$ for all flux surfaces. For the given high-mirror equilibrium of Wendelstein 7-X as used for ECCD simulations in Chapter 5 the condition $200 \leqslant N_t \leqslant 400$ has been defined. The lower boundary guarantees an accurate computation so that the field line is not closed after only a few toroidal periods, whereas the upper boundary keeps memory and runtime treatable.

In a first step, these flux surfaces are uniformly distributed in the normalized toroidal flux s and are, if necessary, shifted from its initial distribution to avoid computation close to low-order rational flux surfaces. This is important to avoid a closure of the field line after only a few toroidal periods, which would result in poor poloidal resolution and, as a consequence, in extremely low accuracy of the flux surface averages. As seen from Figure 3.2, the restriction to an intended number of periods is not possible with a purely uniform distribution due to resonances, therefore, the distribution is adaptively modified. Since the restriction can not be fulfilled everywhere without significantly violating the initial uniform distribution, a slightly larger number of periods is accepted for some values of s. The resulting set of flux surfaces and pertinent collisionality parameters computed from plasma parameter profiles is then used as an input for one NEO-2 run per flux surface. The precomputed solution on a dense mesh in phase space leads to rather large amounts of data ($\sim 100 - 200$ GB per configuration and pertinent profile) stored in the HDF5 file format [45]. Since these data should be used as input also for other applications, the focus was on the development of an interface allowing straightforward access to the precomputed results as described in the following section.

The precomputation of the generalized Spitzer function and other distribution functions in stellarators is a high dimensional problem. Its solution has only become possible due to the parallelization of the stellarator branch of NEO-2. This feature has been developed in the scope of the Master Thesis of the author of this thesis together with W. Kernbichler (see Ref. 46 for technical details on the parallelization using the Message Passing Interface (MPI) [47]). The parallelization of the stellarator branch of NEO-2 is based on multiple domain decomposition along a traced field line, where the field line is separated into domains which can be solved independently of each other. The number of computing nodes defines how many domains of the field line can be solved

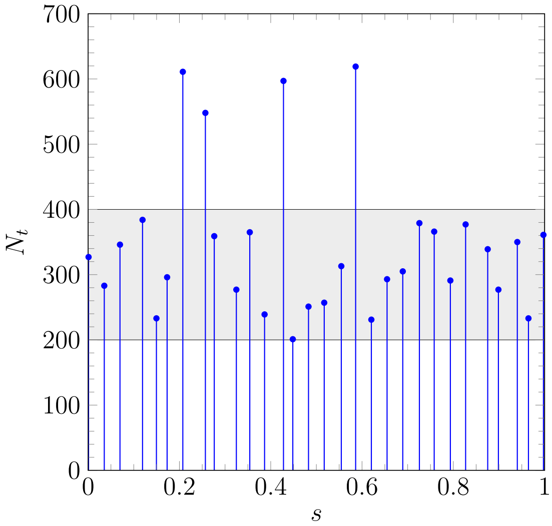

Figure 3.2: Total number of toroidal field periods N_t as a function of the normalized toroidal flux s. The gray band indicates the intended lower and upper limits, respectively, for precomputation. (From G. Kapper, et al. [1])

at the same time and therefore determines the overall code speedup. However, due to Amdahl's law [48] and its generalization for the multicore era [49] there is a limit for the maximum speedup determined by the sequential part of the code which can not be parallelized. A typical runtime of NEO-2 for the precomputation of one flux surface with sufficient spatial resolution is 6 hours on 32 computing nodes. The parallelization is written in a way that one process acts as a scheduler which handles the distribution of field line domains to be solved simultaneously as well as performs load balancing across the nodes. The latter is important because different domains of the field line have different numerical complexity because of the adaptive level placement as described in Section 3.1. This load balancing also ensures optimal work distribution for the case that not all nodes come up with the same computational power. Without parallelization the precomputation of a local solution would have required more than 7 days instead of 6 hours. The final joining of the partial solutions of each field line domain and the pertinent rediscretization scheme is presented in detail in Ref. 2.

This kind of parallelization is different from the parallelization of the quasilinear multi-species version of NEO-2. While for the stellarator branch a higher number of cores means shorter runtime (respecting Amdahl's law), the multi-species version solves the linearized drift kinetic equation for each species on a separate computing node. The solutions of different species are coupled to each other within the integral part of the collision operator. Therefore, the processes have to exchange their solutions only within the direct or pre-conditioned iterations of the solution of the integral part. The solution of a multi-species problem with a large number of different species and pertinent ionization stages is a rather memory-intensive operation. However, the parallelization of this code version, which uses the same library based on MPI as it has been developed for the stellarator version, allocates a separate memory space for the solution of each species. Thus, the usage of processes on different computing nodes not only allows for a speedup of the code, but also allows for distribution of the allocated memory to different computing nodes [31].

3.3 Reconstruction of the generalized Spitzer function in phase space

For electron cyclotron current drive simulations the generalized Spitzer function acting as a current drive efficiency in phase space has to be evaluated along a microwave beam propagating through the plasma. Therefore, it has to be known for any point $(\mathbf{x}, v, \lambda)$ in phase space, where $\mathbf{x} = (s, \vartheta_b, \varphi_b)$ are Boozer coordinates being the normalized toroidal flux, poloidal and toroidal angles, respectively. From the local solution of the linear current drive problem, $g_3(\vartheta, v, \lambda)$, the solution to the 5D problem is reconstructed by linear interpolation over the radial coordinate and over the periodic Boozer angles. These periodic Boozer angles are related to the field line parameter ϑ via the relations,

$$\vartheta_b = \vartheta_0 + \vartheta, \qquad \varphi_b = \varphi_0 + \frac{\vartheta - \vartheta_0}{\iota}, \tag{3.3}$$

where ϑ_0 and φ_0 are the starting points of the field line and ι is the rotational transform. The values of ϑ, where the drift kinetic equation is solved, are adaptively distributed by the solver. Transformations of the field line parameter to Boozer coordinates as given in Eq. (3.3) results in Figure 3.3, where a zoomed depiction of points where the problem is actually solved is given. It should be noted that the depiction of a whole flux surface with $0 < \vartheta_b < 2\pi$ and $0 < \varphi_b < 2\pi/N$ ($N = 5$ for Wendelstein 7-X) would result in a grid which size can be estimated with $N_t \times N_{\varphi_b}$, where typical values are $N_t = 400$ and $N_{\varphi_b} = 600$. In the center of the figure an arbitrary point of interest is marked by a cross in order to indicate the required points of precomputed values for linear interpolation. First, interpolation along two segments on the same field line enclosing the point is performed, while in a second step interpolation is done in the poloidal direction apart from the field line. Since the point of interest will usually be located between two precomputed flux surfaces, this procedure is performed on two flux surfaces enclosing the point with subsequent radial interpolation. As a consequence, one spatial point requires eight precomputed values of NEO-2. The use of linear interpolation is justified by the dense grid in periodic Boozer angles and the sufficiently large number of flux surfaces.

In order to find the relevant precomputed data points to a requested point on the 3D $(s, \vartheta_b, \varphi_b)$-grid, fast lookup routines based on binary search were implemented. The coefficients to reconstruct the distribution function, $g^{\sigma}_{3,m}(\vartheta, \eta(\vartheta, \lambda))$, are read from the data-base using special features of the HDF5 library where only portions of a dataset (so-called hyperslabs [45]) are read in order to reduce disk operations. In order to speedup consecutive calls of the interface, all required information for interpolation of the previous spatial point is cached as long as the spatial position does not change. The time for querying one spatial point is of the order of milliseconds as shown in a benchmark presented in Appendix B, while the evaluation of several velocities takes almost no extra time due to the described data caching.

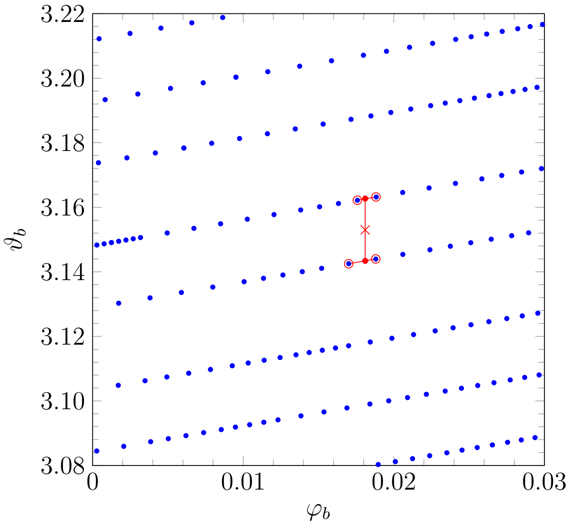

Figure 3.3: Depiction of precomputed data points (•) by NEO-2 on a single flux surface. An arbitrary point of interest (×) is shown, where the required data points for interpolation are highlighted (○). The non-equal spacing of the data points is a consequence of the adaptive level placement in NEO-2 as can be seen from Figure 3.1. (From G. Kapper, et al. [1])

3.4 Summary

The linearized drift kinetic equation solver NEO-2 has been upgraded allowing for an efficient computation and storage of the distribution for tokamaks and stellarators. Here, in particular for current drive simulations, the computation of the distribution function driven by the parallel electric field, also referred to as generalized Spitzer function, is of interest. The implementation of those upgrades was coupled with the development of an interface to access to the high-dimensional precomputed NEO-2 results. This interface can be used as a standalone program, e.g., for plotting the distribution function, as well as as a library in other codes. The latter possibility made possible the integration of NEO-2 in the ray-tracing code TRAVIS (TRAcing VISualized) [22] as explained in more detail in Chapter 5. Up to this upgrade, the NEO-2 results were stored as classical text files. While this is sufficient for scalar quantities and smaller matrices, the high dimensionality of distribution functions led to the migration of the output format to binary HDF5 files [45]. This transition of the file format not only brings the advantage that a lot of output files can be merged to one file which is easy to handle, it also features fast lookup routines for efficient access to large datasets. As described in Section 3.2 the precomputation of the generalized Spitzer function for a given magnetic equilibrium with pertinent plasma parameter profiles results in files up to several hundred Gigabytes. However, the implemented fast lookup routines allow for fast data access. Therefore, the usage of the NEO-2 interface does not significantly harm the interactive usage of TRAVIS or other applications.

Chapter 4

Benchmarking and studies of asymptotical limits

In Chapter 2 the numerical problem has been formulated, while in the previous Chapter 3 the code NEO-2 has been applied to the numerical problem. In this chapter neoclassical transport coefficients and the generalized Spitzer function are computed by NEO-2 and benchmarked against asymptotical collisionality limits. The studies on the mono-energetic bootstrap coefficient in Section 4.1 have been published in the following journal publication, where minor modifications have been made here:

- W. Kernbichler, S. V. Kasilov, G. Kapper, A. F. Martitsch, V. V. Nemov, C. Albert, and M. F. Heyn, “Solution of drift kinetic equation in stellarators and tokamaks with broken symmetry using the code NEO-2”, Plasma Physics and Controlled Fusion **58**, 104001 (2016)

Benchmarks of the fully relativistic Coulomb collision operator as shown in Section 4.3 have been published in an internal EUROfusion report formulated by the author of this thesis:

- G. Kapper, S. V. Kasilov, W. Kernbichler, A. F. Martitsch, and N. B. Marushchenko, *Implementation of the fully relativistic full linearized Coulomb collision model in the code NEO-2 for ECCD modeling in tokamaks and stellarators with finite plasma collisionality*, Technical Report (EUROfusion, 2017)

Contents of this chapter

4.1 Mono-energetic neoclassical transport coefficients in the $1/\nu$ regime . . 73
  4.1.1 Diffusion and bootstrap coefficients, effective ripple and Shaing-Callen limit 73
  4.1.2 Convergence of NEO-2 with and without adaptive grid 76
4.2 Benchmarking of the distribution function 77
  4.2.1 Overview 77
  4.2.2 Collisionless limit 77
  4.2.3 High-collisionality limit 84
  4.2.4 Finite collisionality 86
4.3 Benchmarking with relativistic collision operator 90

4.1 Computation of mono-energetic neoclassical transport coefficients in the $1/\nu$ regime

Originally, NEO-2 was developed for the computation of mono-energetic neoclassical transport coefficients in stellarators [50] and for the computation of distribution functions in tokamaks [18]. Recent progress such as the development of a quasilinear code version for non-axisymmetric tokamaks [3, 37] as well as ongoing technical improvements such as parallelization techniques for a more efficient computation of the generalized Spitzer function in stellarators [2, 7] resulted in a more general version of the code. Results of this upgraded version of the code are presented in the following sections.

4.1.1 Diffusion and bootstrap coefficients, effective ripple and Shaing-Callen limit

In Figure 4.1 two normalized mono-energetic transport coefficients as computed with NEO-2, namely, the diffusion coefficient, D^*_{11}, and the bootstrap coefficient, D^*_{31}, are shown for the Wendelstein 7-X standard configuration as functions of the collisionality parameter $\nu^* = R_0/(\iota l_c)$, where R_0 is the major radius and $l_c = v/\nu_D(v)$ is the mono-energetic mean free path with $\nu_D(v)$ being the deflection frequency. The device configuration and the normalization of the coefficients as well as the definition of ν^* are the same as in Ref. 50, $D^*_{11} = D_{11}/D^p_{11}$ and $D^*_{31} = D_{31}/D^b_{31}$, where D^p_{11} and D^b_{31} are transport coefficients in the equivalent tokamak in plateau and banana regimes, respectively. While for the computations in Ref. 50 only the sequential version of NEO-2 existed, for the results shown in this chapter the parallelized version has been applied allowing for investigations at much smaller collisionalities.

For the comparison, asymptotical values of transport coefficients computed by the code NEO in the $1/\nu$ regime are shown where D_{11} and D_{31} are computed according to Ref. 36 via the standard neoclassical formula with effective ripple modulation representing the device geometry and Refs. 51, 52 where the Shaing-Callen limit value for bootstrap coefficient is presented, respectively. In contrast to D^*_{11} which quickly reaches the asymptotical value when reducing collisionality, the bootstrap coefficient D^*_{31} remains different from the asymptotic value even if ν^* is smaller than one by many orders of magnitude. This trend has been shown earlier in Ref. 50 for a few different

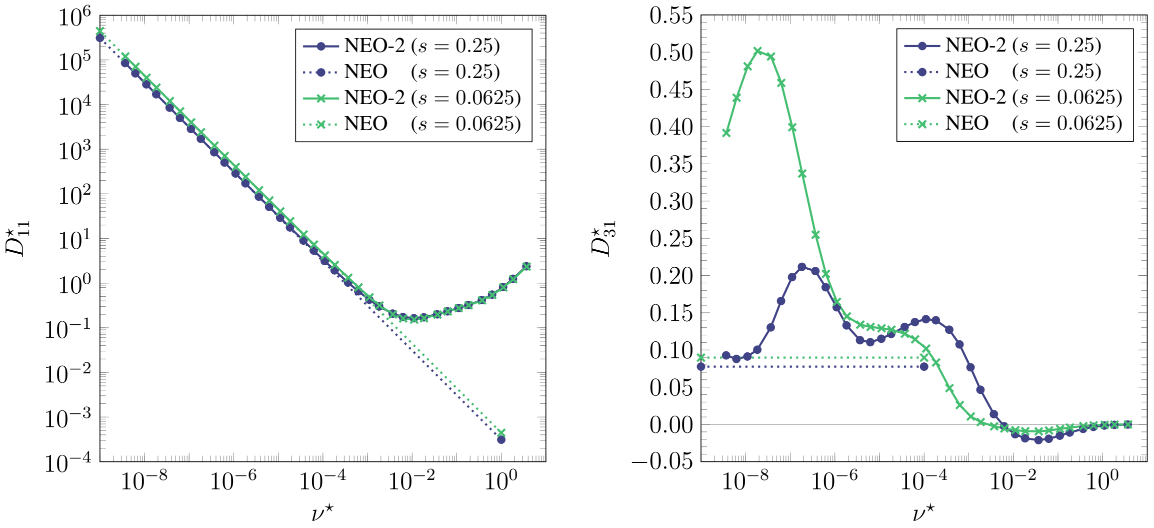

Figure 4.1: Normalized mono-energetic radial transport coefficient $D^\star_{11}$ (left) and normalized mono-energetic bootstrap current coefficient $D^\star_{31}$ (right) as a function of collisionality computed by NEO-2 (solid) for finite collisionalities and by NEO (dotted) for the collisionless limit at half radius $s = 0.25$ (circles) and quarter radius $s = 0.0625$ (crosses). Markers on the solid lines correspond to results of NEO-2 runs at given collisionalities. (From W. Kernbichler, et al. [2])

configurations up to $\nu^* \sim 10^{-6}$, and is seen here up to $\nu^* = 3 \cdot 10^{-9}$. It has been also shown there that even a small $\mathbf{E} \times \mathbf{B}$ rotation allows to reach the asymptotical value of D^*_{31} (see Figure 26 of Ref. 50 for respective Wendelstein 7-X dependencies). Such a behavior of D_{31} is not a computational artifact which could be expected at extremely low collisionalities. It is well reproduced for different field line settings (starting point and number of periods) and different base grid parameters (resulting finally in different adaptively refined η-grids). The result well fulfills the Onsager symmetry ($D_{31} = D_{13}$). This is not an intrinsic property of the NEO-2 discretization scheme but is used instead as a convergence measure [2]. Deviations of D_{31} from the ideal $1/\nu$ limit are caused by a collisional effect of trapped particles on the passing particle distribution. This effect is fully ignored in analytical theory for infinitesimal collisionalities when setting for the passing particle distribution function g_1 (driven by the source $q_1 = -v^r_g$, see Eq. (2.59)) the boundary condition at the trapped-passing boundary where g_1 is assumed to be equal to the collisionless radial displacement of the orbit starting at the flux surface on the global maximum point (see also Ref. 53). At this point the parallel velocity is zero for transient particles and, respectively, co- and counter-passing distribution functions are equal. In this ideal picture the trapped particle region is excluded from the formation of the bootstrap current and contributes only to the Pfirsch-Schlüter current. The distribution of the latter current over velocity space represented by $g_1^a = (g_1^+ - g_1^-)/2$, being the odd part of g_1 with respect to pitch parameter, is rather peculiar in stellarators (see Figure 4.2). A significant part of this current flows in the trapped region within boundary layers $\eta \approx \eta_i$ separating different trapped particle classes. In these layers g_1^a scales as $\nu^{-1/2}$ in case of finite collisionality and turns into a δ-function in the infinitesimal collisionality limit, $g_1^a \sim \delta(\eta - \eta_i)$. If this limit is enforced, all η_i layers are clearly separated from the passing particle region and do not influence the passing particle distribution. However, for any small but finite collisionality, always classes exist at irrational flux surfaces with a boundary layer widths comparable to the distance from η_i to the trapped-passing boundary. Contributions from such boundary layers effectively modify the passing particle distribution at the trapped-passing boundary and thus modify the value of the bootstrap current.

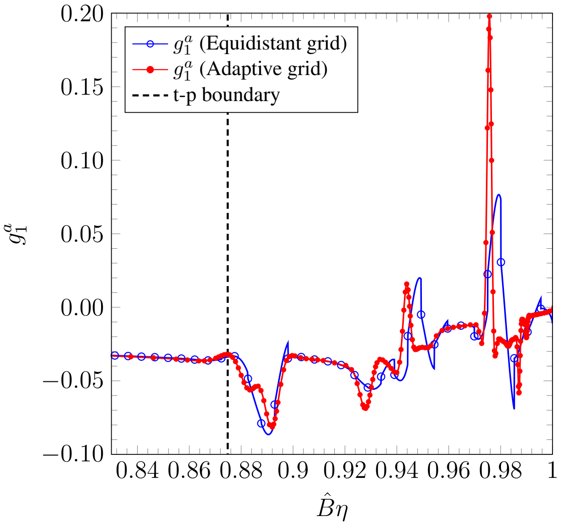

Figure 4.2: Odd part of the gradient driven distribution function, g_1^a, at the position on the field line between distinct maxima computed with adaptive (•) and corresponding equidistant (○) grid as a function of $\hat{B}\eta$ where $\hat{B} = B/B_{\text{ref}}$. The η-level positions are depicted as circles on top of the corresponding curves. Value $\hat{B}\eta = 1$ corresponds to particles reflected at the observation point and the trapped-passing boundary is shown with a vertical dashed line. (From W. Kernbichler, et al. [2])

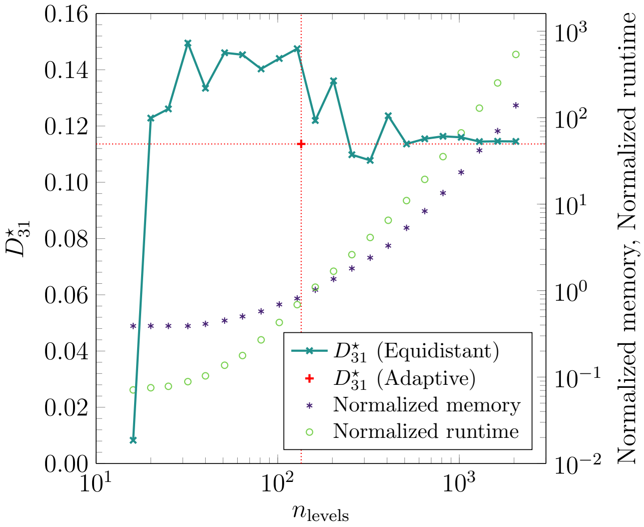

Figure 4.3: Normalized mono-energetic bootstrap current coefficient $D_{31}^{\star}$ for collisionality $\nu^{\star} = 3.66 \cdot 10^{-6}$ at half radius as a function of the number of equidistant η-levels compared to the solution using an adaptive grid. For the adaptive grid a mean number of levels along the field line is indicated as vertical dotted line. In addition the normalized peak memory requirements and normalized runtime with respect to a run with adaptively placed levels is given. (From W. Kernbichler, et al. [2])

4.1.2 Convergence of NEO-2 with and without adaptive grid

In order to demonstrate the advantage of an adaptive η-grid a convergence test of the normalized mono-energetic bootstrap current coefficient $D_{31}^{\star}$ for collisionality $\nu^{\star} = 3.66 \cdot 10^{-6}$ ($L_c/l_c = 2 \cdot 10^{-5}$) at half radius has been performed using an equidistant and an adaptive grid. As can be seen in Figure 4.3, a computation with an equidistant grid requires one order of magnitude more η-levels than with an adaptive scheme to ensure convergence of the solution. In order to provide a direct comparison of runtime and peak memory consumption between the equidistant and the adaptive scheme, normalized runtime and normalized peak memory with respect to a corresponding run with a standard configuration of NEO-2 using an adaptive grid are presented. It should be noted that the peak memory is not necessarily allocated during the whole runtime of the code, however it indicates the maximum memory which has to be available during the runtime on a computing cluster. While absolute numbers for runtime and memory consumption strongly depend on the used computing infrastructure, in order to give an impression of the overall code performance absolute values are given here for the reference run. On a 64-bit Intel(R) Xeon(R) architecture the runtime using 8 parallel processes, where one process acts as scheduler, took 730 seconds with an average peak memory consumption of 450 Megabytes per process. The parallelization of NEO-2 with almost ideal speedup allows a much higher number of parallel processes, however, as a consequence of the high memory demands of the non-adaptive equidistant grid used for benchmarking, all runs were performed on the same high-memory machine with less cores. In addition, in Figure 4.2 a comparison of the odd part of the gradient driven distribution function, g_1^a, computed with an equidistant and adaptive grid at a spatial point between two distinct maxima, where few classes of trapped particles exist, is presented. Two equivalent runs are compared, i.e., number of equidistant levels conforms to the number of adaptively placed levels at this particular point on the field line, however, it can be seen that important features of the distribution function can only be captured by a refinement of the grid at pertinent boundary layers [2].

4.2 Benchmarking of the distribution function

4.2.1 Overview

The generalized Spitzer function is well known in asymptotical collisionality limits, namely in the collisionless limit where 2D bounce average procedures can be applied [12] as well as in the high-collisionality limit where the classical Spitzer function [13] is valid. In both limits, the function is strictly antisymmetric in the pitch angle $\lambda = v_\parallel / v$ at any spatial position. However, in a plasma with finite collisionality the generalized Spitzer function no longer has this trivial dependence on the spatial position. In the following sections, benchmarks against the asymptotical collisionality limits using different sets of basis functions as they have been introduced in Section 2.3.5 are presented for a model tokamak with concentric circular flux surfaces and for the stellarator Wendelstein 7-X. Furthermore, results for finite plasma collisionality are studied.

4.2.2 Collisionless limit

In this section results computed by NEO-2 for different sets of basis functions for collisionality $L_c/l_c = 10^{-3}$, where L_c is the connection length and l_c is the mean free path, are benchmarked against the collisionless limit computed by the code SYNCH, which is a fully relativistic solver of the Spitzer problem in the long mean free path limit for arbitrary 3D toroidal geometries [12]. An effective charge

$$Z_{\text{eff}} = \frac{1}{n_e} \sum_i n_i Z_i^2 = 1 \tag{4.1}$$

is assumed, where n_e is the electron density, and n_i and Z_i are density and charge of ion species i, respectively, where the sum is over all ion species.

In Figures 4.4 and 4.5 the generalized Spitzer function is plotted as a function of the normalized velocity for $\lambda = 1$ at the field maximum of the model tokamak. As is evident from Figure 4.4, where the solution is expanded in terms of Sonine polynomials, a higher number of basis functions does not necessarily mean a more accurate solution. Obviously, a higher number of Sonine polynomials also introduces high order polynomials which cause numerical instabilities. This behavior can be seen from plots (see Figure 2.1) of these basis functions which start to diverge at higher velocities.

In contrast, results obtained with cubic B-splines as basis functions exhibit a more stable solution at high velocities. In the left plot of Figure 4.5 the knots of the B-spline are uniformly distributed in the domain $0 \leqslant x \leqslant 4$ whereas in the right plot $0 \leqslant x \leqslant 5$ is used. Subsequent Taylor expansion is applied in both cases. The analytical solution is well matched for $M = 7$ and $M = 9$ for both knot distributions, while the basis

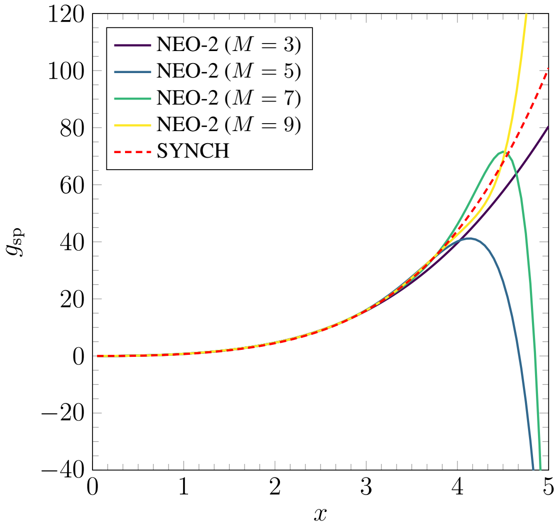

Figure 4.4: Convergence of the NEO-2 solution (solid lines) for the generalized Spitzer function with respect to the number of Sonine polynomials as a function of the normalized velocity $x = v/v_T$ at pitch angle $\lambda = 1$ for the model tokamak. In addition the collisionless limit computed by SYNCH (dashed line) is shown for comparison.

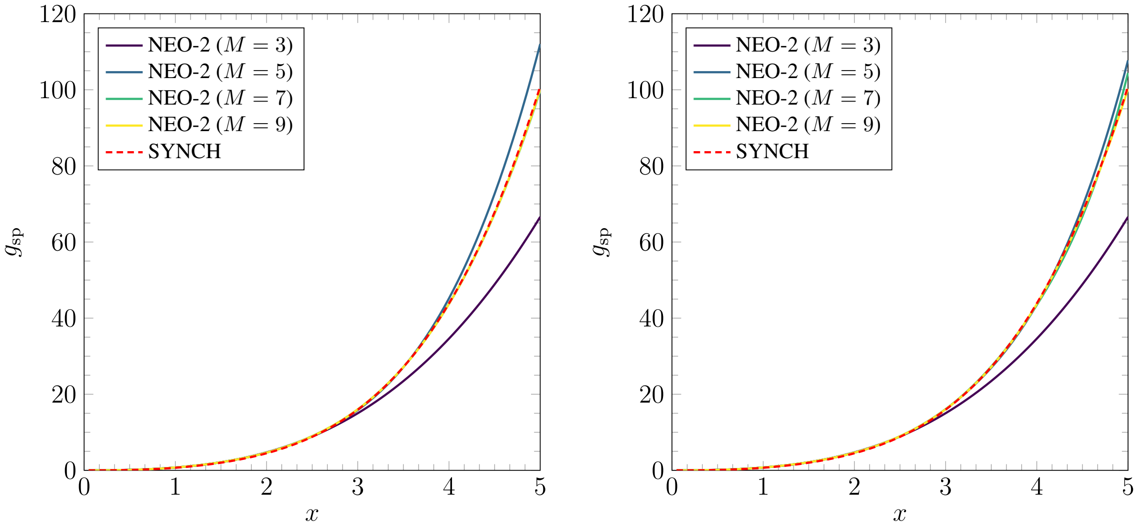

Figure 4.5: Same as in Figure 4.4 but computed with cubic B-splines defined in domain $0 \leqslant x \leqslant 4$ (left) and defined in domain $0 \leqslant x \leqslant 5$ (right) with subsequent Taylor expansion for both.

defined up to $x = 5$ sufficiently represents the high velocity limit already with $M = 5$. In contrast to Sonine polynomials, it is indicated that a higher number of B-splines leads to a more accurate result.

In Figures 4.6 and 4.7 the generalized Spitzer function for a tokamak at the field maximum is plotted against the pitch angle parameter for three different particle velocities and for the same three sets of basis functions as before. As expected the collisionless limit is approached at higher velocities, however, at $x = 5$ the high order Sonine polynomials fail to represent the solution correctly. This is different from the results where the solution is expanded in terms of B-splines. However, it has to be noted that at intermediate velocity ($x = 3$) the solution expanded via Sonine polynomials is better than the respective solution expanded in terms of B-splines. This can be understood because for $M = 3$ the cubic B-splines are constructed with only two knots ($t_1 = 0$, $t_2 = 4$ for Figure 4.7 (left) and $t_1 = 0$, $t_2 = 5$ for Figure 4.7 (right), respectively). This results in a poor resolution for intermediate velocities and consequently a bad result for the whole velocity domain. In Figures 4.8 and 4.9 the same is shown, however, for the field minimum, where the trapped-passing boundary is clearly visible. The conclusion is the same as for the field maximum.

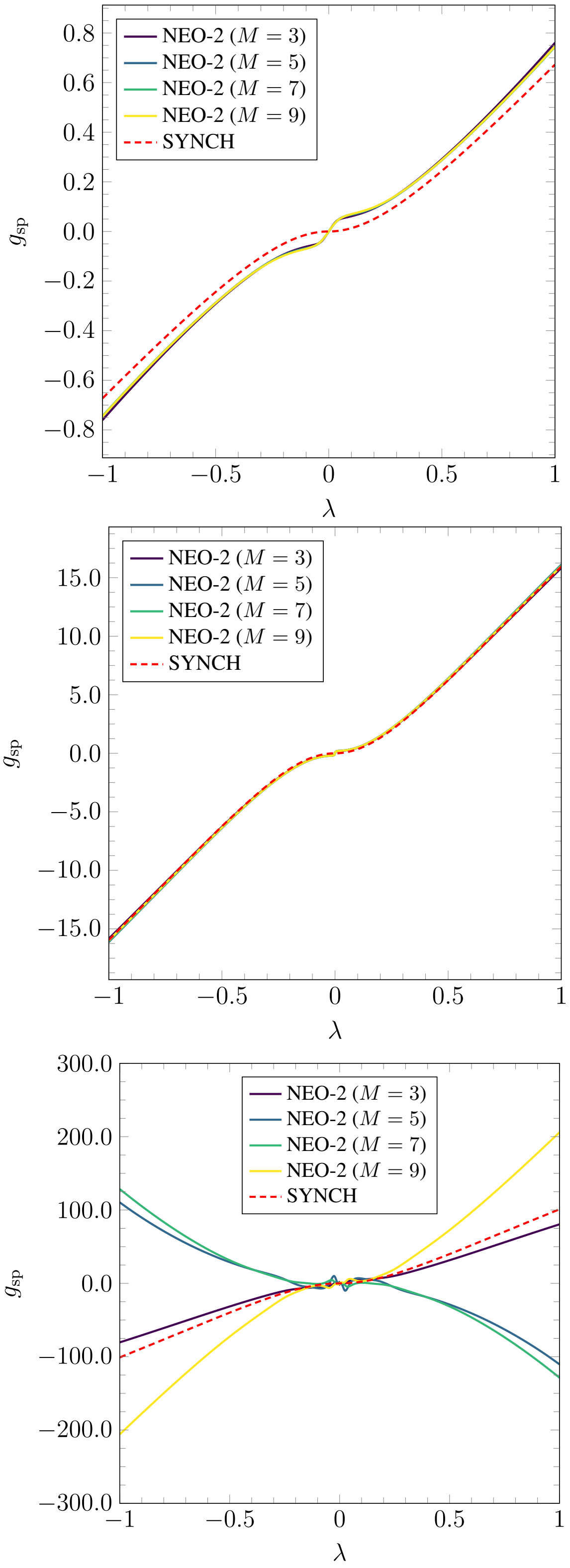

Figure 4.6: Generalized Spitzer function as a function of the pitch angle parameter $\lambda = v_{\parallel}/v$ at the field maximum of the model tokamak for particles at velocities $x = 1$, $x = 3$, and $x = 5$ (from top to bottom). The NEO-2 results (solid lines) have been computed with Sonine polynomials. Results in the collisionless limit from SYNCH (dashed lines) are shown for comparison.

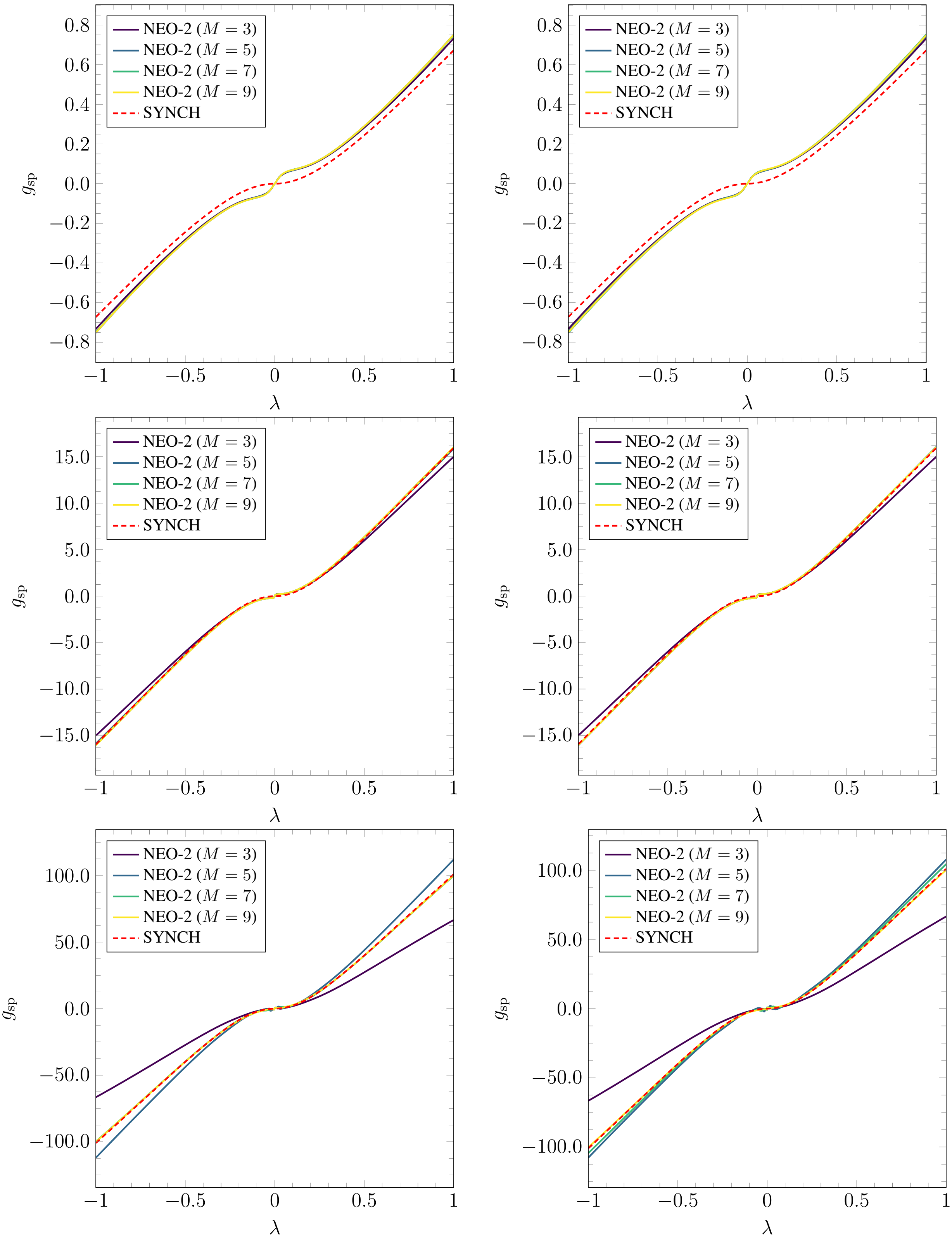

Figure 4.7: Same as in Figure 4.6 but computed with cubic B-splines defined in the domain $0 \leqslant x \leqslant 4$ (left) and defined in domain $0 \leqslant x \leqslant 5$ (right) with subsequent Taylor expansion for both.

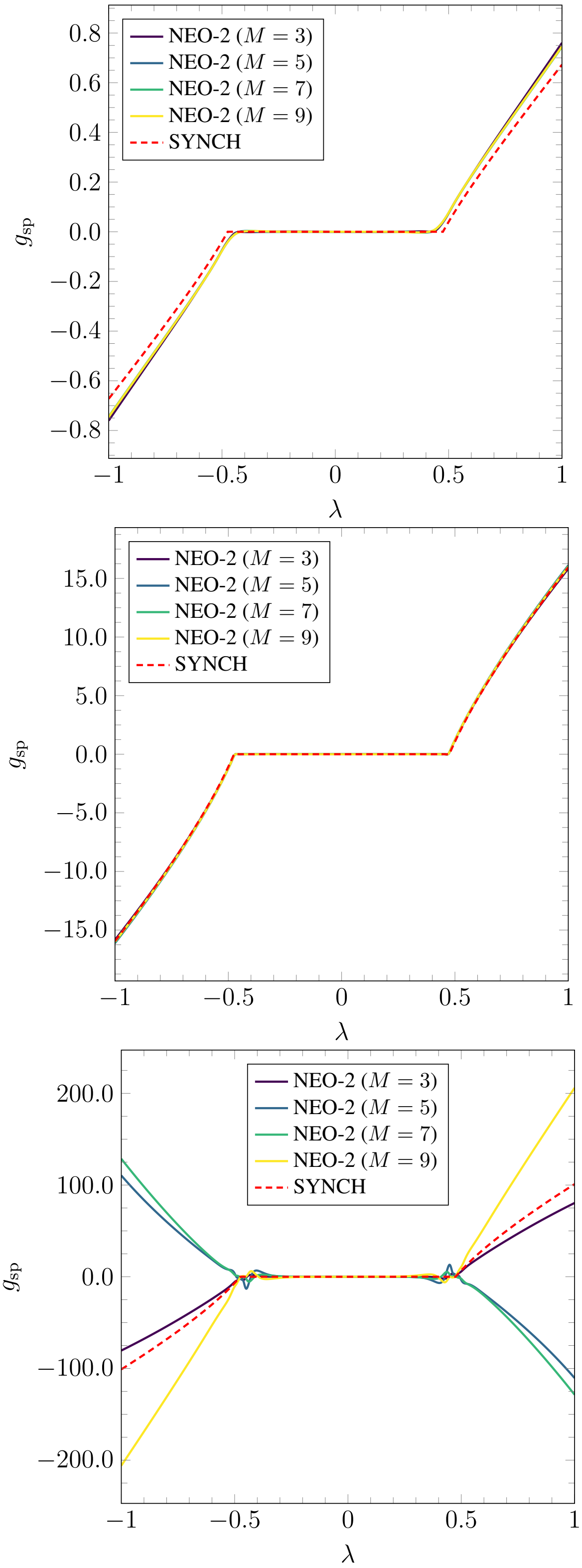

Figure 4.8: Generalized Spitzer function as a function of the pitch angle parameter $\lambda = v_\parallel / v$ at the field minimum of the model tokamak for particles at velocities $x = 1$, $x = 3$, and $x = 5$ (from top to bottom). The NEO-2 results (solid lines) have been computed with Sonine polynomials. Results in the collisionless limit from SYNCH (dashed lines) are shown for comparison.

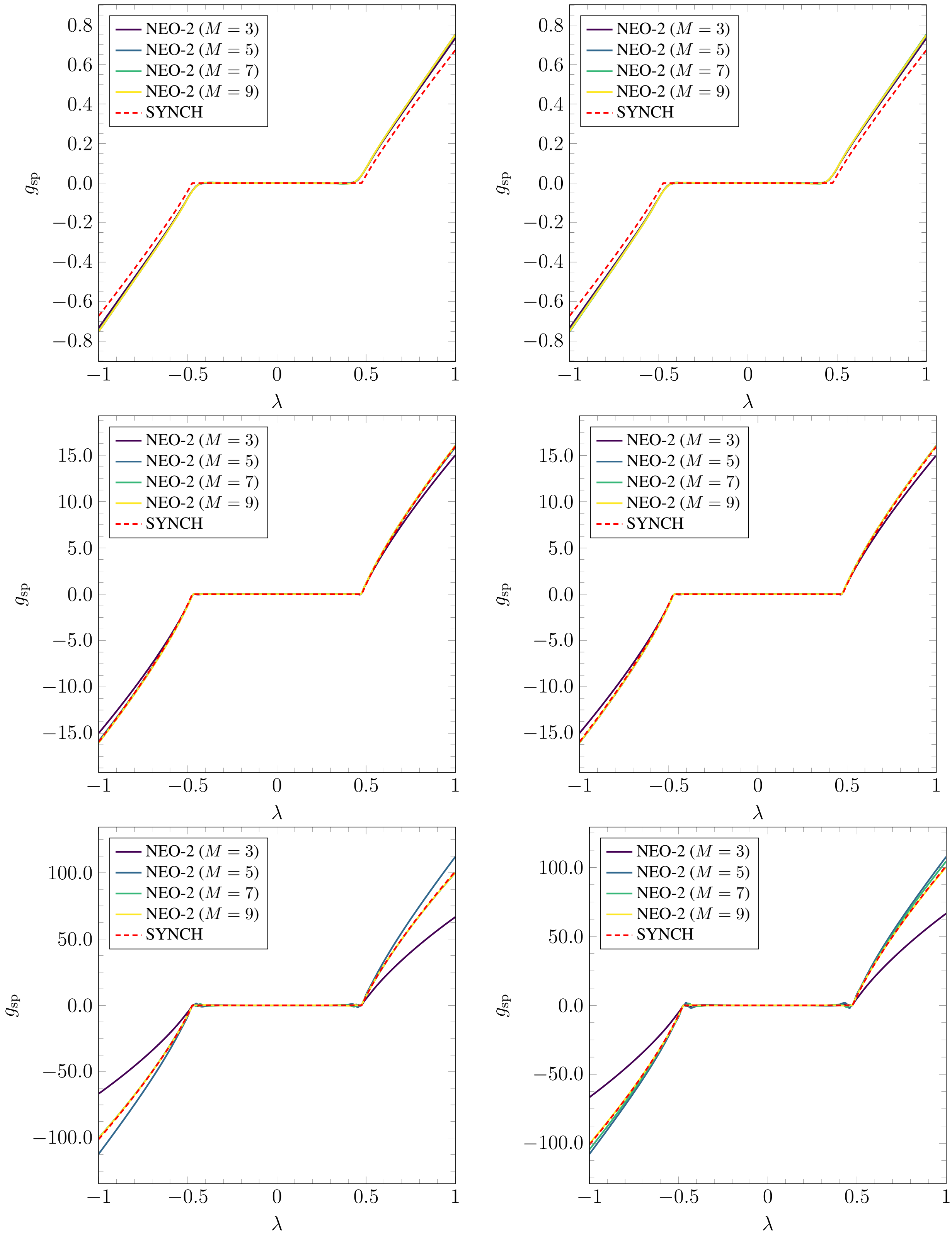

Figure 4.9: Same as in Figure 4.8 but computed with cubic B-splines defined in the domain $0 \leqslant x \leqslant 4$ (left) and defined in domain $0 \leqslant x \leqslant 5$ (right) with subsequent Taylor expansion for both.

4.2.3 High-collisionality limit

In the high-collisionality limit, as well as in homogenous magnetic fields, the generalized Spitzer function is connected to the classical Spitzer function by the following linear relation,

$$g(\mathbf{r}, x) = b(\mathbf{r})\lambda D(x), \tag{4.2}$$

where $b(\mathbf{r}) = B(\mathbf{r})/B_{\mathrm{ref}}$ is a normalized magnetic field module, $\lambda = v_{\|}/v$ is the pitch angle parameter, and $D(x)$ is the classical Spitzer function as given in tabulated form in Table I of Ref. 13. For plotting a continuous function the given discrete values for $D(x)$ have been interpolated using a piecewise cubic spline. In Figure 4.10 various results of NEO-2 computed close to the magnetic axis, where the magnetic field is almost homogenous along the field line, for collisionality $L_c/l_c = 10$ are compared to the classical Spitzer function. For mild particle velocities the results match perfectly the analytical solution, where the mismatch at higher velocities is a result of leaving the high-collisionality limit where the classical Spitzer function is valid. Figure 4.11 confirms the linear dependence of the Spitzer function on the pitch angle parameter. As can be seen, for thermal velocity Laguerre polynomials as well as B-splines perfectly match the classical Spitzer function independent of the tested number of basis functions. As shown in Ref. 5, the high-collisionality limit usually overestimates the current drive efficiency.

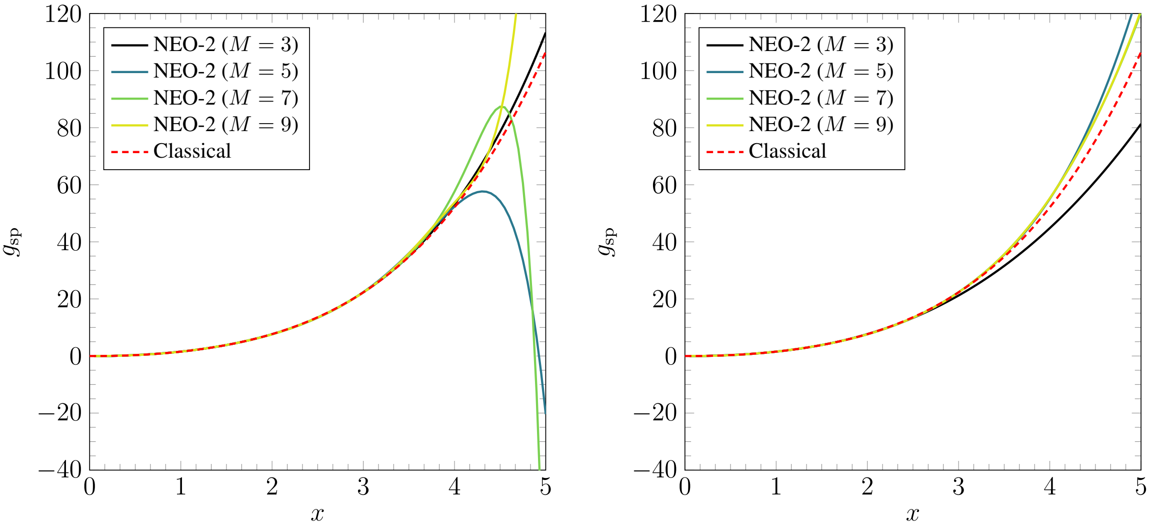

Figure 4.10: Convergence of the NEO-2 solution (solid lines) for the generalized Spitzer function with respect to the number of Sonine polynomials (left) and the number of cubic B-splines (right) as a function of the normalized velocity $x = v/v_T$ at pitch angle $\lambda = 1$ for the model tokamak. In addition, the classical Spitzer function (dashed line) is shown for comparison.

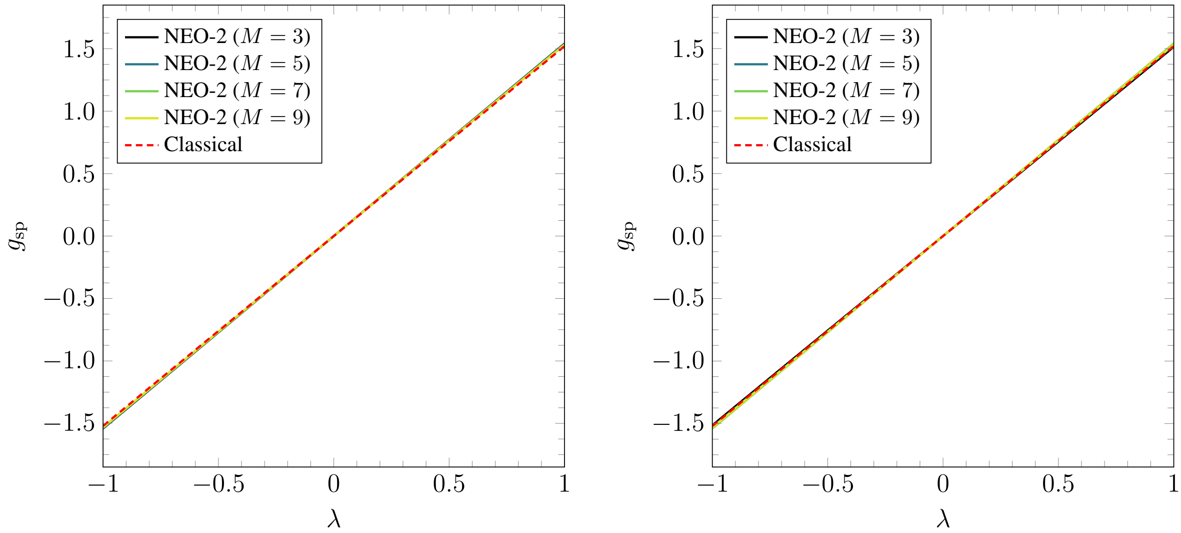

Figure 4.11: Generalized Spitzer function vs. pitch angle computed close to the magnetic axis with NEO-2 (solid lines) where the solution is expanded in terms of Sonine polynomials (left) and cubic B-splines (right) for particles with thermal velocity. The classical Spitzer is shown for comparison (dashed line).

4.2.4 Finite collisionality

In Figure 4.12 the distribution of the magnetic field module on the flux surface of a model tokamak with concentric circular flux surfaces as well as of a standard configuration of Wendelstein 7-X at half radius ($s = 0.25$ where s is the normalized toroidal flux) is presented. Observation points for the computation of the generalized Spitzer function are depicted as colored points. In Figure 4.13 the NEO-2 results for the generalized Spitzer function in a tokamak is shown together with its derivative with respect to the perpendicular velocity for a collisionality $L_c/l_c = 10^{-3}$. For the results presented within this section, cubic B-splines are used as basis functions. Results in the long mean free path limit are again modeled with SYNCH.

The colors of the curves correspond to the different observation points as depicted by respective marker colors in Figure 4.12. As can be seen the generalized Spitzer function is strictly antisymmetric at the absolute field maximum and field minimum, while for the points in between a significant symmetric part of the function is observed. This is explained by a combination of the magnetic mirroring force and collisional detrapping effects due to finite collisionality. This symmetric part is responsible for current drive by waves with symmetric spectra [17] as being discussed in Chapter 5. For higher velocities this part becomes smaller and is more localized in the boundary layer separating trapped and passing particles what is clearly seen in the derivatives of the generalized Spitzer function. Such a derivative with respect to the perpendicular velocity is of main interest for ECCD simulations (see Equation (2.79)). It should be noted that for the tokamak two observation points are at the absolute field minimum, while they are at different toroidal angles. Therefore, the generalized Spitzer function of these two observation points lie on top of each other in the pertinent plots because of the axisymmetric geometry. In Figure 4.14, where the same plots are shown for a standard configuration of Wendelstein 7-X, this is not longer the case. Here, the behavior of the generalized Spitzer function is similar to the investigated tokamak configuration, however, at local extrema of the magnetic field also a symmetric part of the function is observed.

More detailed studies of the impact of finite collisionality on the generalized Spitzer function are presented in Ref. 18 for tokamaks and in Ref. 7 for stellarators.

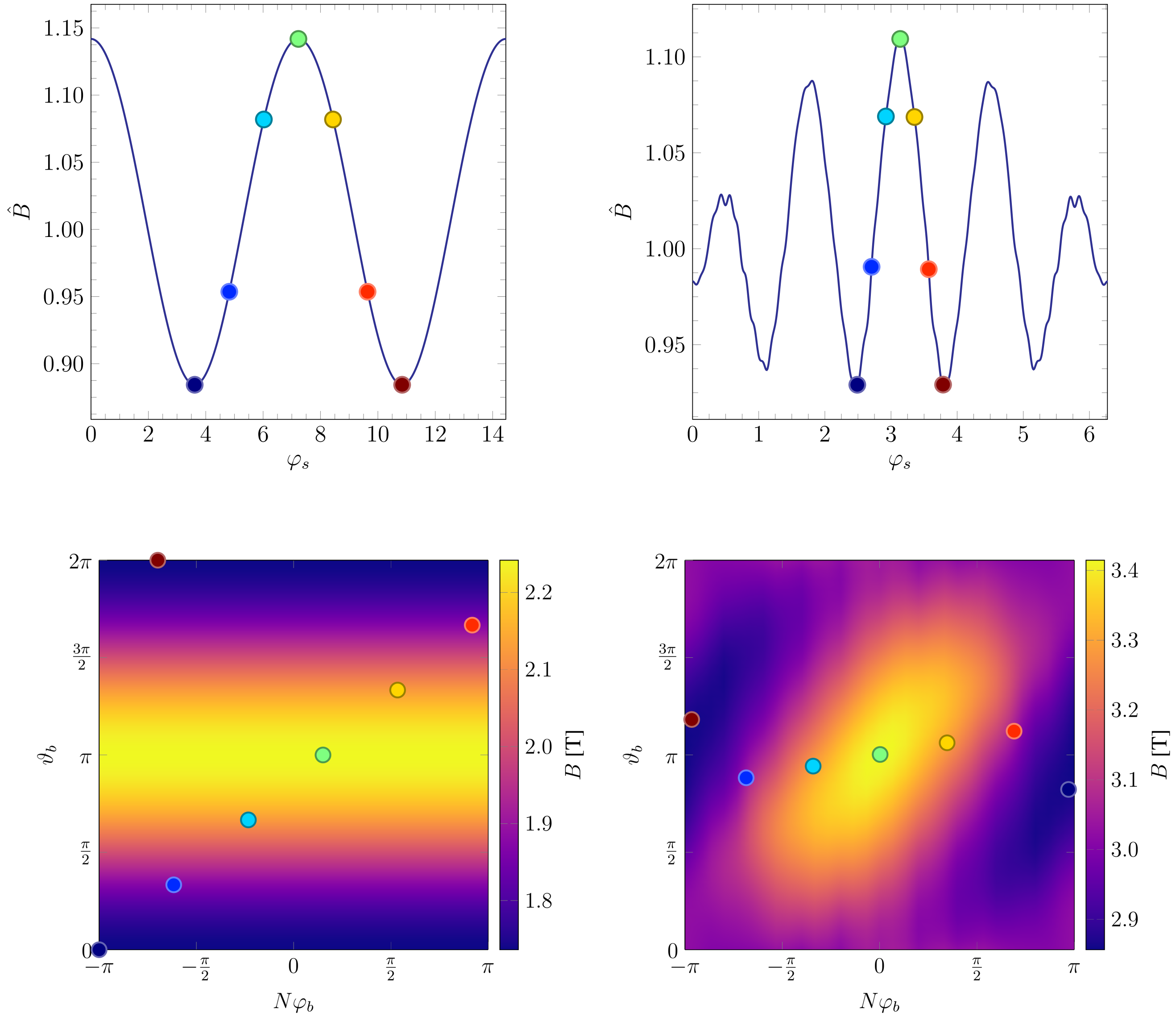

Figure 4.12: Upper plot - Normalized magnetic field module in a model tokamak (left) and in a standard configuration of Wendelstein 7-X (right) as a function of the distance along the field line φ_s on flux surface $s = 0.25$ (half radius). Lower plot - Distribution of the magnetic field module on flux surface $s = 0.25$ for the same devices as a function of the toroidal (φ_b) and poloidal (ϑ_b), angle. Colored points depict various spatial observation points of interest. N is the number of toroidal field periods which is 1 for the tokamak and 5 for Wendelstein 7-X.

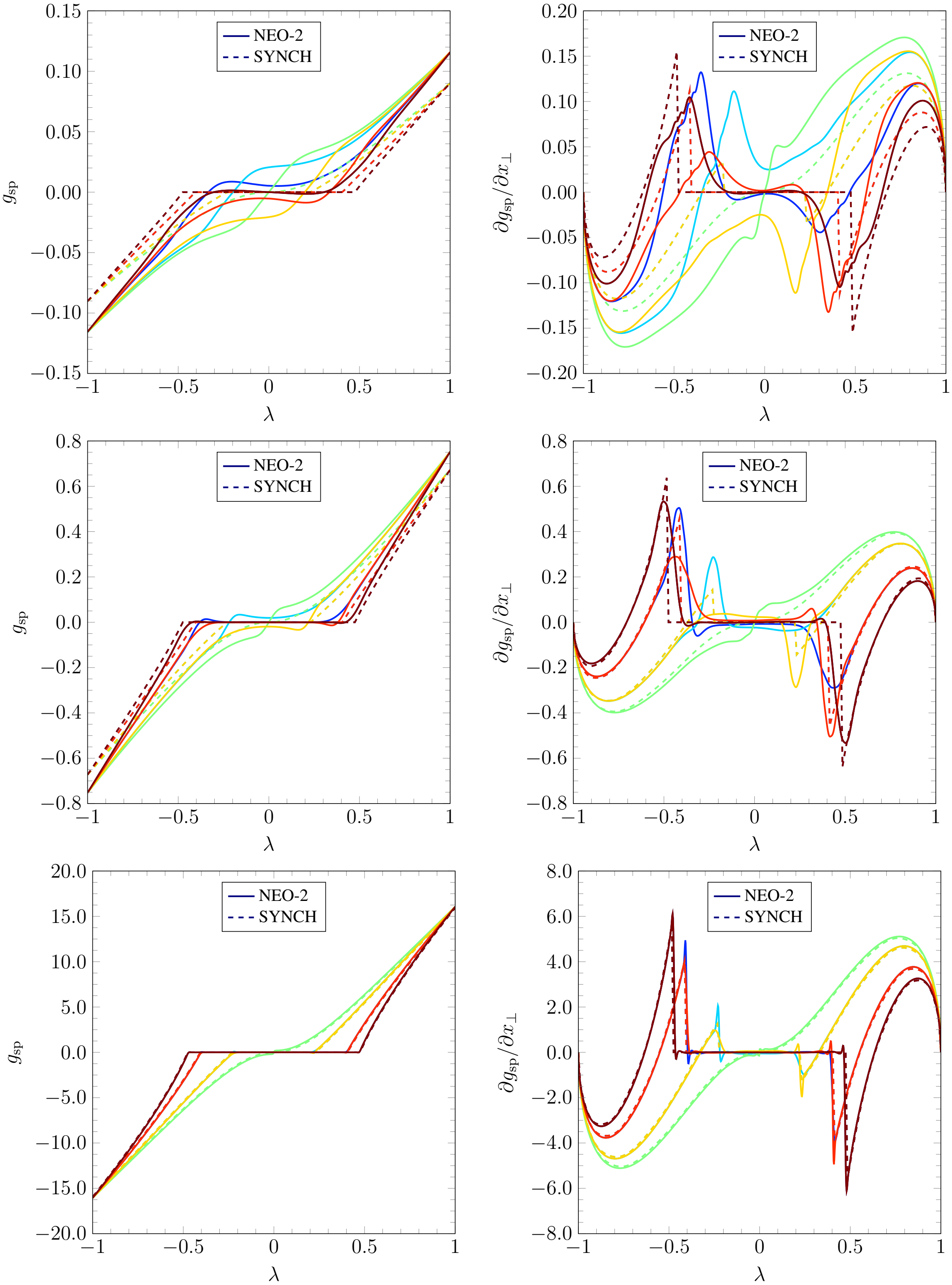

Figure 4.13: Generalized Spitzer function (left) and its derivative with respect to the perpendicular velocity (right) in a model tokamak as a function of the pitch angle parameter for fixed particle velocities ($x = 0.5$, $x = 1.0$, and $x = 3.0$ from top to bottom) at various observation points as depicted as colored dots in Figure 4.12. Curves from NEO-2 and SYNCH are depicted as solid and dashed lines, respectively.

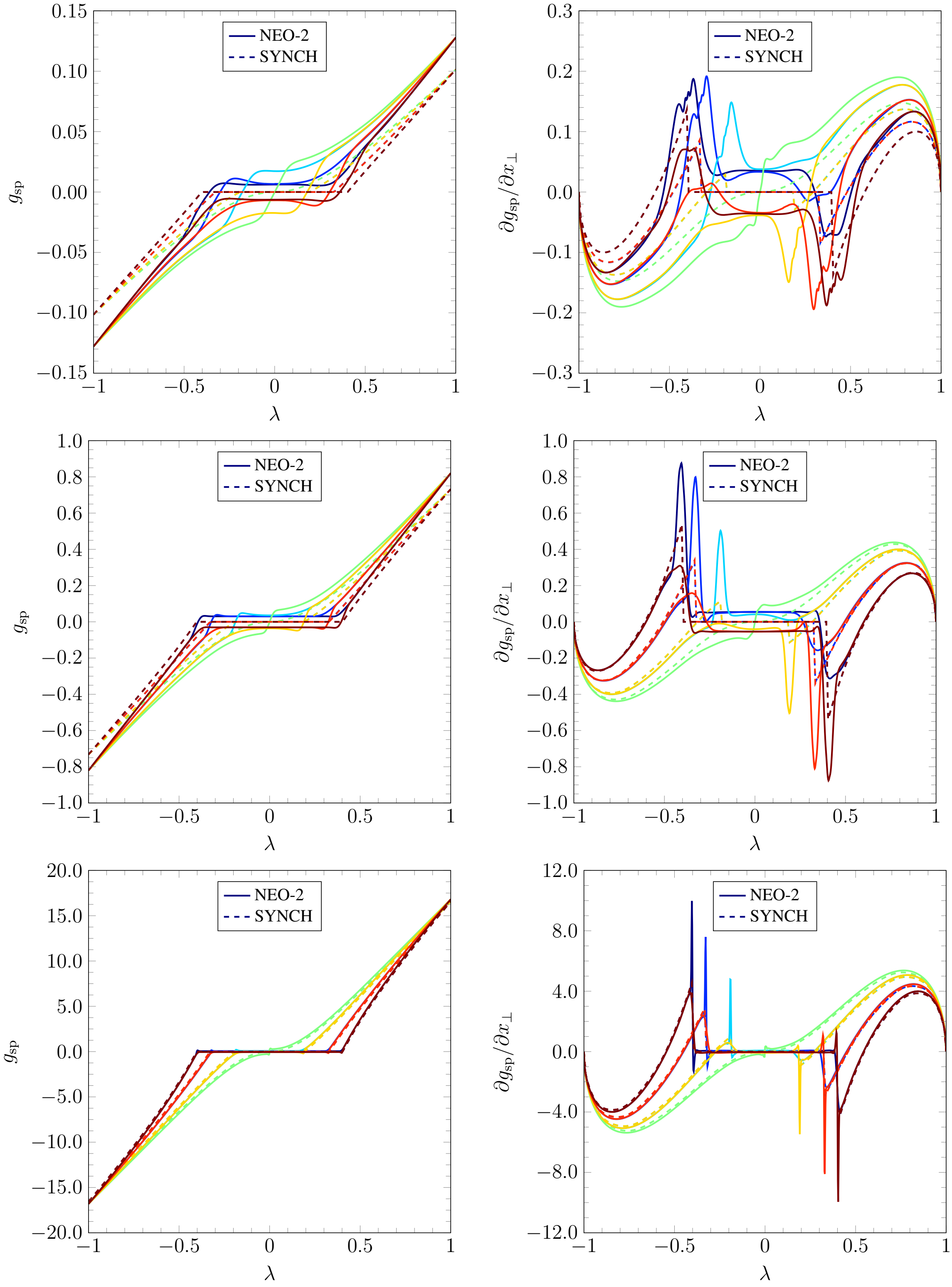

Figure 4.14: Generalized Spitzer function (left) and its derivative with respect to the perpendicular velocity (right) in a standard configuration of Wendelstein 7-X as a function of the pitch angle parameter for fixed particle velocities ($x = 0.5$, $x = 1.0$, and $x = 3.0$ from top to bottom) at various observation points as depicted as colored dots in Figure 4.12. Curves from NEO-2 and SYNCH are depicted as solid and dashed lines, respectively.

4.3 Benchmarking with relativistic collision operator

As discussed in Section 2.4, in the course of this thesis NEO-2 has been upgraded to support three different collision models, namely the non-relativistic collision operator from Trubnikov et al. [28] and Rosenbluth et al. [43], the fully relativistic collision operator from Braams and Karney [19], as well as the fully relativistic collision operator obtained by direct evaluation of Beliaev and Budker [20] including high order Legendre harmonics. In the following, results from these models are benchmarked against the code SYNCH. For benchmarks in the non-relativistic limit the temperature in the relativistic models has been set to $T = 1\,\mathrm{eV}$. The settings for NEO-2 remain the same as before: Collisionality parameter $L_c/l_c = 10^{-3}$ and the effective charge is $Z_{\mathrm{eff}} = 1$. The collisionality parameter depends on temperature and density, however for benchmarking purposes the collisionality is fixed to this value independent of the particle temperature. According to the definition of the mean free path (2.144) this corresponds to an increase of the particle density with increasing temperature. The generalized Spitzer function is computed for a model tokamak and a high-mirror configuration of Wendelstein 7-X at half radius ($s = 0.25$). This corresponds to an aspect ratio $A = 7.87$ for the tokamak and $A = 21.38$ for Wendelstein 7-X.

In Figures 4.15 and 4.16 the generalized Spitzer function computed in the non-relativistic limit as a function of the dimensionless momentum module $x = u/v_T$ for fixed pitch angle parameter is presented for a tokamak and Wendelstein 7-X, respectively. All three collision models supported by the upgraded version of NEO-2 agree well with each other as well as with the results from the collisionless limit as computed by SYNCH. The comparison of the generalized Spitzer function computed with $L = 1$ and $L = 3$, where $L + 1$ denotes the number of Legendre harmonics used in the collision operator, confirms the statement that higher order Legendre harmonics do not influence the result significantly. For high temperatures, $T = 50\,\mathrm{keV}$ and $T = 100\,\mathrm{keV}$, respectively, the same benchmark is presented in Figure 4.17 for a tokamak and in Figure 4.18 for Wendelstein 7-X, where in both cases the non-relativistic model is omitted. A good match of the different collision models is observed.

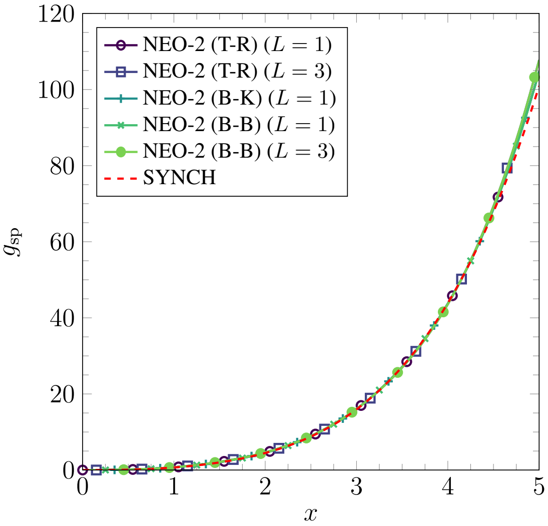

Figure 4.15: Generalized Spitzer function as a function of the dimensionless momentum module x for a model tokamak for particles at the global minimum point with pitch angle parameter $\lambda = v_{\|}/v = 1$ and plasma collisionality $L_c/l_c = 10^{-3}$ in the non-relativistic limit ($T = 1\,\mathrm{eV}$) computed by NEO-2 (solid lines) using the collision operator based on Trubnikov and Rosenbluth (T-R), Braams and Karney (B-K), and direct evaluation of Beliaev and Budker (B-B), respectively, and computed by SYNCH (dashed line).

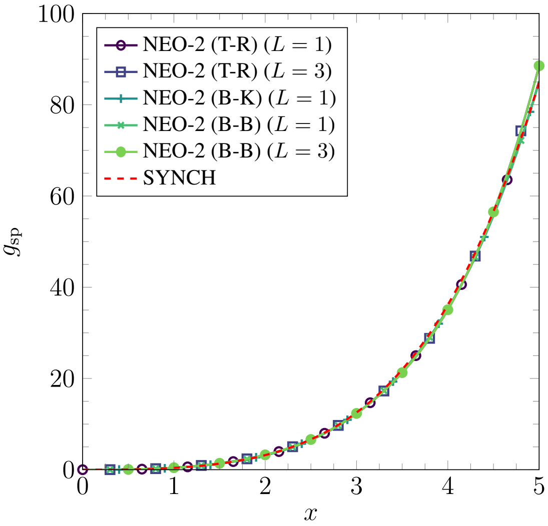

Figure 4.16: Generalized Spitzer function as a function of the dimensionless momentum module x for a high-mirror configuration of Wendelstein 7-X for particles at the global minimum point with pitch angle parameter $\lambda = v_{\|}/v = 1$ and plasma collisionality $L_c/l_c = 10^{-3}$ in the non-relativistic limit ($T = 1\,\mathrm{eV}$) computed by NEO-2 (solid lines) using the collision operator based on Trubnikov and Rosenbluth (T-R), Braams and Karney (B-K), and direct evaluation of Beliaev and Budker (B-B), respectively, and computed by SYNCH (dashed line).

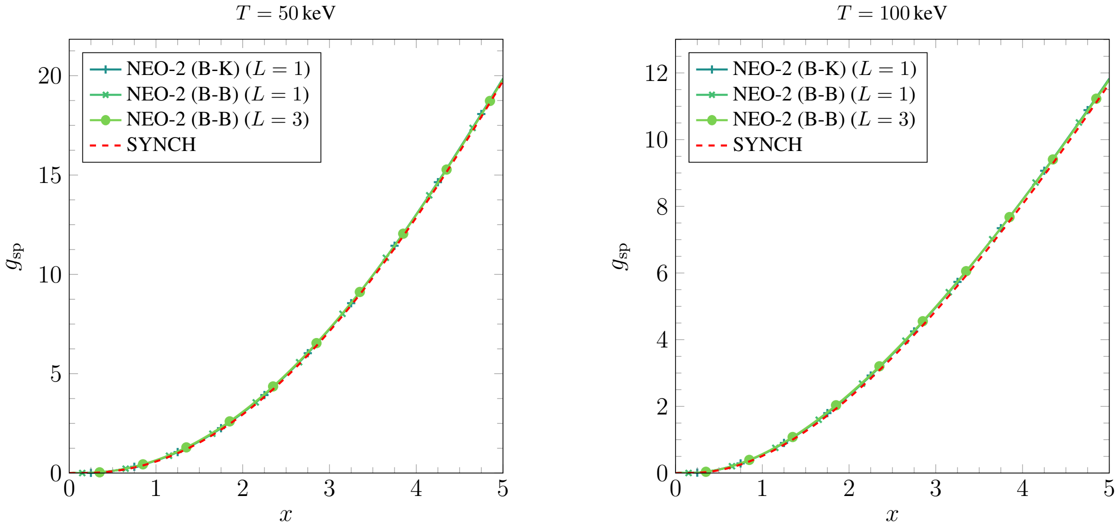

Figure 4.17: Generalized Spitzer function as a function of the dimensionless momentum module x computed for a model tokamak with circular flux surfaces for particles at the global minimum point with temperatures $T = 50\,\mathrm{keV}$ (left) and $T = 100\,\mathrm{keV}$, both with the same plasma collisionality $L_c/l_c = 10^{-3}$, and a pitch angle parameter $\lambda = x_{\|}/x = 1$ using the relativistic collision operators (solid lines) based on Braams and Karney (B-K), and based on direct evaluation of Beliaev and Budker (B-B), respectively. As a benchmark the result of the fully relativistic solver SYNCH (dashed line) is plotted.

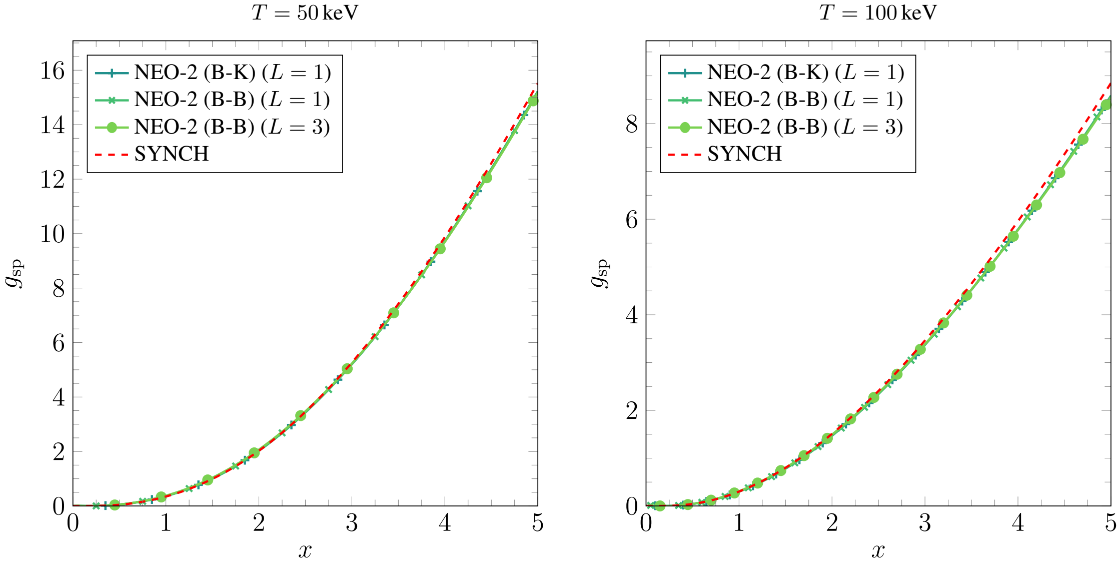

Figure 4.18: The same as in Figure 4.17 but for a high-mirror configuration of Wendelstein 7-X.

In Figures 4.19 and 4.20 the generalized Spitzer function computed with the fully relativistic collision model obtained by direct evaluation of Beliaev and Budker is plotted for various temperatures. Accordingly, in Figures 4.21 and 4.22 the generalized Spitzer function is plotted as a function of the pitch angle parameter λ for various temperatures for particles with $x = 1$ (left) and $x = 3$ (right). As expected, the results from NEO-2 accounting for finite plasma collisionality converge to the results obtained in the collisionless limit for higher particle velocities (see right plots of Figures 4.21 and 4.22).

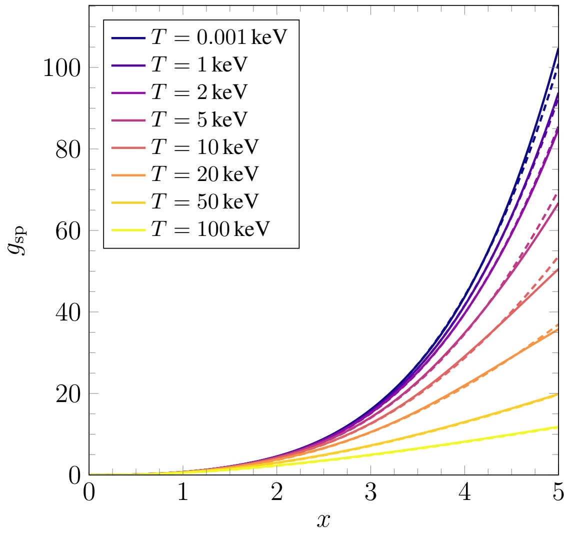

Figure 4.19: Generalized Spitzer function as a function of the dimensionless momentum module x computed for a model tokamak with circular flux surfaces at the global minimum point at various temperatures, however with same plasma collisionality $L_c/l_c = 10^{-3}$, with pitch angle parameter $\lambda = x_{\|}/x = 1$ using the fully relativistic collision operator in NEO-2 obtained by direct evaluation of Beliaev and Budker (solid). As a benchmark the results in the collisionless limit of the fully relativistic code SYNCH (dashed) are given.

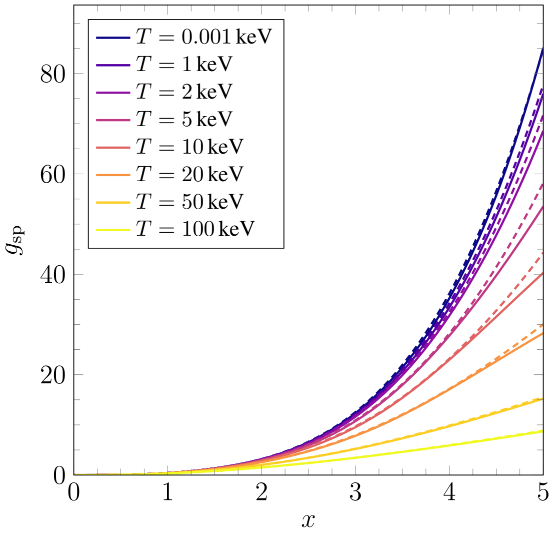

Figure 4.20: The same as in Figure 4.19 but for a high-mirror configuration of Wendelstein 7-X.

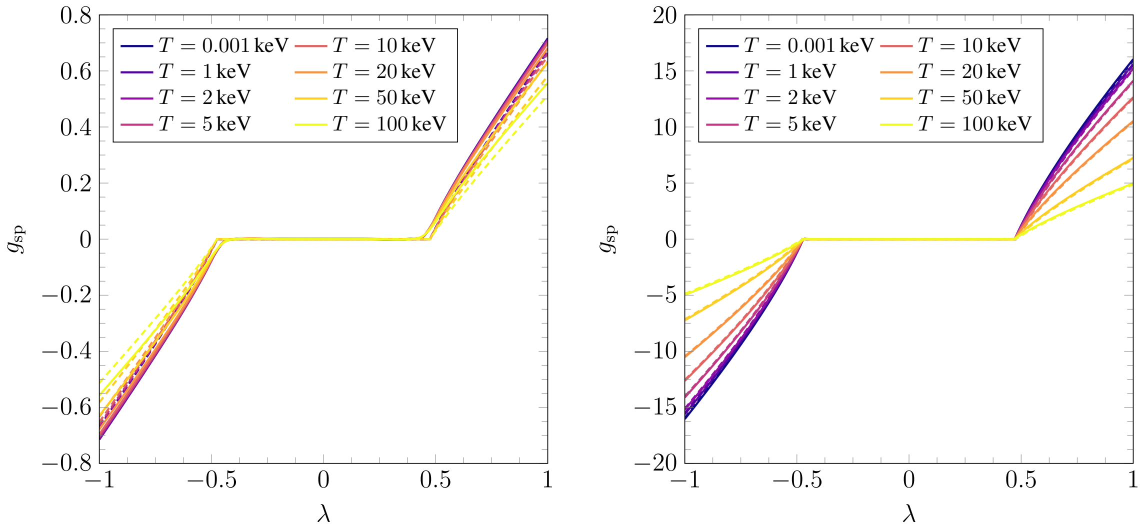

Figure 4.21: Generalized Spitzer function for various temperatures and same plasma collisionality $L_c/l_c = 10^{-3}$ computed with NEO-2 (solid) and SYNCH (dashed) at the global minimum point of a model tokamak with circular flux surfaces for particles with $x = 1$ (left) and $x = 3$ (right).

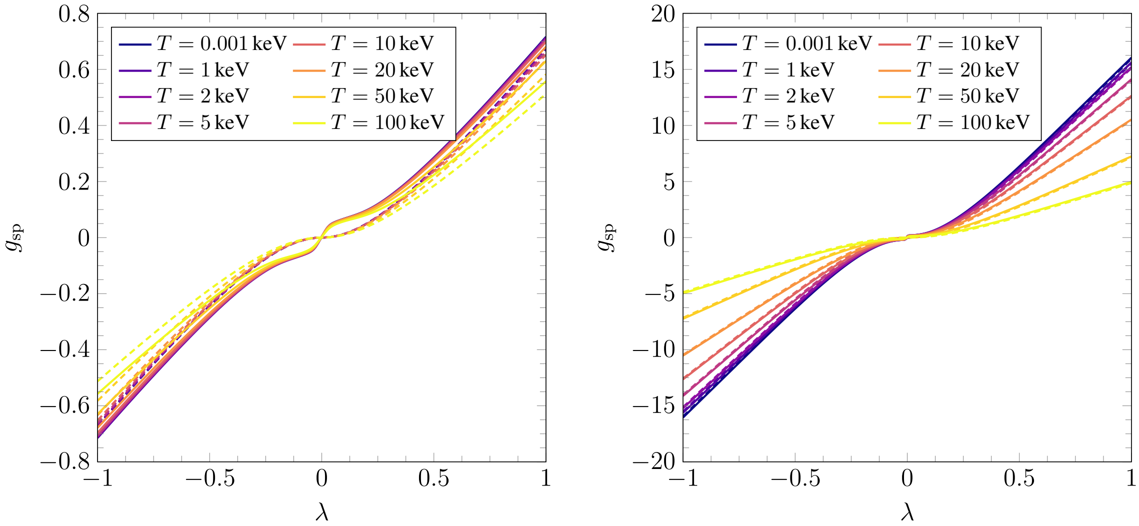

Figure 4.22: The same as in Figure 4.21 but at the global maximum point.

Chapter 5

Electron cyclotron current drive simulations for finite collisionality plasmas in Wendelstein 7-X using the full linearized collision model

While in Chapter 4 the upgraded version of NEO-2 has been benchmarked against asymptotical collisionality limits, in this chapter results of this code are used as an input to the ray-tracing code TRAVIS for investigation of the impact of finite collisionality effects on the electron cyclotron current drive efficiency. The contents of this chapter have been published in the following peer-reviewed journal article formulated by the author:

- G. Kapper, S. V. Kasilov, W. Kernbichler, A. F. Martitsch, M. F. Heyn, N. B. Marushchenko, and Y. Turkin, “Electron cyclotron current drive simulations for finite collisionality plasmas in Wendelstein 7-X using the full linearized collision model”, Physics of Plasmas **23**, 112511 (2016)

In this thesis only minor modifications to the content have been made. In addition to the contents of this paper, an estimation of the influence of ECCD on the radial rotational transform profile and preliminary results from a computation using a fully relativistic collision model have been added in this thesis.

Contents of this chapter

5.1 Introduction 99
5.2 Studies of the current drive efficiency 100
5.3 ECCD simulations with a ray-tracing procedure 103
    5.3.1 Low and moderate density scenario - X2-mode 106
    5.3.2 High density scenario - O2-mode 112
    5.3.3 Current drive mechanisms 119
    5.3.4 Influence of ECCD on iota at the plasma edge 119
    5.3.5 Preliminary results with relativistic collision operator 120
5.4 Conclusion 121

5.1 Introduction

In the last decades a lot of effort was made to optimize the confinement properties of stellarator type toroidal plasma confinement devices since they were invented by Lyman Spitzer in the 1950s [54]. Wendelstein 7-X, being in focus of current drive studies in this chapter, is of the HELIAS (helical axis advanced stellarator) type [23] and has been optimized for good MHD (Magnetohydrodynamic) stability, improved neoclassical confinement, improved confinement of fast ions, and a low bootstrap current (see also Ref. 55). Therefore, Wendelstein 7-X is ready to play a key role in proving the concept of the optimized stellarator for future steady state fusion power plants.

The major and effective minor radius of the plasma are $R = 5.5\,\mathrm{m}$ and $r = 0.55\,\mathrm{m}$, respectively. The device consists of $N = 5$ toroidal field periods, where each field period can be separated into two half periods each containing 5 non-planar modular coils of different shapes and 2 additional planar coils. Each coil has their own power supply resulting in great flexibility of the magnetic configuration. Different configurations of Wendelstein 7-X are defined by different currents in the coils within a half period. The standard configuration is determined by identical currents in all modular coils and no additional currents in the planar coils. This is in contrast to low- and high-mirror configurations where these currents are not the same. The magnetic field from currents of the planar coils has no poloidal component and is used for reduction and increase of the rotational transform [24]. A detailed view on the superconducting magnetic coil system and its assembly can be found in Ref. 56. Accurate measurements of the magnetic field after the completion of the coil system have confirmed remarkable small errors in the magnetic assembly [57]. The device went into operation in December 2015, where first experiments with helium plasmas have started, followed by initial and well controllable hydrogen discharges in February 2016 [25]. While the low densities of this first operation phase using a graphite limiter configuration does not allow for investigation of the stellarator optimization properties which appear at sufficient plasma pressure, it has already been reported that low density electron cyclotron resonance heated plasmas exhibit the core-electron-root confinement [58]. In future operation phases the device will be set up for an island divertor configuration, where a low-order rational flux surface is placed at the plasma edge while such rational flux surfaces are avoided in the plasma core by the low-shear concept since large magnetic islands may be formed there. In contrast to the poloidal divertor concept in tokamaks, here a

natural separatrix is formed without the need of additional fields [59]. These special device characteristics can be destroyed by a small bootstrap current which has to be compensated by electron cyclotron current drive (ECCD) [60], where the cyclotron resonant interaction of electrons and incident radio-frequency (RF) waves drives a parallel current [11]. The electron cyclotron resonance heating (ECRH) system of Wendelstein 7-X is designed to employ ten gyrotrons each with a power up to 1 MW at a wave frequency of 140 GHz at continuous operation [61]. This frequency corresponds to the second harmonic of the electron cyclotron frequency at $B = 2.5\,\mathrm{T}$. A detailed study of the influence of the main Fourier modes of the magnetic field on ECCD and bootstrap current using a self-consistent transport simulation can be found in Ref. 24.
The purpose of this chapter is to study the effect of finite collisionality on the total driven current and its influence on the radial iota profile using as an example a high-mirror configuration of Wendelstein 7-X. As described in Chapter 3, the current drive efficiency is calculated by the drift kinetic equation solver NEO-2 [2] in the non-relativistic limit without further simplifications to the collisional model and without any simplification on the device geometry. Within the adjoint approach [21] these results are used in the ray-tracing code TRAVIS [22] together with results from the code SYNCH [12], which solves the current drive problem in the long mean free path limit. This allows to compare the total driven current obtained from different collision models for various launch scenarii. In addition, preliminary results are presented, where a relativistic full linearized Coulomb collision model, as introduced in Section 2.4, has been used.

5.2 Studies of the current drive efficiency

The impact of finite plasma collisionality on ECCD is investigated using plasma parameter profiles from the transport code NTSS [62] and a high-mirror configuration of Wendelstein 7-X computed by the equilibrium code VMEC [63]. The plasma parameters as depicted in Figure 5.1 correspond to a collisionality at the onset of the long mean free path regime, where the collisionality is roughly three times smaller than needed for the plateau regime. Therefore, this profile represents an initial stage of device operation, where finite collisionality effects play a more significant role than at higher temperatures.

Heating by microwaves is mainly performed close to the field maximum where the absorption of the wave energy by passing particles usually dominates the amount

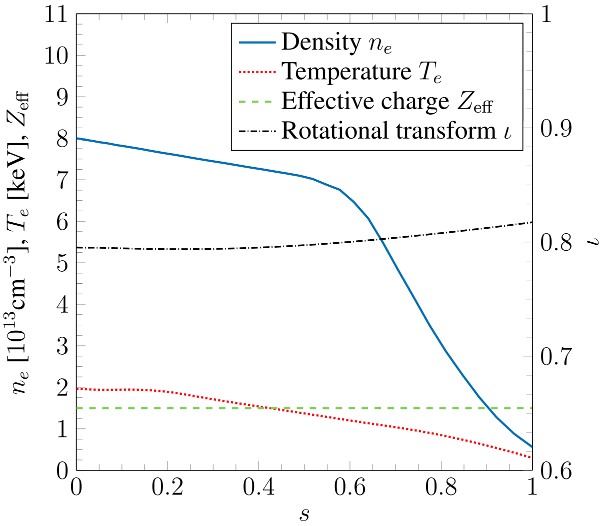

Figure 5.1: Plasma parameter profiles computed by the transport code NTSS [62] and the rotational transform ι as functions of the normalized toroidal flux s. (From G. Kapper, et al. [1])

of energy absorbed by trapped particles. Therefore, the behavior of the generalized Spitzer function at spatial points around the field maximum is of special interest and is investigated in the following. The distribution of the magnetic field module at half radius is given in Figure 5.2, where some spatial points of interest are marked. Results of the generalized Spitzer function from NEO-2 for finite collisionality pertinent to given plasma parameters together with results for the long mean free path regime from the code SYNCH for two different particle velocities, $v = v_T$ and $v = 3v_T$, are presented in Figure 5.3. Here, $v_T = \sqrt{2T_e/m_e}$ is the thermal velocity, where T_e and m_e are electron temperature and electron mass, respectively. Both, the internal TRAVIS model, where the generalized Spitzer function is approximated in the collisionless limit, and the SYNCH model conserve parallel momentum. It has been shown that the high speed limit models can significantly underestimate the current drive efficiency in contrast to collisionless models with parallel momentum conservation [64].

The generalized Spitzer function with finite collisionality effects taken into account is strictly antisymmetric only at the absolute field maximum, and nearly antisymmetric for points in the bean-shaped plane $\varphi_b = 0$ in which the absolute maximum is located. For regions apart from the field maximum in toroidal directions, a significant symmetric part arises in the trapped region which can be explained by a combined effect of mirroring force and trapping/detrapping due to collisions. While finite collisionality

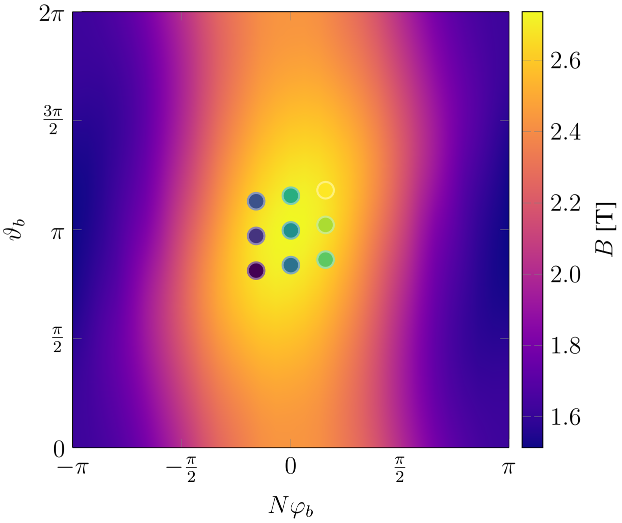

Figure 5.2: Magnetic field module at flux surface $s = 0.25$ as function of Boozer angles ($N = 5$ for Wendelstein 7-X). (From G. Kapper, et al. [1])

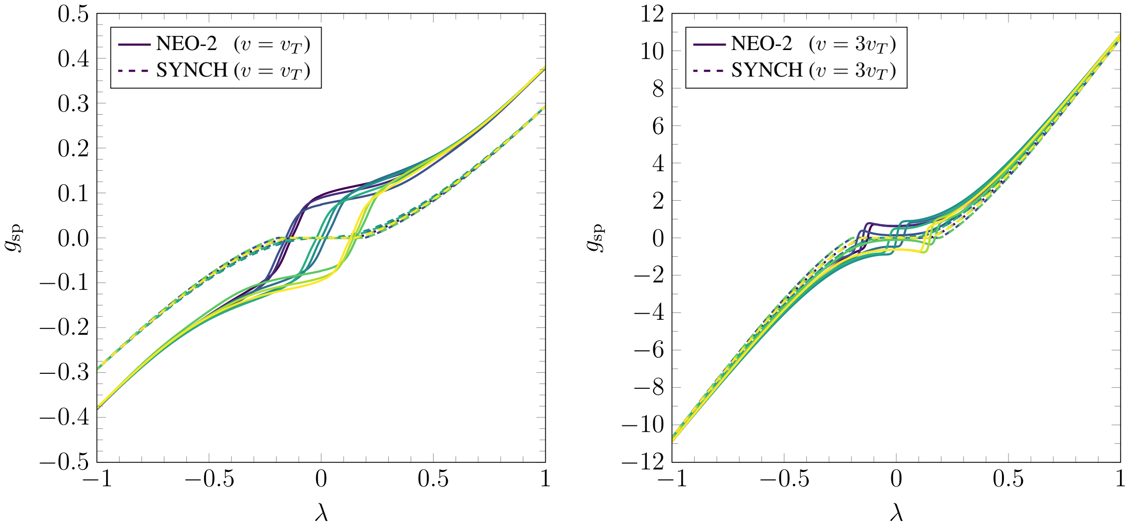

Figure 5.3: Generalized Spitzer function for finite collisionality computed by NEO-2 (solid) and for the collisionless limit computed by SYNCH (dashed) as a function of the pitch parameter $\lambda = v_\parallel/v$. Line colors correspond to respective marker colors in Figure 5.2. (From G. Kapper, et al. [1])

leads mainly to an antisymmetric offset in the passing domain of the distribution function, the symmetric part is also of special interest because it is responsible for current drive by waves with symmetric spectra [17]. These effects become smaller at higher particle velocities where the distribution function converges to the collisionless limit.

In order to further investigate the symmetric part of the generalized Spitzer function, this function is integrated over the pitch parameter in the trapped domain,

$$\overline{g_{\mathrm{sp}}^{(\mathrm{tr})}}(\vartheta, x) = \int\limits_{-\lambda_{\mathrm{tp}}(\vartheta)}^{+\lambda_{\mathrm{tp}}(\vartheta)} \mathrm{d}\lambda g_{\mathrm{sp}}(\vartheta, \lambda(\eta, \sigma), x), \tag{5.1}$$

with

$$\lambda_{\mathrm{tp}}(\vartheta) = \sqrt{1 - \frac{B(\vartheta)}{B_{\max}}}, \tag{5.2}$$

where $B_{\max}$ is the maximum magnetic field module on the flux surface. The distribution of the resulting scalar (5.1) over the angles (this quantity is identical zero in asymptotical limits) is shown in Figure 5.4 for two velocity values, $v = v_T$ and $v = 3v_T$, respectively. This dependence is partly similar to Ref. 15 where the angular distribution of the mono-energetic distribution function for $\lambda = 0$ has been studied.

From Figure 5.3 it is expected that the sign of the mean value of the generalized Spitzer function in the trapped domain is mainly determined by the toroidal angle of Boozer coordinates. However, as seen from Figure 5.4 this is only the case in the vicinity of the absolute field maximum. At toroidal positions apart from the bean-shaped poloidal plane, the sign is determined mainly by the poloidal angle what is similar to the up-down-asymmetry in tokamaks [18]. Summarizing, the non-vanishing mean values of the trapped region of the generalized Spitzer function on almost the whole flux surface indicate significant symmetric parts of this function which would not be seen by collisionless models.

5.3 ECCD simulations with a ray-tracing procedure

In TRAVIS the geometrical optics approach is used for the computation of ECCD, where the quasilinear flux density Γ^i_{RF} of Eq. (2.76) is described in a local approximation,

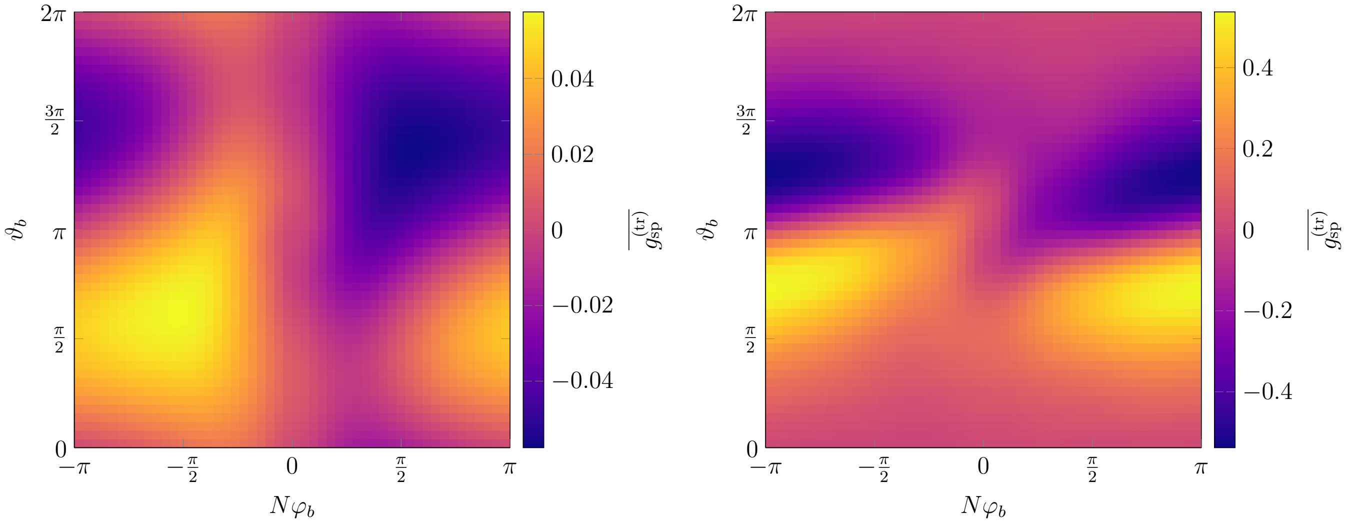

Figure 5.4: Pitch-angle integral in the trapped domain of the generalized Spitzer function (5.1) for velocity values $v = v_T$ (left) and $v = 3v_T$ (right) as functions of Boozer angles on flux surface $s = 0.25$. (From G. Kapper, et al. [1])

i.e., it differs from zero in velocity space only at the resonance line where the (multiple) cyclotron resonance condition taking into account Doppler shift is fulfilled [65],

$$\omega = n\omega_c + k_\parallel v_\parallel. \tag{5.3}$$

Here, ω is the wave frequency, n is the cyclotron harmonic index, $\omega_c = \omega_{c0}/\gamma$ is the relativistic electron cyclotron frequency, $\gamma = (1 - v^2/c^2)^{-1/2}$ is the relativistic factor, and $k_\parallel$ is the parallel wave vector with respect to the magnetic field. In this approach the wave-induced quasilinear diffusion flux density is given as follows,

$$\Gamma^i_{\rm RF} = -\delta(\omega - n\omega_c - k_\parallel v_\parallel) D_0^{ij} \frac{\partial f_{\rm M}}{\partial v^j}, \tag{5.4}$$

where D_0^{ij} are quasilinear diffusion coefficients. Then, Eq. (2.79) takes the form

$$\langle j_{e\parallel} B \rangle = \left\langle \int\limits_{-\infty}^{+\infty} {\rm d}v_\parallel \int\limits_0^{+\infty} {\rm d}v_\perp \delta(\omega - n\omega_c - k_\parallel v_\parallel) F(\vartheta, v_\perp, v_\parallel) \right\rangle. \tag{5.5}$$

The kernel is of the form

$$F(\vartheta, v_\perp, v_\parallel) \propto v_\perp \frac{\partial g^\dagger_{\rm sp}}{\partial v^i} D_0^{ij} \frac{\partial f_{\rm M}}{\partial v^j}, \tag{5.6}$$

where a constant positive factor has been omitted. This kernel is integrated along the resonance line defined by the delta-function to obtain the driven current density. It should be noted that on the $(v_\perp, v_\parallel)$-plane the resonance lines are lines of constant parallel velocity in the non-relativistic case, circles in the weakly-relativistic approach, and elliptic curves in the fully relativistic approach whose centers are located at the $v_\perp = 0$ axis, respectively.

Here, the studies of Ref. 15, where the DKES code [66] has been used for the computation of the ECCD efficiency with a simplified collision model for small but finite collisionalities, are extended. In contrast, NEO-2 is used here for the computation of the generalized Spitzer function without simplifications of the device geometry or of the collision operator. In order to investigate finite collisionality effects on a broad range of launch angles, scans over the poloidal launch angle α (angle between the horizontal plane and the beam) and the toroidal launch angle β (angle between the beam and the meridian plane containing the launcher) are presented in the following for the main scenarii [67], namely the X2- and the O2-resonance. The second harmonic extraordinary mode (X2) with oblique propagation, sufficient for significant ECCD, is usually characterized by almost total absorption before the beam reaches the position of cold resonance $\omega = n\omega_{c0}$, while the second harmonic ordinary mode (O2) has overall lower absorption (typically 50% to 80% for the first pass). However, weak absorption of the O2-mode allows deeper penetration into the plasma and therefore, a significant amount of power absorption by trapped particles. It is necessary to clarify that the investigated launch angles are of theoretical interest and capabilities of the mirrors and other device constraints were not taken into account. As a test configuration one beam with $P_{\text{inp}} = 1$ MW input power and a frequency of 140 Ghz is launched off axis ($Z = -0.1$ m), from an origin given in cylindrical coordinates of $R = 6.56$ m and $\varphi = -6.5$ deg. This position is close to the bean-shaped plane.

5.3.1 Low and moderate density scenario - X2-mode

The common Wendelstein 7-X scenario for low and moderate plasma densities ($n_e < 1.2 \cdot 10^{14}$ cm^{-3} for 140 GHz and 2.5 T) for heating and current drive is the X2-scenario. The restriction on moderate densities originates from the plasma wave cut-off. As seen from the total power absorption in Figure 5.5 (upper plane) for various launch angles, the X2-mode is characterized by total absorption for launch angles where the resonance condition can be fulfilled. In Figure 5.5 (lower plane) the total parallel current driven by passing and trapped particles is depicted. The sign of this current is mainly determined by the parallel wave number $k_\|$, thus strongly depends on the toroidal launch angle. Two particular launch angles are investigated in more detail, namely ($\alpha = 5$ deg, $\beta = 20$ deg) and ($\alpha = 18.75$ deg, $\beta = -2.5$ deg), which are in the following referred to as X2a and X2b, respectively.

Scenario X2a

Scenario X2a is characterized by total absorption of the wave energy by strongly passing particles before the beam reaches the position of cold resonance, see Figure 5.6. This is due to the high optical thickness of the plasma for the X2-mode. However, compared to the collisionless model, a visible increase of the current due to an offset to the antisymmetric part of the generalized Spitzer function is observed (see also Ref. 15). In Figure 5.7 the integral kernel (5.6) of the generated current density is plotted in the $(v_\perp, v_\|)$-plane for the finite collisionality and for the collisionless model with three resonance lines corresponding to positions along the central ray path shown in Figure 5.6. In this qualitative dependence, in contrast to Figure 5.6, beam attenuation along its path caused by the absorption is ignored in F, where the wave amplitude has been set constant everywhere for simplicity. It should be noted that the integral kernel F also depends on the spatial position, therefore it is different for different resonance positions, however, the change is minimal within the three depicted resonance positions and not of relevance for this qualitative view. As can be seen from Figures 5.6 and 5.7, the strong absorption of the X2-mode does not allow any power absorption by trapped particles. This is usually expected for X2-scenarii. In Figure 5.8 (left), where the total driven current within the volume enclosed by a given flux surface is plotted, it can be seen that the collisionless model underestimates the total current by approximately 10%. An estimation of the influence of this current

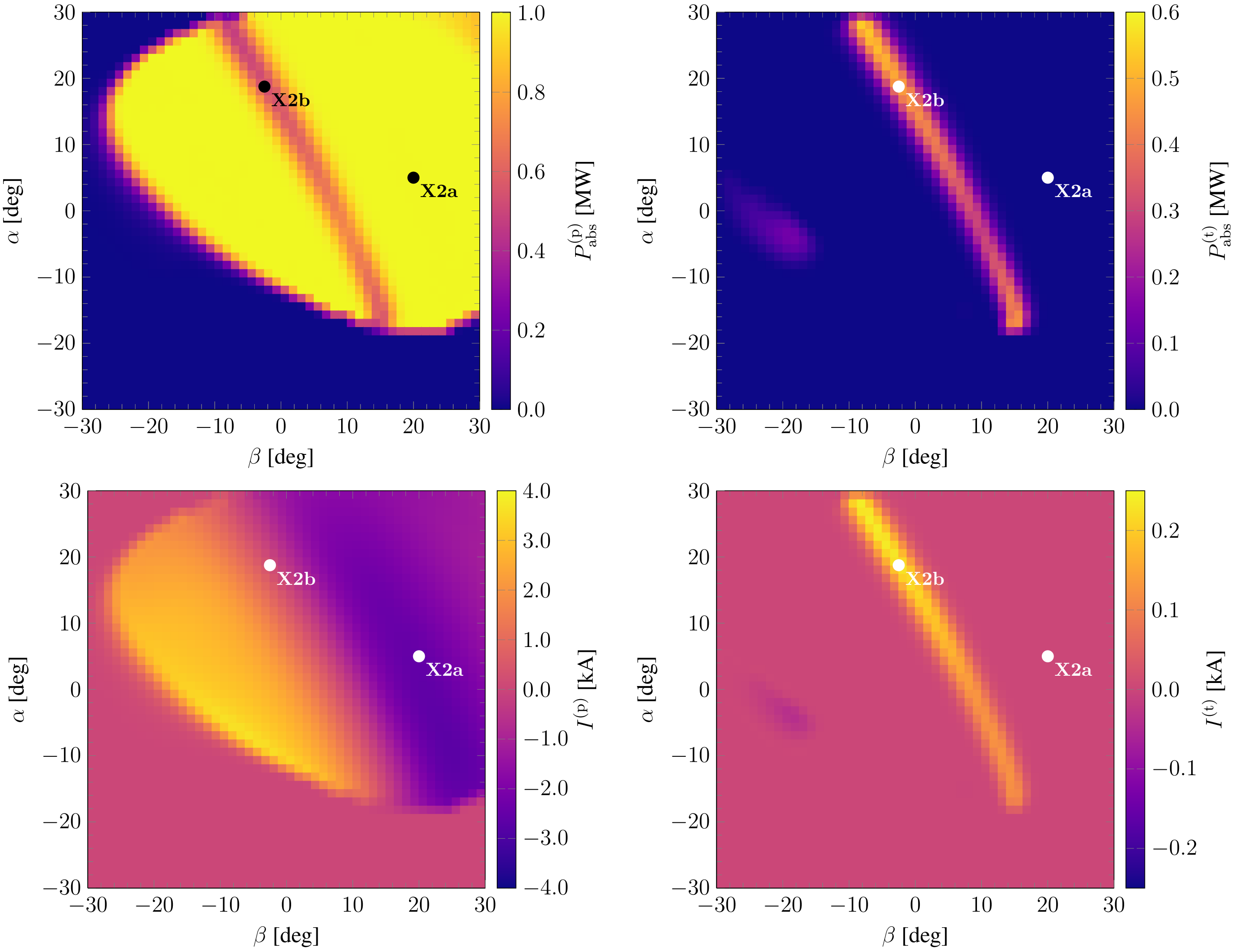

Figure 5.5: X2-mode - Total absorbed power (upper plane) and total driven current (lower plane) of a beam with 1 MW input power as functions of the toroidal (β) and poloidal (α) launch angle by passing particles (left) and trapped particles (right). Two particular launch angles, depicted as X2a and X2b, are then studied in more detail. (From G. Kapper, et al. [1])

on the radial rotational transform profile is given in Figure 5.8 (right). As expected from the current profile, at the absorption region the change of iota as computed using the finite collisionality model is stronger than computed with the collisionless model, while the results of both models significantly deviate from the equilibrium value of iota. However, at the plasma edge there is no visible difference between the two collision models, what is being discussed in more detail in Section 5.3.4. It should be noted that in these plots $\sqrt{s}$ has been used for the abscissa in order to give a better impression of the current and rotational transform profile in real space.

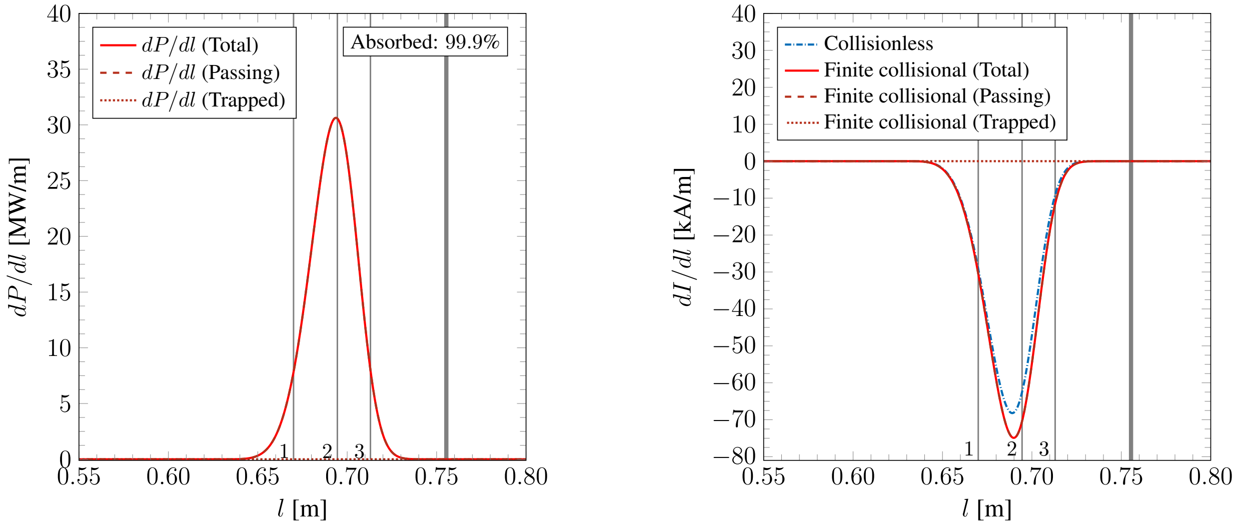

Figure 5.6: Scenario X2a - Locally absorbed power dP/dl (left) and locally driven current dI/dl (right) for the finite collisionality and the collisionless case as functions of the distance along the central ray l. Contributions of passing and trapped particles are depicted as dashed and dotted lines, respectively. The cold resonance position is marked with a thick vertical line. (From G. Kapper, et al. [1])

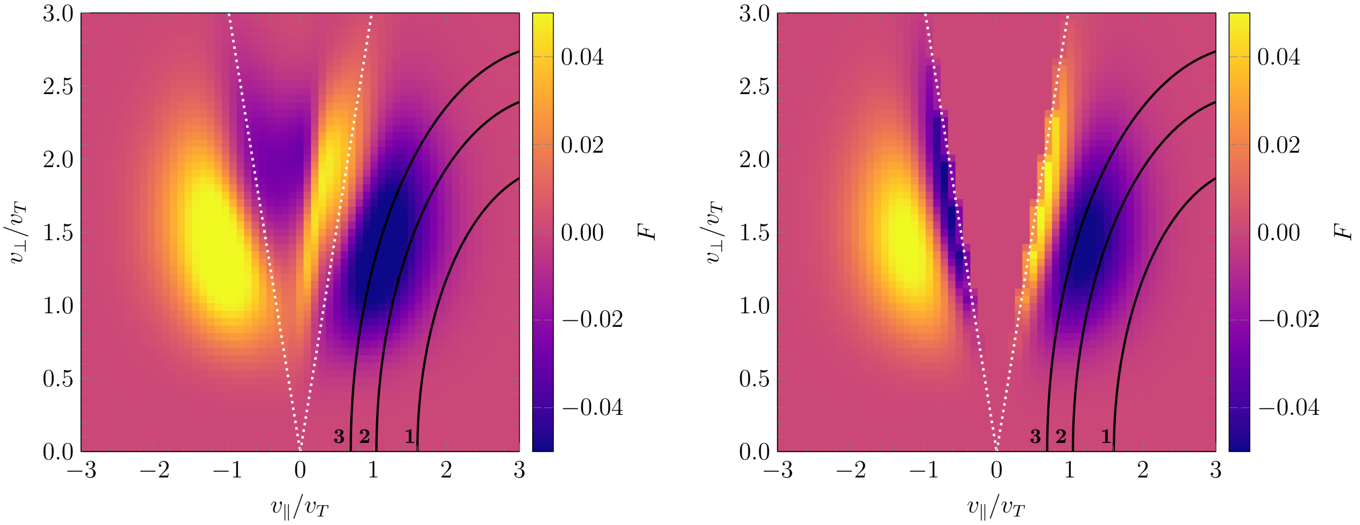

Figure 5.7: Scenario X2a - Current density integral kernel (5.6) as a function of the parallel and perpendicular normalized velocities for finite collisionality (left) and for the collisionless limit (right). The three numbered resonance lines correspond to respective positions indicated by numbered vertical lines in Figure 5.6. The trapped-passing boundary is shown by dashed lines. Colors are supersaturated in order to clarify the different signs of kernel F in different regions. (From G. Kapper, et al. [1])

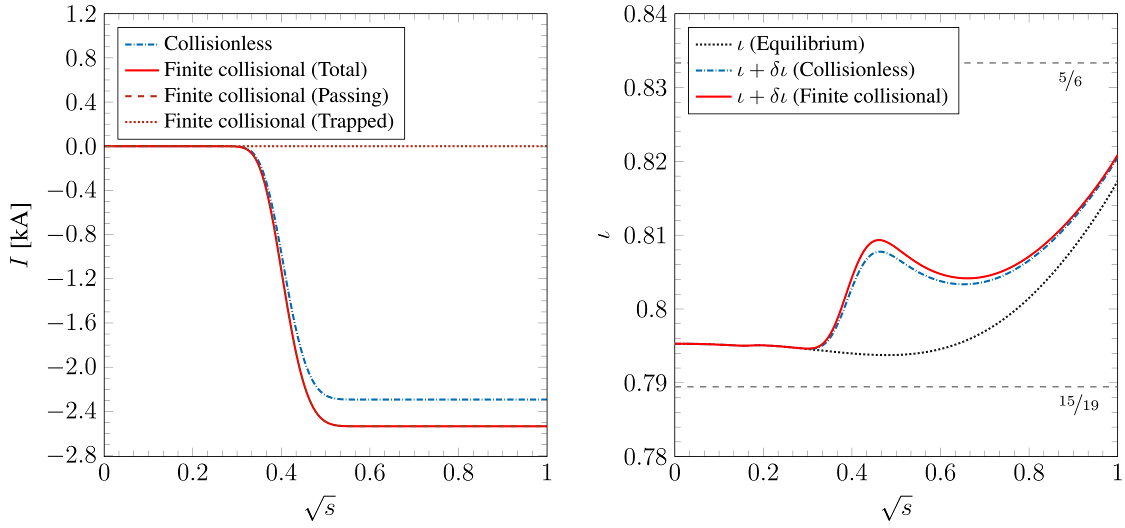

Figure 5.8: Scenario X2a - The left plot shows the total driven current within the volume enclosed by a given flux surface s for finite collisionality and in the mean free path regime (Left plot from G. Kapper, et al. [1]). The right plot shows an estimation of the influence of ECCD on the rotational transform profile, where the equilibrium value of ι is shown as dotted line. Resonances are indicated as horizontal dashed lines.

Scenario X2b

Scenario X2b (see Figure 5.9), which is characterized by very low $k_\parallel$, is special for X2 since almost the same fraction of energy is absorbed by trapped and passing particles, respectively, in a very narrow absorption region (roughly 1 cm) after the cold resonance position. As a consequence, a current is driven by both, trapped and passing particles, which is significantly underestimated by the collisionless model. In Figure 5.10 the integral kernel (5.6) of the parallel current density is depicted for the finite and collisionless model. As can be seen, a significant fraction of resonance line 2 is located inside the deeply trapped region. In contrast to the collisionless model where the distribution function is strictly antisymmetric and the integral kernel vanishes in the trapped domain, this leads to a significant co-current by trapped particles. In Figure 5.11 (left) the total driven parallel current indicates that account of finite plasma collisionality for this particular launch angle leads to an increase of the total current by almost one order of magnitude. The very narrow absorption region leads to a jump in the rotational transform profile as can be seen from Figure 5.11 (right). This current increase mainly results from a non-vanishing symmetric part of the generalized Spitzer function in the trapped domain referred to as the “Helander-Catto mechanism” [17].

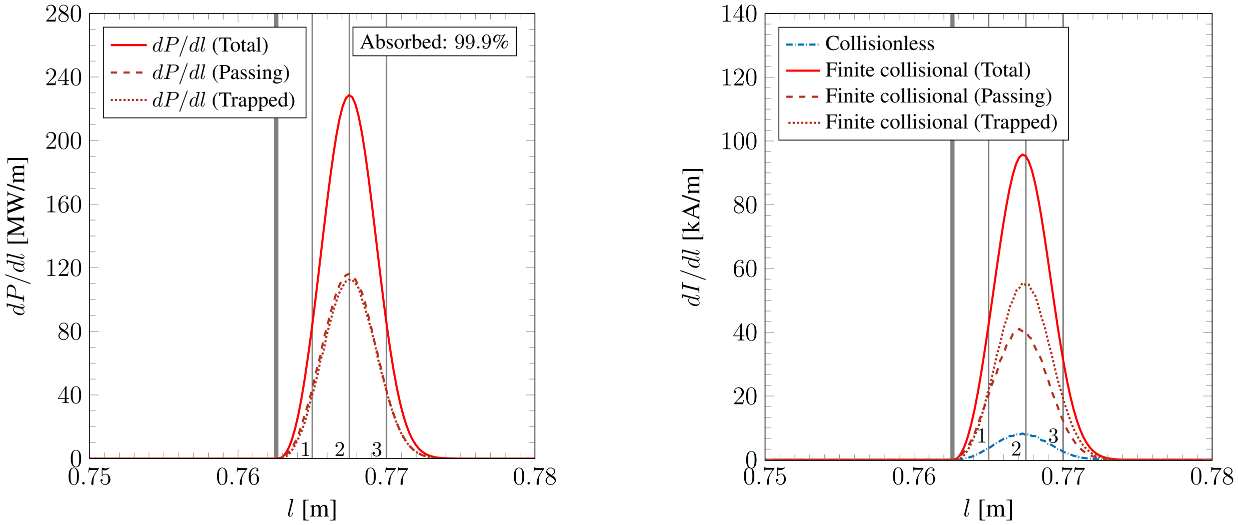

Figure 5.9: Scenario X2b - Locally absorbed power dP/dl (left) and locally driven current dI/dl (right) for the finite collisionality and the collisionless case as functions of the distance along the central ray l. Contributions of passing and trapped particles are depicted as dashed and dotted lines, respectively. The cold resonance position is marked with a thick vertical line. (From G. Kapper, et al. [1])

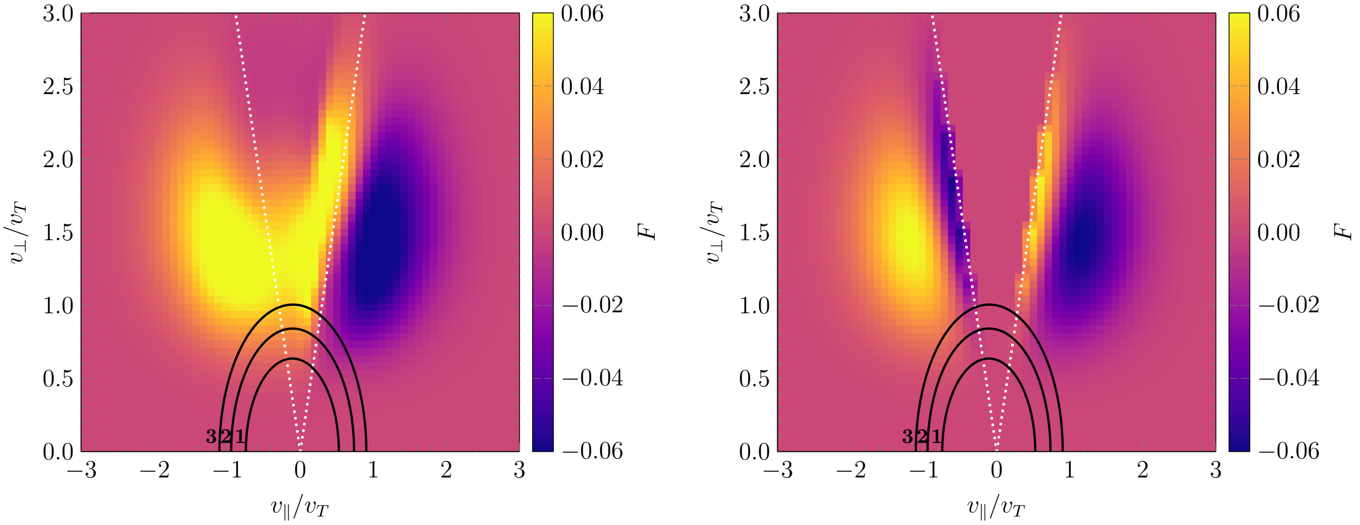

Figure 5.10: Scenario X2b - Current density integral kernel (5.6) as a function of the parallel and perpendicular normalized velocities for finite collisionality (left) and for the collisionless limit (right). The three numbered resonance lines correspond to respective positions indicated by numbered vertical lines in Figure 5.9. The trapped-passing boundary is shown by dashed lines. Colors are supersaturated in order to clarify the different signs of kernel F in different regions. (From G. Kapper, et al. [1])

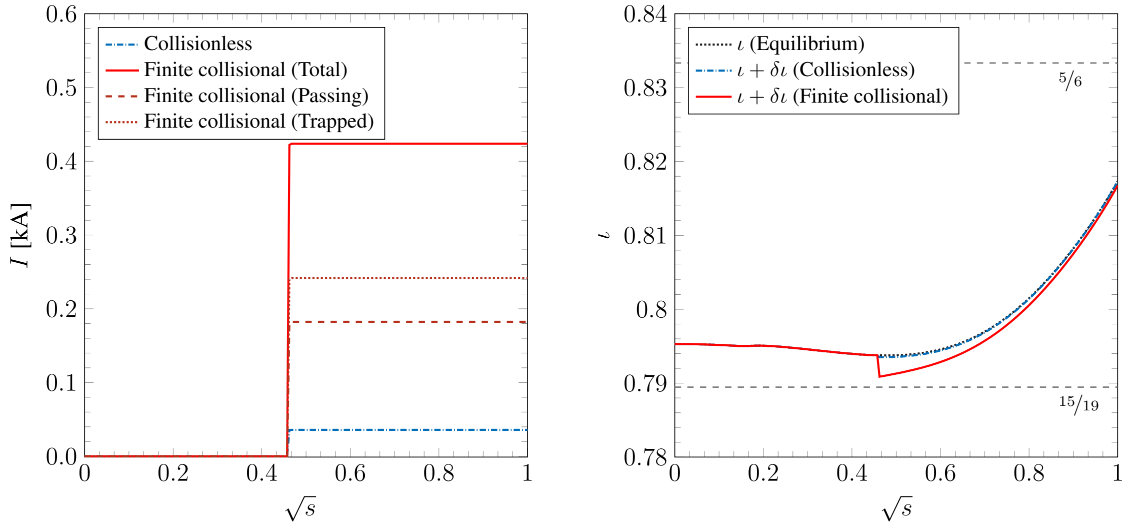

Figure 5.11: Scenario X2b - The left plot shows the total driven current within the volume enclosed by a given flux surface s for finite collisionality and in the mean free path regime. (Left plot from G. Kapper, et al. [1]) The right plot shows an estimation of the influence of ECCD on the rotational transform profile, where the equilibrium value of ι is shown as dotted line. Resonances are indicated as horizontal dashed lines.

In addition, a scan over the toroidal angle β at a fixed poloidal launch angle $\alpha = 18.75$ deg is given in Figure 5.12. As can be seen, for small toroidal launch angles, a significant amount of energy is absorbed by trapped particles, resulting in a current which is clearly underestimated by the collisionless model.

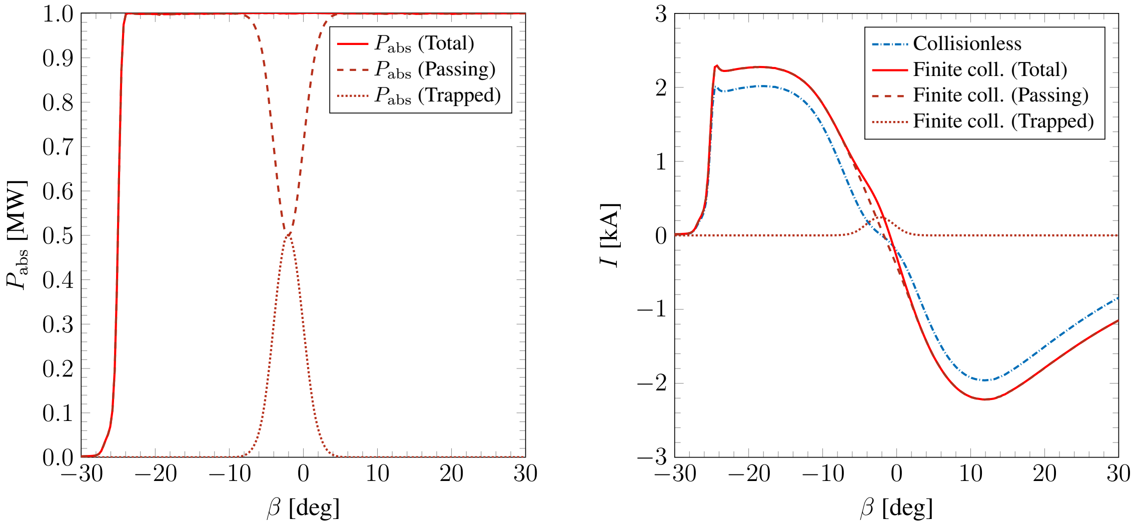

Figure 5.12: Absorbed power (left) and total driven current (right) of a X2-beam with 1 MW input power by passing (dashed) and trapped (dotted) particles as functions of the toroidal launch angle β at fixed poloidal angle $\alpha = 18.75$ deg. (From G. Kapper, et al. [1])

5.3.2 High density scenario - O2-mode

In contrast to the X2-mode, the plasma is optically gray for the O2-mode, thus the energy of the wave is not fully absorbed within a single pass. The cut-off density is twice the cut-off density of X2, which makes the O2-scenario applicable for high density plasmas. 2D launch angle scans in Figure 5.13, similar to scans of Figure 5.5 for X2, show that the sign of the total driven current by passing particles is mainly determined by the toroidal launch angle which mainly determines the parallel wave number $k_{\|}$. However, the sign of the total current driven by trapped particles is mainly determined by the poloidal position of the absorption region. This is in agreement with the behavior of the pitch-angle integral of the generalized Spitzer function in the trapped domain (see Eq. (5.1)) in Figure 5.4. Also for the O2-scenario two particular launch angles are investigated, namely ($\alpha = 5$ deg, $\beta = 20$ deg), which is the same as X2a, and ($\alpha = 0$ deg, $\beta = -10$ deg), which are in the following referred to as O2a and O2b, respectively.

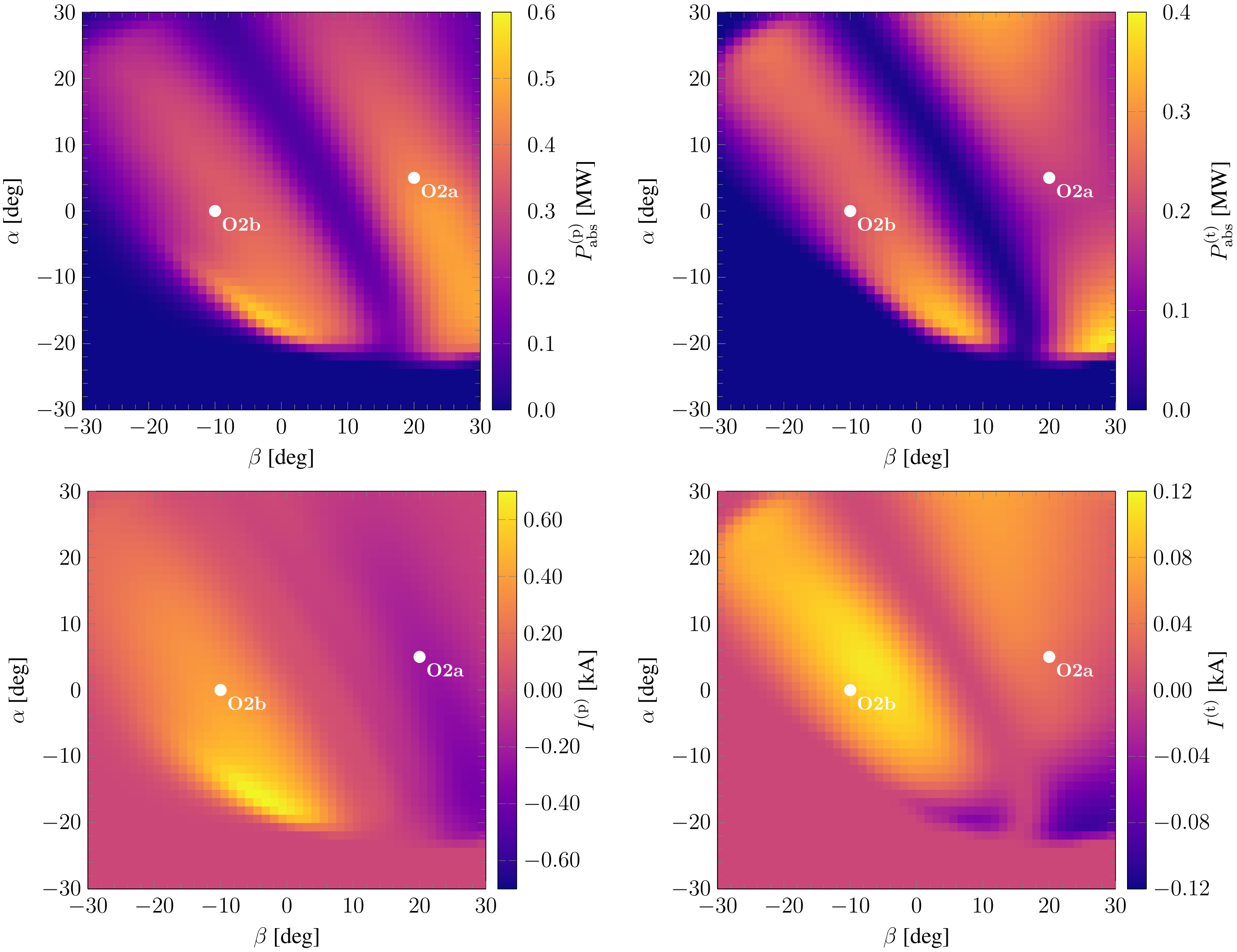

Figure 5.13: O2-mode - Total absorbed power (upper plane) and total driven current (lower plane) of a beam with 1 MW input power as functions of the toroidal (β) and poloidal (α) launch angle by passing particles (left) and trapped particles (right). Two particular launch angles, depicted as O2a and O2b, are then studied in more detail. (From G. Kapper, et al. [1])

Scenario O2a

In launch scenario O2a (Figure 5.14) a major fraction of energy is absorbed by passing particles before the cold resonance surface, and a significant amount is also absorbed by trapped particles after the cold resonance surface. The resonant parallel velocity changes its sign after the cold resonance position, thus leading to both, co- and counter-current by passing particles at different sides of the cold resonance, respectively. However, the significant amount of trapped particles involved in the absorption process leads to a pertinent current in contrast to the collisionless model. For detailed investigation of the different current drive mechanisms, the integral kernel (5.6) of the current density is presented in Figure 5.15. The resonance line at position 1 is fully located in the passing region, what results in a counter-current drive by passing particles only. Integration along resonance line 2 covers both, passing and trapped region. Here, a co-current is generated by a non-vanishing symmetric part of the generalized Spitzer function in the trapped domain. The resonance line at position 3 is almost fully located in the passing domain, which results in a co-current by passing particles and almost no contribution from trapped particles. As can be seen in Figure 5.16 (left), the increase of the total driven current by passing particles is mitigated by the different sign of the current by trapped particles. Despite that the total current does not significantly differ between the two collision models, the local difference of iota is clearly seen from Figure 5.16 (right). In order to maximize the current drive, a scenario has to be found where both, current driven by trapped and passing particles, have the same sign and where absorption processes prohibit damping of the current due to the change of the sign of the resonant parallel velocity when passing the cold resonance position. Such a launch angle scenario has been found and is presented in the following section.

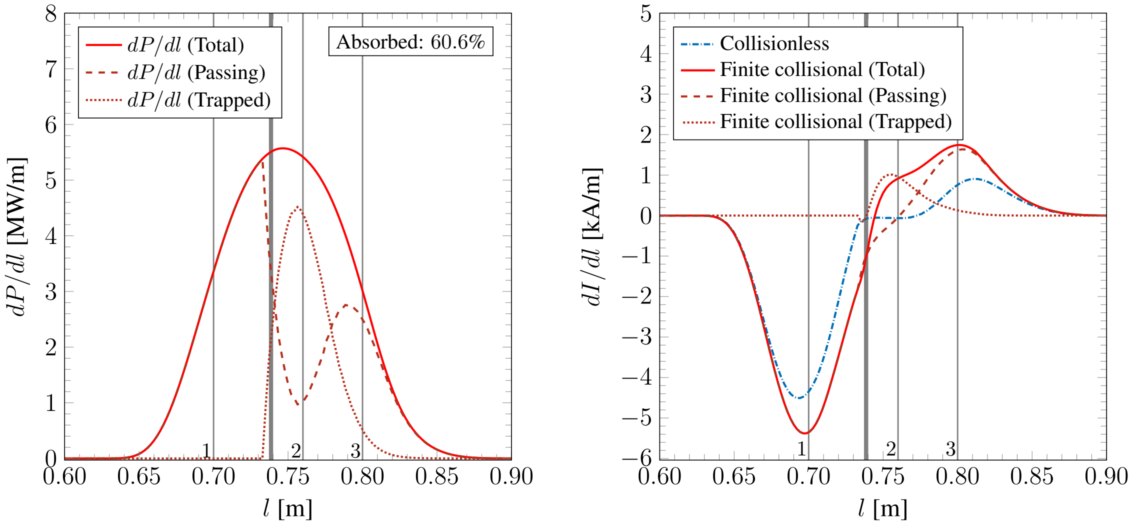

Figure 5.14: Scenario O2a - Locally absorbed power dP/dl (left) and locally driven current dI/dl (right) for the finite collisionality and the collisionless case as functions of the distance along the central ray l. Contributions of passing and trapped particles are depicted as dashed and dotted lines, respectively. The cold resonance position is marked with a thick vertical line. (From G. Kapper, et al. [1])

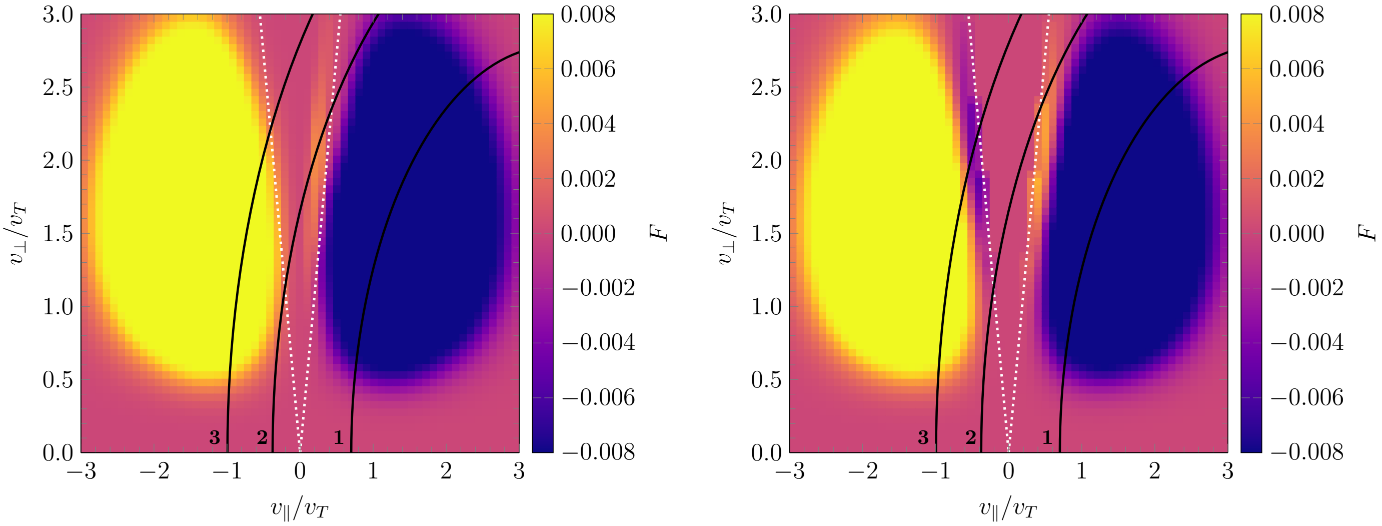

Figure 5.15: Scenario O2a - Current density integral kernel (5.6) as a function of the parallel and perpendicular normalized velocities for finite collisionality (left) and for the collisionless limit (right). The three numbered resonance lines correspond to respective positions indicated by numbered vertical lines in Figure 5.14. The trapped-passing boundary is shown by dashed lines. Colors are supersaturated in order to clarify the different signs of kernel F in different regions. (From G. Kapper, et al. [1])

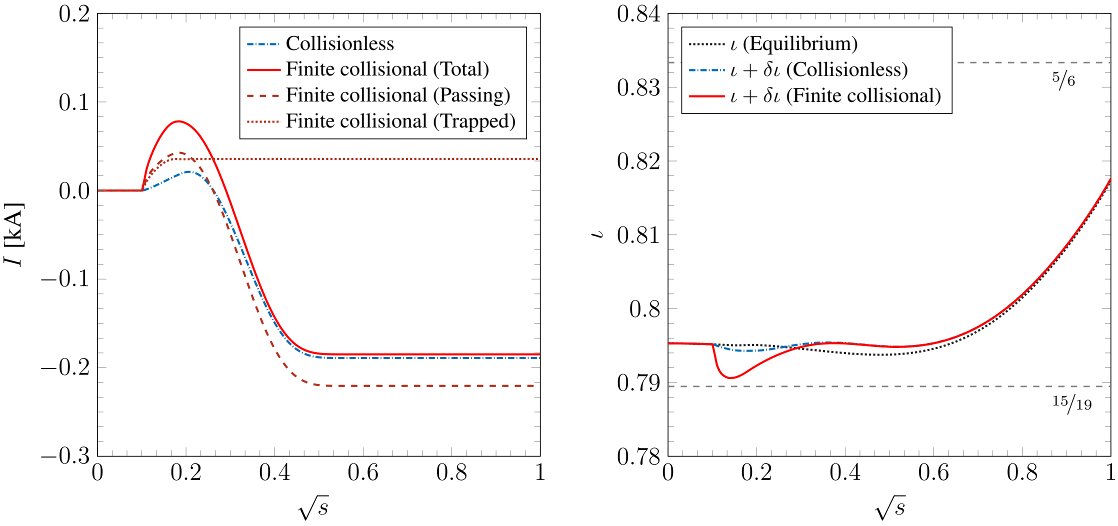

Figure 5.16: Scenario O2a - The left plot shows the total driven current within the volume enclosed by a given flux surface s for finite collisionality and in the mean free path regime. (Left plot G. Kapper, et al. [1]) The right plot shows an estimation of the influence of ECCD on the rotational transform profile, where the equilibrium value of ι is shown as dotted line. Resonances are indicated as horizontal dashed lines.

Scenario O2b

In scenario O2b (Figure 5.17) the current by trapped particles significantly increases the total driven current since the counter-current by passing particles is not strong enough to mitigate this effect. In Figure 5.18, where the current density kernel (5.6) is plotted, it is clearly seen that at resonance position 1 the whole current is produced by passing particles, while in contrast to the collisionless model, at positions 2 and 3 there is a non-vanishing contribution to the generated current in the trapped domain close to the boundary layer. As seen from the total driven current in Figure 5.19, the collisionless model underestimates the current by 60%, however the effect on iota at the edge is negligible.

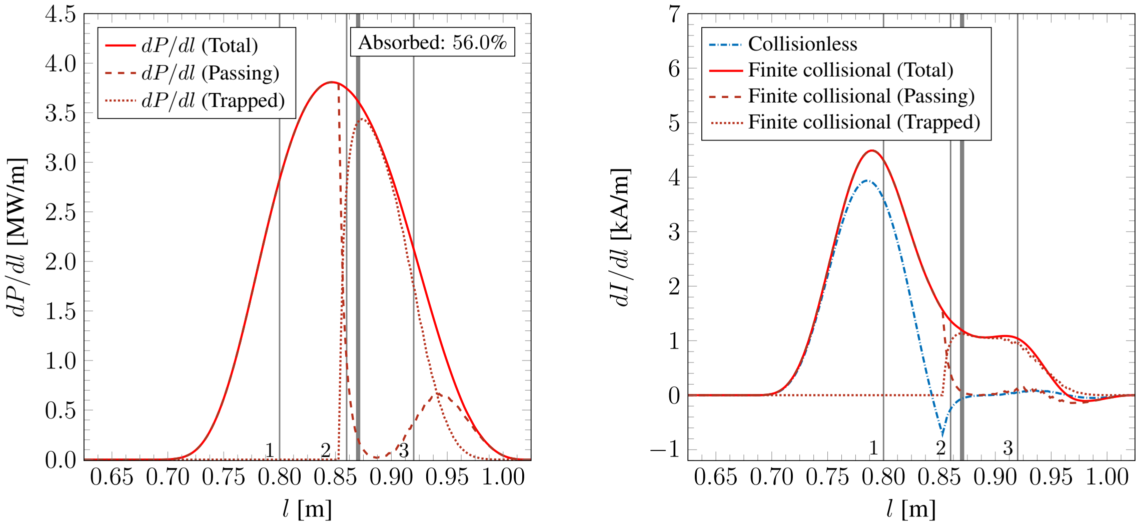

Figure 5.17: Scenario O2b - Locally absorbed power dP/dl (left) and locally driven current dI/dl (right) for the finite collisionality and the collisionless case as functions of the distance along the central ray l. Contributions of passing and trapped particles are depicted as dashed and dotted lines, respectively. The cold resonance position is marked with a thick vertical line. (From G. Kapper, et al. [1])

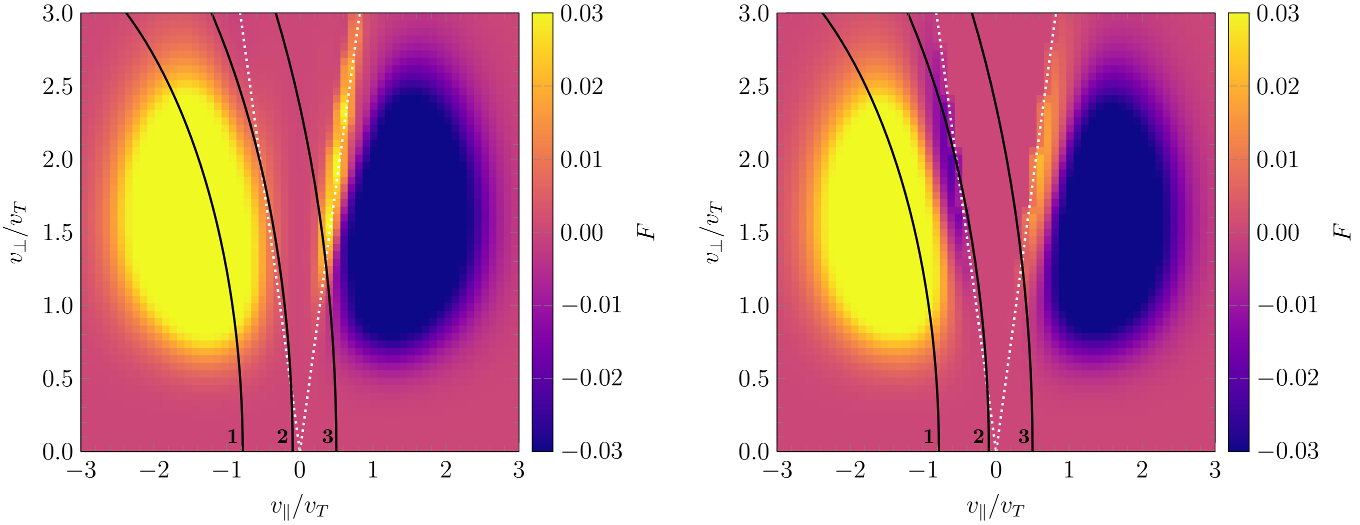

Figure 5.18: Scenario O2b - Current density integral kernel (5.6) as a function of the parallel and perpendicular normalized velocities for finite collisionality (left) and for the collisionless limit (right). The three numbered resonance lines correspond to respective positions indicated by numbered vertical lines in Figure 5.17. The trapped-passing boundary is shown by dashed lines. Colors are supersaturated in order to clarify the different signs of kernel F in different regions. (From G. Kapper, et al. [1])

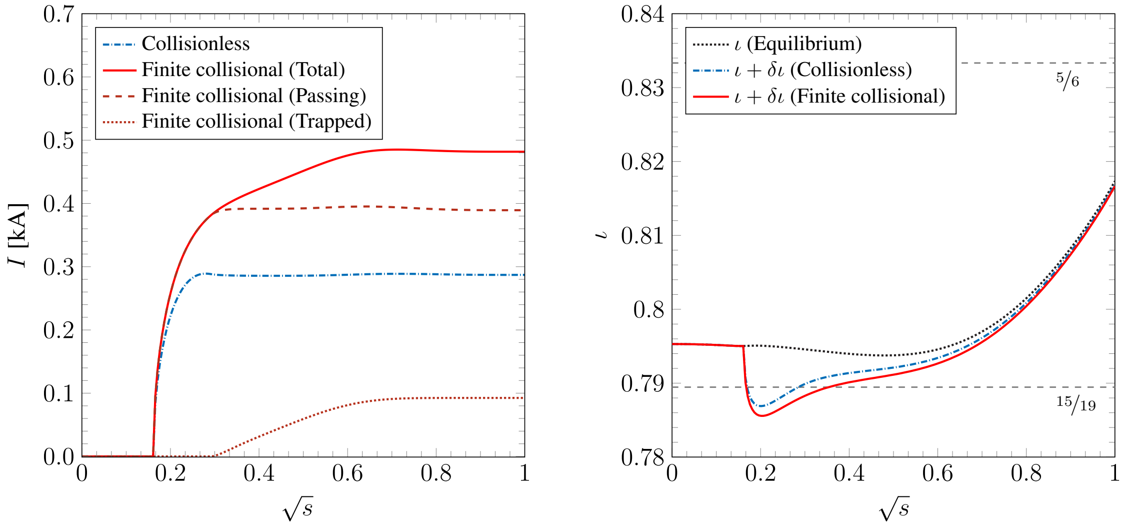

Figure 5.19: Scenario O2b - The left plot shows the total driven current within the volume enclosed by a given flux surface s for finite collisionality and in the mean free path regime (Left plot from G. Kapper, et al. [1]). The right plot shows an estimation of the influence of ECCD on the rotational transform profile, where the equilibrium value of ι is shown as dotted line. Resonances are indicated as horizontal dashed lines.

5.3.3 Current drive mechanisms

Out of all figures, Figure 5.18 is the best to illustrate all three current drive mechanisms involved, which do not require momentum input. First, and the strongest of them, is the Fisch-Boozer mechanism [11] which results from the dependence of momentum relaxation time on the position in the velocity space due to such a dependence of the local collision time. This mechanism prevails in velocity space regions where F is negative for $v_\parallel > 0$ and, respectively, positive for $v_\parallel < 0$ (F is with high accuracy antisymmetric there). Another mechanism can be called a "collisional Ohkawa effect", called also a "trapped particle effect" in Ref. 68. This mechanism also follows from the momentum relaxation time dependence on the velocity which is induced now by the proximity of the trapped particle region ("momentum loss cone"). The region where this mechanism prevails can be seen in the collisionless figure, Figure 5.18 (right), near the trapped-passing boundary in the passing particle domain. There, the sign of F changes to the opposite with respect to the sign of F in the regions with Fisch-Boozer mechanism. It should be noted that the term "collisional Ohkawa effect" is used here in order to distinguish from the conventional Ohkawa effect [69], where the current is generated by RF-diffusion alone which enforces the particle exchange between trapped and passing regions. In turn, the "collisional Ohkawa effect" does not require the capability from the RF-diffusion to move particles into the loss cone directly. It is sufficient for this diffusion just to move particles closer to the trapped-passing boundary and the rest is completed by collisions. Finally, in addition to these two mechanisms which are basically described by the antisymmetric part of the generalized Spitzer function, also the "Helander-Catto mechanism" can be seen in the collisional figure, Figure 5.18 (left), where the symmetric part of F makes a contribution in the trapped particle domain and in the vicinity of the trapped-passing boundary in the passing region.

5.3.4 Influence of ECCD on iota at the plasma edge

Following the formalism of Ref. 70, the estimations of iota as presented in Figures 5.8, 5.11, 5.16, and 5.19 are performed with the unperturbed 3D magnetic equilibrium and fixed plasma parameter profiles. This can be understood as the first iteration step of a self-consistently coupled code combination of the ray-tracing code, the equilibrium code, the transport code and the drift kinetic equation solver. However, this first order estimate is sufficient to see that the rotational transform ι is indeed influenced at the absorption region of the wave and that the effect is underestimated by the collisionless model. However, for all investigated launch scenarii the iota value at the edge is not significantly modified. This can be explained by a simple cylindrical model,

$$\iota(r) = \frac{2I(r)R_0}{cB_0 r^2}, \tag{5.7}$$

where $I = I(r)$ is the toroidal current through the cross-section limited by the flux surface of radius r, R_0 is the major radius, c is the speed of light, and B_0 is the magnetic field module. As can be seen, a change of iota in the core decays with $1/r^2$ and therefore becomes small at the edge. If it is necessary to balance the bootstrap current in order to preserve the position of the island divertor, then iota has to be controlled at the plasma edge. For highly localized absorption, what is typical for small launch angles in tokamaks and stellarators, the total driven current $I(r)$ almost jumps from zero for $r < r_{\mathrm{abs}}$ to its maximum for $r > r_{\mathrm{abs}}$, where r_{abs} is the radius where the wave absorption has its maximum. In case of power deposition close to the axis, the change of iota at radii $r \approx r_{\mathrm{abs}}$ has to be by $(a/r_{\mathrm{abs}})^2$ times larger than at the edge where $r = a$ with a being the radius of the outer flux surface. Such huge modification of iota in the core would introduce a higher probability for instabilities. In order to avoid these problems the current drive should be off-axis with the absorption region far enough from the axis such that $r_{\mathrm{abs}} \sim a$. Since at outer radii the plasma is more collisional, the collisional effects on the generalized Spitzer function as computed by NEO-2 become even more important.

5.3.5 Preliminary results with relativistic collision operator

The impact of using a fully relativistic collision model for the precomputation by NEO-2 as discussed in Section 2.4 on the total driven current in the scenario O2b has been investigated. As can be seen from Figure 5.20 the total current decreases by $\sim 4\%$ when a fully relativistic collision model is applied. This is in agreement with the benchmarks of the generalized Spitzer function for various relativistic temperatures as shown in Section 4.3.

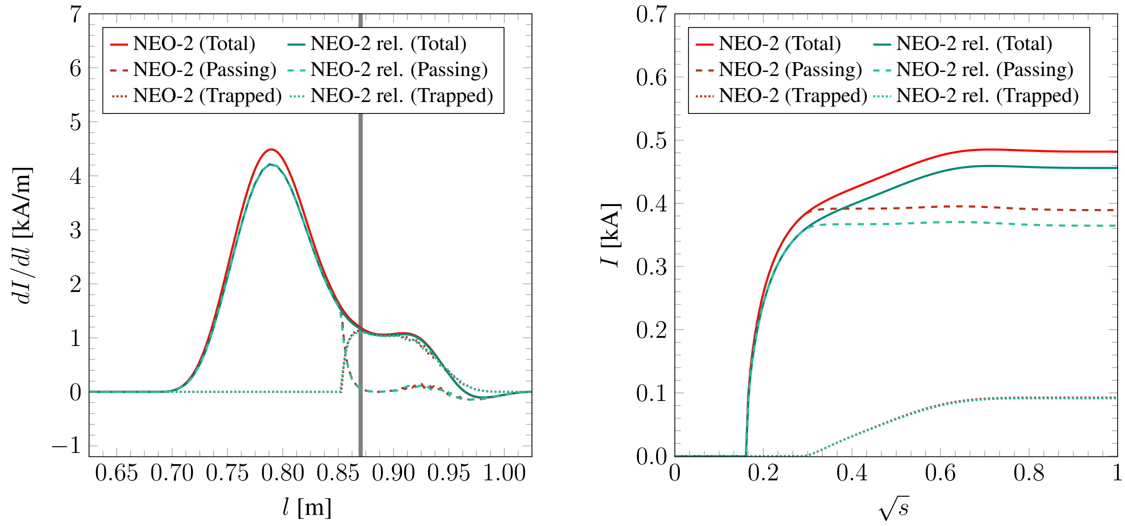

Figure 5.20: Left plot - Locally driven current dI/dl as function of the distance along the central ray l computed in the non-relativistic limit (red lines) and computed with a fully relativistic collision model (green). Contributions of passing and trapped particles are depicted as dashed and dotted lines, respectively. The cold resonance position is marked with a thick vertical line. Right plot - Total driven current within the volume enclosed by a given flux surface s computed in the non-relativistic limit (red line) and computed with a fully relativistic collision model (green line).

5.4 Conclusion

It has been shown that finite collisionality effects have an impact on the total current driven in both, ECCD scenarii where the wave energy is fully absorbed by passing particles and in scenarii where also trapped particles are involved in the absorption process. For a proper description of these effects the generalized Spitzer function was computed by the drift kinetic equation solver NEO-2 using the full linearized Coulomb collision operator for a high-mirror configuration of Wendelstein 7-X using realistic plasma parameters representing an initial stage of device operation. This 5D function has been used in the ray-tracing code TRAVIS and extends its various collisionless models. From the NEO-2 results it is seen that the generalized Spitzer function exhibits symmetric parts, which are responsible for current drive by waves with symmetric spectra [17], which can not be expected from interpolation between asymptotical collisionality limits. The impact of finite collisionality is not only restricted to the trapped domain but also leads to an offset of the generalized Spitzer function in the passing domain and therefore, to an increase of its antisymmetric part [15]. However, the significance of these finite collisionality effects decreases at higher particle velocities and lower collisionality. While the strong absorption of the X2-scenario for low and moderate densities results in efficient current generation, in high density plasmas this mode can not propagate through the plasma because of the wave cut-off. For such scenarii heating and current drive with the O2-mode might become necessary, where finite collisionality effects play a more significant role. Such a scenario can be found in Figure 7 of Ref. 71, where an operation at high density beyond the X2 cut-off is studied. Since the overall low absorption of the O2-mode, also multi-pass scenarii are planed, while in this thesis only the first pass was investigated. Summarizing, finite collisionality effects have been seen for both, the X2-resonance (mainly due to the offset of the generalized Spitzer function in the passing domain) as well as for the O2-resonance (mainly due to the symmetric part of the generalized Spitzer function). It should be noted that the high-collisionality model, as it was studied in Ref. 5, typically overestimates the current drive efficiency.

It has also been demonstrated that precomputation of NEO-2 results is possible not only for flux surface averaged quantities such as diffusion coefficients, but also for the high dimensional distribution function. Various techniques such as usage of the HDF5 file format and data caching capabilities of the provided data interface, as described in Chapter 3, allow for straightforward and fast access to the data. This precomputation process would not be possible within reasonable effort without the efficient parallelization of the code.

The ray-tracing code TRAVIS uses a fully relativistic approach for the computation of the resonance condition and the absorption and emission coefficients. Here, NEO-2 modeled the generalized Spitzer function in the non-relativistic limit (for the applied plasma parameters, this does not produce any significant error in ECCD calculations). However, in the course of this thesis the solver has been upgraded to apply the fully relativistic Coulomb collision model, where preliminary results have been presented.

Chapter 6

Synopsis

An average parallel plasma equilibrium current ("bootstrap current") arises in tokamaks and stellarators with increasing plasma temperature. While inductive parallel plasma currents are required in tokamaks in order to form a poloidal magnetic field, it might be necessary to balance the bootstrap current in stellarators. A powerful technique for this purpose is the so-called electron cyclotron current drive (ECCD), which is based on the cyclotron resonant interaction of electrons with incident radio-frequency waves [11]. The resonance region of such microwaves propagating through the plasma depends on the electron cyclotron frequency which is a function of the local magnetic field module. This allows for a well localized current drive and, as a result, for a controlled modification of the rotational transform profile. The latter is of special interest in the low-shear stellarator Wendelstein 7-X [60], where a net plasma current might create unintended low-order rational flux surfaces in the plasma core where large magnetic islands can be formed. In turn, in order to form an island divertor configuration [59] such a rational flux surface is intentionally placed at the plasma edge. Significant experimental experience on ECCD have been achieved at Wendelstein 7-AS which is extremely important for Wendelstein 7-X (see e.g. Refs. 72–74). In addition, non-inductive current drive is also of interest for establishing a steady state operation of tokamaks [75].

The efficiency of current drive in phase space is related to the classical Spitzer function for homogenous magnetic fields and for the high-collisionality limit [13], while for the long mean free path limit 2D bounce average procedures can be applied [12]. In these asymptotical collisionality limits the Spitzer function is strictly antisymmetric with respect to parallel velocity for all spatial points on a flux surface. However, for finite collisionality, where the solution to the conductivity problem is referred to as the generalized Spitzer function, this function has a finite value in the trapped particle region [14], what is in contrast to the collisionless limit, and also has an offset in the passing particle region [15]. These features can qualitatively be reproduced from solutions in asymptotical collisionality limits as demonstrated in Ref. 16. However as presented in this thesis, the generalized Spitzer function computed with the code NEO-2 [2], which solves the drift kinetic equation for plasmas with finite collisionality using the full linearized Coulomb collision operator without simplifications on the device geometry, exhibits also a feature which can not be expected from the low- and high-collisionality limit. This feature, which results from the combined action of the magnetic mirroring force and collisional effects, is due to the symmetric part of this function with respect to parallel velocity. This part is localized in velocity space around the trapped-passing boundary in the long mean free path regime and is also responsible for the bootstrap effect. This symmetric part can also be used for current drive by waves with symmetric spectra in the parallel wave number, as shown analytically in Ref. 17 and demonstrated later numerically in Refs. 5, 7, 18.

Originally, NEO-2 was developed for the computation of mono-energetic neoclassical transport coefficients in stellarators [50] and for the computation of distribution functions in tokamaks [18]. It has been developed at the Institute of Theoretical and Computational Physics at TU Graz in cooperation with the Institute of Plasma Physics, National Science Center "Kharkov Institute of Physics and Technology". In the scope of this thesis NEO-2 has been upgraded allowing for an efficient computation and storage of the high dimensional generalized Spitzer function for 3D toroidal geometry. A sufficient velocity resolution of the generalized Spitzer function requires a stable solution of the current drive problem up to several thermal velocities. Therefore, a generalized form of matrix elements of the NEO-2 collision operator resulting from discretization of this operator over the energy variable using the basis function expansion (Galerkin method) has been derived in the scope of this thesis. These basis functions can be chosen to be well suited for the specific kind of problem and do not have to be orthogonal. The transition from commonly used generalized Laguerre polynomials of order 3/2 (Sonine polynomials), which have also been used in the original NEO-2 version, to more localized B-splines extends the upper velocity limit of $\sim 3.5 v_T$, where v_T is the thermal velocity, as it was seen for Sonine polynomials at higher values. The solutions expanded in terms of different sets of basis functions have been benchmarked against analytical limits confirming that cubic B-splines are well suited for representation of the solution for this specific kind of problem. In addition, the generalization of the basis functions have not only been applied to the current drive problem but have also been successfully applied to NTV (Neoclassical Toroidal Viscosity) computations with a quasilinear version of the code NEO-2 [3], where the solution requires an even more localized basis, i.e., hat functions or quadratic B-splines.

An interface featuring straightforward access to precomputed NEO-2 datasets has been developed either as a standalone program or as library for ray-tracing codes. The latter has been used for combination of NEO-2 with the ray-tracing code TRAVIS [22] within the adjoint approach [21] in cooperation with the Max Planck Institute for Plasma Physics in Greifswald. With help of this interface, precomputed datasets from NEO-2 for a given plasma equilibrium with pertinent plasma parameter profiles are used as velocity-dependent current drive efficiency in TRAVIS. The code combination NEO-2/TRAVIS has been successfully applied to a high-mirror configuration of Wendelstein 7-X using realistic plasma parameter profiles at a rather low electron temperature [1, 5]. As presented in this thesis, finite plasma collisionality has a significant impact on the current drive efficiency and respective total driven current density in both, ECCD scenarii where the wave energy is fully absorbed by passing particles, and in scenarii where wave energy is also absorbed by trapped particles. The investigated scenarii involved the second harmonic extraordinary mode (X2) as well as the second harmonic ordinary mode (O2), which are the main heating scenarii of Wendelstein 7-X [67]. While the strong absorption of the X2-mode results in efficient current drive by passing particles, this method is limited to low and moderate plasma densities because of the wave cut-off. For high density experiments the O2-mode, which is typically poorly absorbed in the first pass, becomes necessary (see Fig. 7 of Ref. 71). The deeper penetration of this mode into the plasma core results in wave energy absorption also by trapped particles. However, in collisionless models the generalized Spitzer function vanishes in the trapped particle domain. This is in contrast to the results presented in this thesis, where the generalized Spitzer function has a finite value in the trapped region as well as a significant symmetric part. Since the sign of the driven current by this symmetric part depends on the region of absorption, a co- and counter current can be produced by variation of the microwave beam launch angle. For both scenarii, the O2- and the X2-resonance, a significant impact of collisional effects on the total driven current and as a result thereof a change of the rotational transform profile have been observed.

In scenarii studied here, the absorption takes place in the plasma core, whereas the change of iota decays with $1/r^2$, where r is the plasma radius. Thus, a change of iota close to the edge as required for the control of the position of the island divertor would require a huge change of iota in the core. Since this increases the likeliness for instabilities, an off-axis current drive simulation where the absorption region is far enough from the axis, is planned for the future. At such outer radii the plasma is more collisional and therefore the direct evaluation of the generalized Spitzer function with NEO-2 becomes even more important.

While in TRAVIS the position of the resonance line as well as absorption coefficients are evaluated using a fully relativistic approach, the generalized Spitzer function as provided by NEO-2 has been computed in the non-relativistic limit. This did not introduce a significant error for the given plasma parameters. However, in this thesis this limitation of NEO-2 has been removed by implementation of the fully relativistic Coulomb collision operator by Braams and Karney [19] as well as by direct evaluation of the collision operator from Beliaev and Budker [20]. Results have been successfully benchmarked against the fully relativistic code SYNCH [12], which solves the conductivity problem for arbitrary 3D toroidal geometries in the long mean free path limit.

Besides ECCD modeling, numerical studies on the mono-energetic bootstrap current coefficient in Wendelstein 7-X for a broad range of plasma collisionalities have been performed [2] and benchmarked to Ref. 50. Computations at extremely low collisionalities in the $1/\nu$ regime have only been possible due to the numerous upgrades of NEO-2 especially due to the code parallelization. Since the asymptotical limit [51, 52] is seen to be never reached with small (but finite) plasma collisionality, the NEO-2 results have been checked against various numerical artifacts. More precisely, variation of the starting point of the traced field line, the field line length, and the level distribution of the discretization scheme have confirmed the convergence of the results. In all pertinent runs the Onsager symmetry condition of the neoclassical transport coefficients matrix is well fulfilled within fault tolerance. (The Onsager symmetry of the transport coefficient matrix is not an intrinsic property of the solver and can therefore be used as a convergence criterion.) The gradient driven distribution function, which is responsible for the bootstrap current, has been studied in order to explain this behavior. The odd part of this function, representing the parallel current, shows that a huge part of this current is localized in the phase space near the boundaries between different classes of trapped particles. At irrational flux surfaces there are always such boundaries which contain the global trapped-passing boundary within their boundary layer of finite but very small width. Such boundaries affect the passing particle distribution function and therefore influence the bootstrap current. This effect of multiply trapped particles on the passing particle distribution is fully ignored in the well known Shaing-Callen derivation of the bootstrap coefficient (see Refs. 51, 52), however such an approximation cannot be justified at irrational flux surfaces in case of any finite plasma collisionality.

Summarizing, a workflow has been developed to perform electron cyclotron current drive simulations for a given magnetic equilibrium and pertinent plasma parameter profiles with the code combination NEO-2/TRAVIS. For the given equilibrium and plasma parameter profiles a visible influence of collisional effects on the driven current has been observed. NEO-2 has been upgraded to a fully relativistic drift kinetic equation solver making it ready for simulations of high temperature plasmas representing future reactor conditions.

Appendix A

Trubnikov potentials for perturbed distribution function

In this chapter the Trubnikov potentials [28],

$$\varphi_{b1}(\vartheta,\mathbf{v}) = -\frac{1}{4\pi}\int \mathrm{d}^3v'\frac{f_{b1}(\vartheta,\mathbf{v}')}{|\mathbf{v}-\mathbf{v}'|}, \tag{A.1}$$

$$\psi_{b1}(\vartheta,\mathbf{v}) = -\frac{1}{8\pi}\int \mathrm{d}^3v'|\mathbf{v}-\mathbf{v}'|f_{b1}(\vartheta,\mathbf{v}'), \tag{A.2}$$

are evaluated for the perturbed distribution function f_{b1}. The relative velocity module of the colliding particles with γ being the angle between the vectors $\mathbf{v}$ and $\mathbf{v}'$ is expressed by

$$|\mathbf{v}-\mathbf{v}'| \equiv u(v,v',\alpha) = \sqrt{v^2-2vv'\alpha+v'^2}, \tag{A.3}$$

where $\alpha = \cos\gamma$. Legendre polynomials form a complete set of basis functions to represent any function $f(\alpha)$ in the interval $-1 \leqslant \alpha \leqslant 1$ as follows,

$$f(\alpha) = \sum_{l=0}^{\infty} a_l P_l(\alpha), \tag{A.4}$$

with the expansion coefficients given by,

$$a_l = \frac{2l+1}{2}\int\limits_{-1}^{+1} \mathrm{d}\alpha f(\alpha)P_l(\alpha). \tag{A.5}$$

As defined in Ref. 76 the function $u(v, v', \alpha)^{-1}$ appearing in Eq. (A.1) is expanded as follows,

$$\frac{1}{u(v, v', \alpha)} = \sum_{l=0}^{\infty} \frac{v_<^l}{v_>^{l+1}} P_l(\alpha), \tag{A.6}$$

where P_l is the Legendre polynomial of degree l, $v_>$ is the larger of v and v', and $v_<$ is the smaller of v and v'. Substitution of Eq. (A.6) in (A.1) gives,

$$\begin{aligned} \varphi_{b1}(\vartheta, \mathbf{v}) =& -\frac{1}{4\pi} \int \mathrm{d}^3 v' \frac{f_{b1}(\vartheta, \mathbf{v}')}{u(v, v', \alpha)}, \\ =& -\frac{1}{4\pi} \sum_{l=0}^{\infty} \int\limits_0^{\infty} \mathrm{d}v' v'^2 \int\limits_{-1}^{+1} \mathrm{d}\lambda' f_{b1}(\vartheta, \mathbf{v}') \int\limits_0^{2\pi} \mathrm{d}\phi \frac{v_<^l}{v_>^{l+1}} P_l(\alpha), \end{aligned} \tag{A.7}$$

where

$$\int \mathrm{d}^3 v' \ldots = \int_0^{\infty} \mathrm{d}v' v'^2 \int_{-1}^{+1} \mathrm{d}\lambda' \int_0^{2\pi} \mathrm{d}\phi \ldots, \tag{A.8}$$

with ϕ and λ being the gyrophase and the pitch angle parameter, respectively. The angle γ is transformed to spherical coordinates as follows,

$$\alpha = \cos\gamma = \cos\theta \cos\theta' + \sin\theta \sin\theta' \cos(\phi - \phi'), \tag{A.9}$$

where θ and ϕ are the polar and azimuthal angle, respectively, and $\lambda = \cos(\theta)$. The addition theorem for spherical harmonics [77],

$$\begin{aligned} P_l(\alpha) =& P_l(\lambda) P_l(\lambda') + \\ &+ 2 \sum_{m=1}^{l} \frac{(l-m)!}{(l+m)!} P_l^{(m)}(\lambda) P_l^{(m)}(\lambda') \cos[m(\phi - \phi')], \end{aligned} \tag{A.10}$$

with $P_k^{(m)}$ being the associated Legendre polynomial of order m is used for evaluation of the integral over the gyrophase (gyrophase average in spherical coordinates [78]) as follows,

$$\frac{1}{\overline{u}} = \frac{1}{2\pi} \int\limits_0^{2\pi} \mathrm{d}\phi \frac{1}{u}$$

$$
\begin{aligned}
&=\frac{1}{2\pi}\int_0^{2\pi}\mathrm{d}\phi\sum_{l=0}^{\infty}\frac{v_<^l}{v_>^{l+1}}P_l(\lambda)P_l(\lambda')+\underbrace{\frac{1}{2\pi}\int_0^{2\pi}\mathrm{d}\phi f(\cos\phi)}_{=0}\\
&=\sum_{l=0}^{\infty}\frac{v_<^l}{v_>^{l+1}}P_l(\lambda)P_l(\lambda'), \qquad \text{(A.11)}
\end{aligned}
$$

where $f(\cos\phi)$ represents the second term of Eq. (A.10) which is periodic in ϕ. Eq. (A.11) and the definition of the perturbed distribution function f_{b1} as given in Eq. (2.156) are used to express Eq. (A.1) as follows,

$$
\begin{aligned}
\varphi_{b1}(\vartheta,\mathbf{v}) =&-\frac{1}{2}\sum_{m'=0}^{M}\sum_{l'=0}^{L}\sum_{l=0}^{\infty}g_{b,m',l'}(\vartheta)P_l(\lambda)\int_0^{\infty}\mathrm{d}v'v'^2 f_{b0}(v')\frac{v_<^l(v,v')}{v_>^{l+1}(v,v')}\varphi_{m'}\left(\frac{v'}{v_{Tb}}\right)\times\\
&\times\int_{-1}^{+1}\mathrm{d}\lambda' P_{l'}(\lambda')P_l(\lambda')\\
=&-\frac{1}{2}\sum_{m'=0}^{M}\sum_{l=0}^{L}P_l(\lambda)\frac{2}{2l+1}g_{b,m',l}(\vartheta)\int_0^{\infty}\mathrm{d}v'v'^2 f_{b0}(v')\frac{v_<^l(v,v')}{v_>^{l+1}(v,v')}\varphi_{m'}\left(\frac{v'}{v_{Tb}}\right)\\
=&-\frac{1}{2}\sum_{m'=0}^{M}\sum_{l=0}^{L}g_{b,m',l}(\vartheta)\frac{2}{2l+1}P_l(\lambda)\times\\
&\times\left[v^{-l-1}\int_0^{v}\mathrm{d}v'v'^2 f_{b0}(v')v'^l\varphi_{m'}\left(\frac{v'}{v_{Tb}}\right)+\right.\\
&\left.+\ v^l\int_v^{\infty}\mathrm{d}v'v'^2 f_{b0}(v')v'^{(-l-1)}\varphi_{m'}\left(\frac{v'}{v_{Tb}}\right)\right], \qquad \text{(A.12)}
\end{aligned}
$$

where the orthogonality of Legendre polynomials,

$$
\int_{-1}^{+1}\mathrm{d}\lambda P_{l'}(\lambda)P_l(\lambda)=\frac{2}{2l+1}\delta_{l',l} \qquad \text{(A.13)}
$$

was used and the integral boundaries were split up in order to integrate the functions $v_>(v,v')$ and $v_<(v,v')$. For the evaluation of (A.2)

$$
\psi_{b1}(\vartheta,\mathbf{v}) = -\frac{1}{8\pi}\int\mathrm{d}^3v'\frac{u(v,v',\alpha)^2}{u(v,v',\alpha)}f_{b1}(\vartheta,\mathbf{v}')
$$

$$= -\frac{1}{8\pi}\int\limits_{0}^{\infty} \mathrm{d}v' v'^2 \int\limits_{-1}^{+1} \mathrm{d}\lambda' f_{b1}(\vartheta, \mathbf{v}') \int\limits_{0}^{2\pi} \mathrm{d}\phi \frac{u(v, v', \alpha)^2}{u(v, v', \alpha)}, \tag{A.14}$$

the term u^2/u is expanded via Legendre polynomials with the coefficients (A.5),

$$\begin{aligned} a_l =& \frac{2l+1}{2}\int\limits_{-1}^{+1} \mathrm{d}\alpha \frac{u^2}{u} P_l(\alpha) \\ =& \frac{2l+1}{2}\int\limits_{-1}^{+1} \mathrm{d}\alpha \frac{v_<^2 - 2v_< v_> \alpha + v_>^2}{u} P_l(\alpha) \\ =& \frac{2l+1}{2}\int\limits_{-1}^{+1} \mathrm{d}\alpha \sum_{l'=0}^{\infty} \frac{v_<^{l'}}{v_>^{l'+1}} P_{l'}(\alpha)(v_<^2 - 2v_< v_> \alpha + v_>^2) P_l(\alpha). \end{aligned} \tag{A.15}$$

Using the orthogonality of Legendre polynomials and the fact the following integral vanishes unless $l' = l \pm 1$ (see Eq. (3.31) in Ref. 76),

$$\int\limits_{-1}^{+1} \mathrm{d}\alpha \alpha P_{l'}(\alpha) P_l(\alpha) = \begin{cases} \frac{2(l+1)}{(2l+1)(2l+3)} & \text{for } l' = l+1 \\ \frac{2l}{(2l-1)(2l+1)} & \text{for } l' = l-1 \\ 0 & \text{otherwise} \end{cases} \tag{A.16}$$

Eq. (A.15) evaluates to,

$$a_l = \frac{v_<^{l+2}}{v_>^{l+1}} \frac{1}{2l+3} - \frac{v_<^{l}}{v_>^{l-1}} \frac{1}{2l-1}. \tag{A.17}$$

Performing similar steps as in (A.12) finally gives the expression,

$$\begin{aligned} \psi_{b1}(\vartheta, \mathbf{v}) =& -\frac{1}{4}\sum_{m'=0}^{M}\sum_{l=0}^{L} g_{b,m',l}(\vartheta) \frac{2}{2l+1} P_l(\lambda) \times \\ & \times \left[\frac{1}{2l+3} v^{-l-1} \int\limits_{0}^{v} \mathrm{d}v' v'^{l+4} f_{b0}(v') \varphi_{m'}\left(\frac{v'}{v_{Tb}}\right) - \right. \\ & - \frac{1}{2l-1} v^{-l+1} \int\limits_{0}^{v} \mathrm{d}v' v'^{l+2} f_{b0}(v') \varphi_{m'}\left(\frac{v'}{v_{Tb}}\right) + \end{aligned}$$

$$+\frac{1}{2l+3}v^{l+2}\int\limits_{v}^{\infty}\mathrm{d}v'\frac{1}{v'^{l-1}}f_{b0}(v')\varphi_{m'}\left(\frac{v'}{v_{Tb}}\right)-$$

$$\left.-\frac{1}{2l-1}v^{l}\int\limits_{v}^{\infty}\mathrm{d}v'\frac{1}{v'^{l-3}}f_{b0}(v')\varphi_{m'}\left(\frac{v'}{v_{Tb}}\right)\right]. \tag{A.18}$$

Appendix B

Interface documentation

Introduction

Technical details of the NEO-2 interface as given in this appendix have been presented in the following internal EUROfusion report:

- G. Kapper, W. Kernbichler, S. V. Kasilov, and N. B. Marushchenko, *Interface to the generalized Spitzer function computed by NEO-2*, Technical Report (EUROfusion, 2015)

The interface to access the precomputed distribution function by NEO-2 is developed to be used straightforward without any special knowledge about the internal workflows. Therefore, only three subroutines have to be called from an external code after the module is included:

```
use spitzerinterface_neo2, &
    only: init_spitzerinterface, &
         gfunc_neo2, &
         deinit_spitzerinterface
...
call init_spitzerinterface()
...
call gfunc_neo2(s, theta, phi, xtr, xpa, g, gtr, gpa)
...
call deinit_spitzerinterface()
```

The module has to be initialized before its first usage. This process reads the interface settings file, opens the HDF5 data file, and caches meta data for faster data access. The interface reconstructs the generalized Spitzer function and its derivatives with respect to the perpendicular and parallel velocity at an arbitrary point in the torus with one call of the subroutine `gfunc_neo2()`. For reasons of usability it is not critical if the interface has already been initialized since this method checks the initialization state and performs the initialization on its first call if necessary. However, the initialization could take some time, therefore, it is suggested to be done at the start of the program where it is not performance critical.

Parameters

The parameters of `gfunc_neo2()` are described in detail in the following list:

- **Parameter `s`**
  - **Direction**: Input
  - **Type**: real(kind=dp)
  - **Dimension**: Scalar
  - **Definition**: Normalized toroidal flux (flux surface label s)
- **Parameter `theta`**
  - **Direction**: Input
  - **Type**: real(kind=dp)
  - **Dimension**: Scalar
  - **Definition**: Poloidal angle in Boozer coordinates (ϑ_b)
- **Parameter `phi`**
  - **Direction**: Input
  - **Type**: real(kind=dp)
  - **Dimension**: Scalar
  - **Definition**: Toroidal angle in Boozer coordinates (φ_b)

- **Parameter** `xtr`
  - **Direction**: Input
  - **Type**: real(kind=dp)
  - **Dimension**: Scalar or one-dimensional vector
  - **Definition**: Perpendicular velocity component with respect to the magnetic field line and normalized to the thermal velocity ($x_\perp$)

- **Parameter** `xpa`
  - **Direction**: Input
  - **Type**: real(kind=dp)
  - **Dimension**: Scalar or one-dimensional vector
  - **Definition**: Parallel velocity component with respect to the magnetic field line and normalized to the thermal velocity ($x_\parallel$)

- **Parameter** `g`
  - **Direction**: Output
  - **Type**: real(kind=dp)
  - **Dimension**: Scalar or one-dimensional vector
  - **Definition**: Generalized Spitzer function (g_{sp})

- **Parameter** `gtr`
  - **Direction**: Output
  - **Type**: real(kind=dp)
  - **Dimension**: Scalar or one-dimensional vector
  - **Definition**: Derivative of the generalized Spitzer function with respect to the perpendicular velocity ($\partial g_{\mathrm{sp}}/\partial x_\perp$)

- **Parameter** `gpa`
    - **Direction**: Output
    - **Type**: real(kind=dp)
    - **Dimension**: Scalar or one-dimensional vector
    - **Definition**: Derivative of the generalized Spitzer function with respect to the parallel velocity ($\partial g_{\mathrm{sp}}/\partial x_{\parallel}$)

It should be noted that the kind `dp` of the real data type is set to 8 in the code which corresponds to the double precision type. The parameters `xtr` and `xpa` can be scalars or vectors. In case of vectors, the quantities `xtr`, `xpa`, `g`, `gtr`, and `gpa` have to be of the same size and have to be already allocated. Using this option, a scan in velocity space can be simply performed with only one function call.

Configuration

The interface is configured via a Fortran namelist file `spitzerinterface.in`. This avoids the necessity of recompilation if parameters are changed which are connected to the interpolation and normalization process. Here an example of a default settings file is given with subsequent description of each parameter.

```
&spitzerinterface
  input_filename = 'w7x-m24li.h5'
  lsw_interp_s = .true.
  lsw_interp_theta = .true.
  lsw_interp_phi = .true.
  lsw_remove_offset = .true.
  isw_gnorm = 3
  enable_cache = .true.
  debug = .false.
/
```

- **Parameter** `input_filename`
    - **Type**: character
    - **Default**: 'results.h5'
    - **Definition**: Specifies the HDF5 file containing the precomputed datasets from preceded NEO-2 runs.

- **Parameter** `lsw_interp_s`
    - **Type**: logical
    - **Values**: true or false
    - **Default**: true
    - **Definition**: Enables/Disables the linear interpolation along flux surfaces. If false, a nearest neighbor interpolation is performed.

- **Parameter** `lsw_interp_theta`
    - **Type**: logical
    - **Values**: true or false
    - **Default**: true
    - **Definition**: Enables/Disables the linear interpolation along the poloidal angle. If false, a nearest neighbor interpolation is performed.

- **Parameter** `lsw_interp_phi`
    - **Type**: logical
    - **Values**: true or false
    - **Default**: true
    - **Definition**: Enables/Disables the linear interpolation along the toroidal angle. If false, a nearest neighbor interpolation is performed.

- **Parameter** `lsw_remove_offset`
    - **Type**: logical
    - **Values**: true or false
    - **Default**: true
    - **Definition**: Enables/Disables the offset correction as described in Section 2.2.4.

- **Parameter** `isw_gnorm`
    - **Type**: logical
    - **Values**: 2 or 3
    - **Default**: 3
    - **Definition**: Defines the normalization of the generalized Spitzer function.
        - Value 2 activates the standard NEO-2 normalization,

          $$el_c \left\langle \int \mathrm{d}^3 v g Q_{\mathrm{RF}} \right\rangle = \frac{\langle j_\parallel B \rangle}{B_{\mathrm{ref}}} = \frac{\langle j_\parallel B \rangle}{\langle B^3 \rangle} \langle B^2 \rangle \tag{B.1}$$

          where e is the particle charge, l_c is the mean free path, Q_{RF} is the quasilinear particle source in phase space, $j_\parallel$ is the current in the direction of the magnetic field line, and B_{ref} is a reference magnetic field (usually $B_{\mathrm{ref}} = B_{00}$, where B_{00} is the $(m = 0,\ n = 0)$-harmonic of the magnetic field expansion in Boozer coordinates). $< \ldots >$ denotes flux surface average, which is the average over the volume between neighboring flux surfaces.
        - Value 3 activates the standard TRAVIS normalization,

          $$el_c \left\langle \int \mathrm{d}^3 v g Q_{\mathrm{RF}} \right\rangle = \langle j_\parallel \rangle \tag{B.2}$$

- **Parameter** `enable_cache`
  - **Type**: logical
  - **Values**: true or false
  - **Default**: true
  - **Definition**: Enables the caching facility as described in Section 3.3. The influence on the runtime is described in Section B.

- **Parameter** `debug`
  - **Type**: logical
  - **Values**: true or false
  - **Default**: false
  - **Definition**: Enables/Disables debug output.

Performance

Figure B.1 shows the dependence of runtime on the number of different spatial points as queried from the interface. As can be seen the runtime is of the order $\mathcal{O}(n)$, where n is the number of queried spatial points. On average the time for querying one spatial point is slightly larger than one millisecond on the test system using a HDF5 file with a size of 39 Gigabyte. As stated in Section 3.3 a caching mechanism was developed in order not to read the HDF5 file if the spatial position from one to the subsequent query stays the same, e.g., as used for velocity space scans at fixed spatial coordinate. Figure B.2 shows the runtime for a constant spatial point for different velocities with and without the caching mechanism, respectively. The order of the runtime without cache is $\mathcal{O}(n)$, where n is the number of probed pitch angles. However, the cache keeps the data of the involved propagators (four per spatial point for 3D linear interpolation) in the memory until the spatial point is changed. Therefore, the number of disk operations is effectively reduced. Compared to the runtime without cache, the runtime with cache is close to the order $\mathcal{O}(1)$.

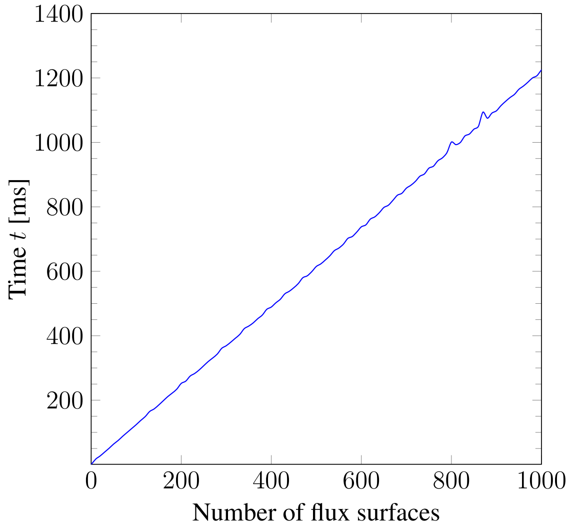

Figure B.1: Total runtime for computing the generalized Spitzer function at constant poloidal and toroidal angle for n different flux surfaces.

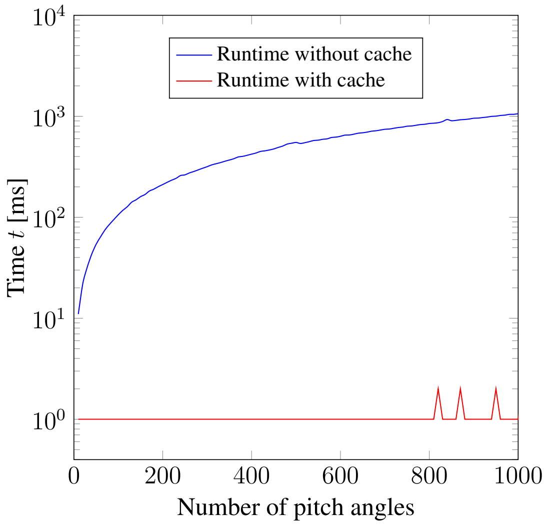

Figure B.2: Total runtime for computing the generalized Spitzer function for one constant spatial point and different velocities with and without caching mechanism.

List of Figures

2.1 Basis functions based on Sonine polynomials (Eq. (2.176)) as functions of the normalized velocity module and their derivatives with respect to x. 49

2.2 B-splines of order $k = 2$ (hat functions) as functions of the normalized velocity module and their derivatives with respect to x. The second derivative is not continues and therefore not shown. 52

2.3 B-splines of order $k = 3$ (quadratic B-splines) as functions of the normalized velocity module and their derivatives with respect to x. 53

2.4 B-splines of order $k = 4$ (cubic B-splines) as functions of the normalized velocity module and their derivatives with respect x. 54

2.5 B-splines of order $k = 4$ (cubic B-splines) defined up to $x = 4$ as functions of the normalized velocity module with subsequent Taylor expansion and their derivatives with respect to the normalized velocity module. . 55

3.1 Distribution of adaptively refined η-levels along the field line at collisionality $L_c/l_c = 1$ (left) and $L_c/l_c = 10^{-3}$ (right) in a standard configuration (upper plots) and a high-mirror configuration (lower plots) of Wendelstein 7-X. Ripple boundaries and toroidal field period boundaries are depicted as vertical solid and dashed lines, respectively. Local field minima of $\hat{B} = B/B_{\mathrm{ref}}$ are indicated as green dots, while local field maxima are indicated as red circles. 65

3.2 Total number of toroidal field periods N_t as a function of the normalized toroidal flux s. The gray band indicates the intended lower and upper limits, respectively, for precomputation. (From G. Kapper, et al. [1]) . 67

3.3 Depiction of precomputed data points (●) by NEO-2 on a single flux surface. An arbitrary point of interest (×) is shown, where the required data points for interpolation are highlighted (○). The non-equal spacing of the data points is a consequence of the adaptive level placement in NEO-2 as can be seen from Figure 3.1. (From G. Kapper, et al. [1]) . . 69

4.1 Normalized mono-energetic radial transport coefficient $D^{\star}_{11}$ (left) and normalized mono-energetic bootstrap current coefficient $D^{\star}_{31}$ (right) as a function of collisionality computed by NEO-2 (solid) for finite collisionalities and by NEO (dotted) for the collisionless limit at half radius $s = 0.25$ (circles) and quarter radius $s = 0.0625$ (crosses). Markers on the solid lines correspond to results of NEO-2 runs at given collisionalities. (From W. Kernbichler, et al. [2]) 74

4.2 Odd part of the gradient driven distribution function, g^a_1, at the position on the field line between distinct maxima computed with adaptive (●) and corresponding equidistant (○) grid as a function of $\hat{B}\eta$ where $\hat{B} = B/B_{\text{ref}}$. The η-level positions are depicted as circles on top of the corresponding curves. Value $\hat{B}\eta = 1$ corresponds to particles reflected at the observation point and the trapped-passing boundary is shown with a vertical dashed line. (From W. Kernbichler, et al. [2]) 75

4.3 Normalized mono-energetic bootstrap current coefficient $D^{\star}_{31}$ for collisionality $\nu^{\star} = 3.66 \cdot 10^{-6}$ at half radius as a function of the number of equidistant η-levels compared to the solution using an adaptive grid. For the adaptive grid a mean number of levels along the field line is indicated as vertical dotted line. In addition the normalized peak memory requirements and normalized runtime with respect to a run with adaptively placed levels is given. (From W. Kernbichler, et al. [2]) . . . 76

4.4 Convergence of the NEO-2 solution (solid lines) for the generalized Spitzer function with respect to the number of Sonine polynomials as a function of the normalized velocity $x = v/v_T$ at pitch angle $\lambda = 1$ for the model tokamak. In addition the collisionless limit computed by SYNCH (dashed line) is shown for comparison. 78

4.5 Same as in Figure 4.4 but computed with cubic B-splines defined in domain $0 \leqslant x \leqslant 4$ (left) and defined in domain $0 \leqslant x \leqslant 5$ (right) with subsequent Taylor expansion for both. 79

4.6 Generalized Spitzer function as a function of the pitch angle parameter $\lambda = v_\parallel/v$ at the field maximum of the model tokamak for particles at velocities $x = 1$, $x = 3$, and $x = 5$ (from top to bottom). The NEO-2 results (solid lines) have been computed with Sonine polynomials. Results in the collisionless limit from SYNCH (dashed lines) are shown for comparison. 80

4.7 Same as in Figure 4.6 but computed with cubic B-splines defined in the domain $0 \leqslant x \leqslant 4$ (left) and defined in domain $0 \leqslant x \leqslant 5$ (right) with subsequent Taylor expansion for both. 81

4.8 Generalized Spitzer function as a function of the pitch angle parameter $\lambda = v_\parallel/v$ at the field minimum of the model tokamak for particles at velocities $x = 1$, $x = 3$, and $x = 5$ (from top to bottom). The NEO-2 results (solid lines) have been computed with Sonine polynomials. Results in the collisionless limit from SYNCH (dashed lines) are shown for comparison. 82

4.9 Same as in Figure 4.8 but computed with cubic B-splines defined in the domain $0 \leqslant x \leqslant 4$ (left) and defined in domain $0 \leqslant x \leqslant 5$ (right) with subsequent Taylor expansion for both. 83

4.10 Convergence of the NEO-2 solution (solid lines) for the generalized Spitzer function with respect to the number of Sonine polynomials (left) and the number of cubic B-splines (right) as a function of the normalized velocity $x = v/v_T$ at pitch angle $\lambda = 1$ for the model tokamak. In addition, the classical Spitzer function (dashed line) is shown for comparison. 85

4.11 Generalized Spitzer function vs. pitch angle computed close to the magnetic axis with NEO-2 (solid lines) where the solution is expanded in terms of Sonine polynomials (left) and cubic B-splines (right) for particles with thermal velocity. The classical Spitzer is shown for comparison (dashed line). 85

4.12 Upper plot - Normalized magnetic field module in a model tokamak (left) and in a standard configuration of Wendelstein 7-X (right) as a function of the distance along the field line φ_s on flux surface $s = 0.25$ (half radius). Lower plot - Distribution of the magnetic field module on flux surface $s = 0.25$ for the same devices as a function of the toroidal (φ_b) and poloidal (ϑ_b), angle. Colored points depict various spatial observation points of interest. N is the number of toroidal field periods which is 1 for the tokamak and 5 for Wendelstein 7-X. 87

4.13 Generalized Spitzer function (left) and its derivative with respect to the perpendicular velocity (right) in a model tokamak as a function of the pitch angle parameter for fixed particle velocities ($x = 0.5$, $x = 1.0$, and $x = 3.0$ from top to bottom) at various observation points as depicted as colored dots in Figure 4.12. Curves from NEO-2 and SYNCH are depicted as solid and dashed lines, respectively. 88

4.14 Generalized Spitzer function (left) and its derivative with respect to the perpendicular velocity (right) in a standard configuration of Wendelstein 7-X as a function of the pitch angle parameter for fixed particle velocities ($x = 0.5$, $x = 1.0$, and $x = 3.0$ from top to bottom) at various observation points as depicted as colored dots in Figure 4.12. Curves from NEO-2 and SYNCH are depicted as solid and dashed lines, respectively. 89

4.15 Generalized Spitzer function as a function of the dimensionless momentum module x for a model tokamak for particles at the global minimum point with pitch angle parameter $\lambda = v_{\|}/v = 1$ and plasma collisionality $L_c/l_c = 10^{-3}$ in the non-relativistic limit ($T = 1\,\mathrm{eV}$) computed by NEO-2 (solid lines) using the collision operator based on Trubnikov and Rosenbluth (T-R), Braams and Karney (B-K), and direct evaluation of Beliaev and Budker (B-B), respectively, and computed by SYNCH (dashed line). 91

4.16 Generalized Spitzer function as a function of the dimensionless momentum module x for a high-mirror configuration of Wendelstein 7-X for particles at the global minimum point with pitch angle parameter $\lambda = v_\parallel/v = 1$ and plasma collisionality $L_c/l_c = 10^{-3}$ in the non-relativistic limit ($T = 1\,\mathrm{eV}$) computed by NEO-2 (solid lines) using the collision operator based on Trubnikov and Rosenbluth (T-R), Braams and Karney (B-K), and direct evaluation of Beliaev and Budker (B-B), respectively, and computed by SYNCH (dashed line). 91

4.17 Generalized Spitzer function as a function of the dimensionless momentum module x computed for a model tokamak with circular flux surfaces for particles at the global minimum point with temperatures $T = 50\,\mathrm{keV}$ (left) and $T = 100\,\mathrm{keV}$, both with the same plasma collisionality $L_c/l_c = 10^{-3}$, and a pitch angle parameter $\lambda = x_\parallel/x = 1$ using the relativistic collision operators (solid lines) based on Braams and Karney (B-K), and based on direct evaluation of Beliaev and Budker (B-B), respectively. As a benchmark the result of the fully relativistic solver SYNCH (dashed line) is plotted. 92

4.18 The same as in Figure 4.17 but for a high-mirror configuration of Wendelstein 7-X. 92

4.19 Generalized Spitzer function as a function of the dimensionless momentum module x computed for a model tokamak with circular flux surfaces at the global minimum point at various temperatures, however with same plasma collisionality $L_c/l_c = 10^{-3}$, with pitch angle parameter $\lambda = x_\parallel/x = 1$ using the fully relativistic collision operator in NEO-2 obtained by direct evaluation of Beliaev and Budker (solid). As a benchmark the results in the collisionless limit of the fully relativistic code SYNCH (dashed) are given. 93

4.20 The same as in Figure 4.19 but for a high-mirror configuration of Wendelstein 7-X. 94

4.21 Generalized Spitzer function for various temperatures and same plasma collisionality $L_c/l_c = 10^{-3}$ computed with NEO-2 (solid) and SYNCH (dashed) at the global minimum point of a model tokamak with circular flux surfaces for particles with $x = 1$ (left) and $x = 3$ (right). 94

4.22 The same as in Figure 4.21 but at the global maximum point. 95

5.1 Plasma parameter profiles computed by the transport code NTSS [62] and the rotational transform ι as functions of the normalized toroidal flux s. (From G. Kapper, et al. [1]) 101

5.2 Magnetic field module at flux surface $s = 0.25$ as function of Boozer angles ($N = 5$ for Wendelstein 7-X). (From G. Kapper, et al. [1]) 102

5.3 Generalized Spitzer function for finite collisionality computed by NEO-2 (solid) and for the collisionless limit computed by SYNCH (dashed) as a function of the pitch parameter $\lambda = v_\parallel/v$. Line colors correspond to respective marker colors in Figure 5.2. (From G. Kapper, et al. [1]) . . 102

5.4 Pitch-angle integral in the trapped domain of the generalized Spitzer function (5.1) for velocity values $v = v_T$ (left) and $v = 3v_T$ (right) as functions of Boozer angles on flux surface $s = 0.25$. (From G. Kapper, et al. [1]) 104

5.5 X2-mode - Total absorbed power (upper plane) and total driven current (lower plane) of a beam with 1 MW input power as functions of the toroidal (β) and poloidal (α) launch angle by passing particles (left) and trapped particles (right). Two particular launch angles, depicted as X2a and X2b, are then studied in more detail. (From G. Kapper, et al. [1]) 107

5.6 Scenario X2a - Locally absorbed power dP/dl (left) and locally driven current dI/dl (right) for the finite collisionality and the collisionless case as functions of the distance along the central ray l. Contributions of passing and trapped particles are depicted as dashed and dotted lines, respectively. The cold resonance position is marked with a thick vertical line. (From G. Kapper, et al. [1]) 108

5.7 Scenario X2a - Current density integral kernel (5.6) as a function of the parallel and perpendicular normalized velocities for finite collisionality (left) and for the collisionless limit (right). The three numbered resonance lines correspond to respective positions indicated by numbered vertical lines in Figure 5.6. The trapped-passing boundary is shown by dashed lines. Colors are supersaturated in order to clarify the different signs of kernel F in different regions. (From G. Kapper, et al. [1]) 109

5.8 Scenario X2a - The left plot shows the total driven current within the volume enclosed by a given flux surface s for finite collisionality and in the mean free path regime (Left plot from G. Kapper, et al. [1]). The right plot shows an estimation of the influence of ECCD on the rotational transform profile, where the equilibrium value of ι is shown as dotted line. Resonances are indicated as horizontal dashed lines. . . 109

5.9 Scenario X2b - Locally absorbed power dP/dl (left) and locally driven current dI/dl (right) for the finite collisionality and the collisionless case as functions of the distance along the central ray l. Contributions of passing and trapped particles are depicted as dashed and dotted lines, respectively. The cold resonance position is marked with a thick vertical line. (From G. Kapper, et al. [1]) 110

5.10 Scenario X2b - Current density integral kernel (5.6) as a function of the parallel and perpendicular normalized velocities for finite collisionality (left) and for the collisionless limit (right). The three numbered resonance lines correspond to respective positions indicated by numbered vertical lines in Figure 5.9. The trapped-passing boundary is shown by dashed lines. Colors are supersaturated in order to clarify the different signs of kernel F in different regions. (From G. Kapper, et al. [1]) 111

5.11 Scenario X2b - The left plot shows the total driven current within the volume enclosed by a given flux surface s for finite collisionality and in the mean free path regime. (Left plot from G. Kapper, et al. [1]) The right plot shows an estimation of the influence of ECCD on the rotational transform profile, where the equilibrium value of ι is shown as dotted line. Resonances are indicated as horizontal dashed lines. . . 111

5.12 Absorbed power (left) and total driven current (right) of a X2-beam with 1 MW input power by passing (dashed) and trapped (dotted) particles as functions of the toroidal launch angle β at fixed poloidal angle $\alpha = 18.75$ deg. (From G. Kapper, et al. [1]) 112

5.13 O2-mode - Total absorbed power (upper plane) and total driven current (lower plane) of a beam with 1 MW input power as functions of the toroidal (β) and poloidal (α) launch angle by passing particles (left) and trapped particles (right). Two particular launch angles, depicted as O2a and O2b, are then studied in more detail. (From G. Kapper, et al. [1]) 113

5.14 Scenario O2a - Locally absorbed power dP/dl (left) and locally driven current dI/dl (right) for the finite collisionality and the collisionless case as functions of the distance along the central ray l. Contributions of passing and trapped particles are depicted as dashed and dotted lines, respectively. The cold resonance position is marked with a thick vertical line. (From G. Kapper, et al. [1]) 115

5.15 Scenario O2a - Current density integral kernel (5.6) as a function of the parallel and perpendicular normalized velocities for finite collisionality (left) and for the collisionless limit (right). The three numbered resonance lines correspond to respective positions indicated by numbered vertical lines in Figure 5.14. The trapped-passing boundary is shown by dashed lines. Colors are supersaturated in order to clarify the different signs of kernel F in different regions. (From G. Kapper, et al. [1]) 115

5.16 Scenario O2a - The left plot shows the total driven current within the volume enclosed by a given flux surface s for finite collisionality and in the mean free path regime. (Left plot G. Kapper, et al. [1]) The right plot shows an estimation of the influence of ECCD on the rotational transform profile, where the equilibrium value of ι is shown as dotted line. Resonances are indicated as horizontal dashed lines. 116

5.17 Scenario O2b - Locally absorbed power dP/dl (left) and locally driven current dI/dl (right) for the finite collisionality and the collisionless case as functions of the distance along the central ray l. Contributions of passing and trapped particles are depicted as dashed and dotted lines, respectively. The cold resonance position is marked with a thick vertical line. (From G. Kapper, et al. [1]) 117

5.18 Scenario O2b - Current density integral kernel (5.6) as a function of the parallel and perpendicular normalized velocities for finite collisionality (left) and for the collisionless limit (right). The three numbered resonance lines correspond to respective positions indicated by numbered vertical lines in Figure 5.17. The trapped-passing boundary is shown by dashed lines. Colors are supersaturated in order to clarify the different signs of kernel F in different regions. (From G. Kapper, et al. [1]) 118

5.19 Scenario O2b - The left plot shows the total driven current within the volume enclosed by a given flux surface s for finite collisionality and in the mean free path regime (Left plot from G. Kapper, et al. [1]). The right plot shows an estimation of the influence of ECCD on the rotational transform profile, where the equilibrium value of ι is shown as dotted line. Resonances are indicated as horizontal dashed lines. . . 118

5.20 Left plot - Locally driven current dI/dl as function of the distance along the central ray l computed in the non-relativistic limit (red lines) and computed with a fully relativistic collision model (green). Contributions of passing and trapped particles are depicted as dashed and dotted lines, respectively. The cold resonance position is marked with a thick vertical line. Right plot - Total driven current within the volume enclosed by a given flux surface s computed in the non-relativistic limit (red line) and computed with a fully relativistic collision model (green line). 121

B.1 Total runtime for computing the generalized Spitzer function at constant poloidal and toroidal angle for n different flux surfaces. 142

B.2 Total runtime for computing the generalized Spitzer function for one constant spatial point and different velocities with and without caching mechanism. 142

References

[1] G. Kapper, S. V. Kasilov, W. Kernbichler, A. F. Martitsch, M. F. Heyn, N. B. Marushchenko, and Y. Turkin, “Electron cyclotron current drive simulations for finite collisionality plasmas in Wendelstein 7-X using the full linearized collision model”, Physics of Plasmas **23**, 112511 (2016).

[2] W. Kernbichler, S. V. Kasilov, G. Kapper, A. F. Martitsch, V. V. Nemov, C. Albert, and M. F. Heyn, “Solution of drift kinetic equation in stellarators and tokamaks with broken symmetry using the code NEO-2”, Plasma Physics and Controlled Fusion **58**, 104001 (2016).

[3] A. F. Martitsch, S. V. Kasilov, W. Kernbichler, G. Kapper, C. G. Albert, M. F. Heyn, H. M. Smith, E. Strumberger, S. Fietz, W. Suttrop, M. Landreman, the ASDEX Upgrade Team, and the EUROfusion MST1 Team, “Effect of 3D magnetic perturbations on the plasma rotation in ASDEX Upgrade”, Plasma Physics and Controlled Fusion **58**, 074007 (2016).

[4] C. G. Albert, M. F. Heyn, G. Kapper, S. V. Kasilov, W. Kernbichler, and A. F. Martitsch, “Evaluation of toroidal torque by non-resonant magnetic perturbations in tokamaks for resonant transport regimes using a Hamiltonian approach”, Physics of Plasmas **23**, 082515 (2016).

[5] G. Kapper, W. Kernbichler, S. V. Kasilov, and N. B. Marushchenko, “Modeling of electron cyclotron current drive for finite collisionality plasmas in Wendelstein 7-X”, in 42nd EPS Conference on Plasma Physics, Vol. 39E (2015), P1.164.

[6] C. G. Albert, M. F. Heyn, G. Kapper, S. V. Kasilov, W. Kernbichler, and A. F. Martitsch, “Hamiltonian approach for evaluation of toroidal torque from finite amplitude non-axisymmetric perturbations of a tokamak magnetic field in resonant transport regimes”, in *43rd EPS Conference on Plasma Physics* (2016), P1.051.

[7] W. Kernbichler, G. Kapper, S. V. Kasilov, and N. B. Marushchenko, “Computation of the Spitzer function in stellarators and tokamaks with finite collisionality”, EPJ Web of Conferences **87**, 01006 (2015).

[8] A. Dinklage, T. Klinger, G. Marx, and L. Schweikhard, *Plasma Physics: Confinement, Transport and Collective Effects*, Vol. 670 (Springer Science & Business Media, 2005).

[9] A. J. Webster, “Fusion: Power for the future”, Physics education **38**, 135 (2003).

[10] C. F. v. Weizsäcker, “Zur Theorie der Kernmassen”, Zeitschrift für Physik **96**, 431–458 (1935).

[11] N. J. Fisch and A. H. Boozer, “Creating an Asymmetric Plasma Resistivity with Waves”, Physical Review Letters **45**, 720–722 (1980).

[12] S. V. Kasilov and W. Kernbichler, “Passive cyclotron current drive efficiency for relativistic toroidal plasmas”, Physics of Plasmas **3**, 4115–4127 (1996).

[13] L. Spitzer and R. Härm, “Transport Phenomena in a Completely Ionized Gas”, Physical Review **89**, 977–981 (1953).

[14] Y. R. Lin-Liu, V. S. Chan, F. L. Hinton, and S. K. Wong, “Collisionality effects on electron cyclotron current drive efficiency”, AIP Conference Proceedings **595**, 438–441 (2001).

[15] H. Maaßberg, C. D. Beidler, and N. B. Marushchenko, “Electron cyclotron current drive modelling with parallel momentum correction for tokamaks and stellarators”, Physics of Plasmas **19**, 102501 (2012).

[16] Y. R. Lin-Liu, V. S. Chan, T. C. Luce, R. Prater, O. Sauter, and R. W. Harvey, “Modeling of electron cyclotron current drive experiments on DIII-D”, AIP Conference Proceedings **485**, 249–252 (1999).

[17] P. Helander and P. J. Catto, “Neoclassical current drive by waves with a symmetric spectrum”, Physics of Plasmas **8**, 1988–1994 (2001).

[18] W. Kernbichler, S. V. Kasilov, G. O. Leitold, V. V. Nemov, and N. B. Marushchenko, “Generalized Spitzer Function with Finite Collisionality in Toroidal Plasmas”, Contributions to Plasma Physics **50**, 761–765 (2010).

[19] B. J. Braams and C. F. F. Karney, “Conductivity of a relativistic plasma”, Physics of Fluids B: Plasma Physics **1**, 1355–1368 (1989).

[20] S. T. Beliaev and G. I. Budker, “The relativistic kinetic equation”, in Soviet Phys.(Doklady), Vol. 1 (1956), p. 218.

[21] T. M. Antonsen and K. R. Chu, “Radio frequency current generation by waves in toroidal geometry”, Physics of Fluids **25**, 1295–1296 (1982).

[22] N. B. Marushchenko, Y. Turkin, and H. Maaßberg, “Ray-tracing code TRAVIS for ECR heating, EC current drive and ECE diagnostic”, Computer Physics Communications **185**, 165–176 (2014).

[23] J. Nührenberg and R. Zille, “Stable stellarators with medium β and aspect ratio”, Physics Letters A **114**, 129–132 (1986).

[24] J. Geiger, C. D. Beidler, Y. Feng, H. Maaßberg, N. B. Marushchenko, and Y. Turkin, “Physics in the magnetic configuration space of W7-X”, Plasma Physics and Controlled Fusion **57**, 014004 (2015).

[25] T. Klinger et al., “Performance and properties of the first plasmas of Wendelstein 7-X”, Plasma Physics and Controlled Fusion **59**, 014018 (2017).

[26] P. Helander and D. J. Sigmar, *Collisional transport in magnetized plasmas*, Vol. 4 (Cambridge University Press, 2005).

[27] F. Scheck, *Theoretische Physik 1* (Springer-Verlag Berlin Heidelberg, 2003).

[28] B. A. Trubnikov, “Particle interactions in a fully ionized plasma”, Reviews of Plasma Physics **1**, 105 (Consultants Bureau, New York, 1965).

[29] R. G. Littlejohn, “Variational principles of guiding centre motion”, Journal of Plasma Physics **29**, 111–125 (1983).

[30] P. Leitner, “Impact of Energy and Momentum Conservation on Fluid Resonances in the Kinetic Modelling of the Interaction of Resonant Magnetic Perturbations with a Tokamak Plasma”, PhD thesis (Institute of Theoretical and Computational Physics, Graz University of Technology, 2015).

[31] A. F. Martitsch, “Modeling of Plasma Rotation in Tokamaks”, PhD thesis (Institute of Theoretical and Computational Physics, Graz University of Technology, 2016).

[32] W. D. D’Haeseleer, *Flux Coordinates and Magnetic Field Structure: A Guide to a Fundamental Tool of Plasma Theory*, 1991.

[33] A. I. Morozov and L. S. Solov’ev, “The structure of magnetic fields”, in *Reviews of Plasma Physics*, Vol. 2 (Consultants Bureau, New York, 1966), pp. 1–101.

[34] F. L. Hinton and R. D. Hazeltine, “Theory of plasma transport in toroidal confinement systems”, Rev. Mod. Phys. **48**, 239–308 (1976).

[35] W. Kernbichler, S. V. Kasilov, V. V. Nemov, G. Leitold, and M. F. Heyn, “Evaluation of the Bootstrap Current in Stellarators”, AIP Conference Proceedings **669**, 492–495 (2003).

[36] V. V. Nemov, S. V. Kasilov, W. Kernbichler, and M. F. Heyn, “Evaluation of $1/\nu$ neoclassical transport in stellarators”, Physics of Plasmas **6**, 4622–4632 (1999).

[37] S. V. Kasilov, W. Kernbichler, A. F. Martitsch, H. Maassberg, and M. F. Heyn, “Evaluation of the toroidal torque driven by external non-resonant non-axisymmetric magnetic field perturbations in a tokamak”, Physics of Plasmas **21**, 092506 (2014).

[38] S. I. Braginskii, “Transport Processes in Plasma”, in *Reviews of Plasma Physics*, Vol. 1 (Consultants Bureau, New York, 1965), pp. 205–311.

[39] W. Kernbichler, S. V. Kasilov, G. O. Leitold, V. V. Nemov, and K. Allmaier, “Recent Progress in NEO-2 – A Code for Neoclassical Transport Computations Based on Field Line Tracing”, Plasma and Fusion Research **3**, S1061–S1061 (2008).

[40] G. O. Leitold, “Computation of neoclassical transport coefficients and generalized Spitzer function in toroidal fusion plasmas”, PhD thesis (Institute of Theoretical and Computational Physics, Graz University of Technology, 2010).

[41] C. de Boor, *A Practical Guide to Splines*, Vol. 27 (Springer-Verlag New York, 1978).

[42] C. de Boor, “On calculating with B-splines”, Journal of Approximation Theory **6**, 50–62 (1972).

[43] M. N. Rosenbluth, W. M. MacDonald, and D. L. Judd, “Fokker-Planck equation for an inverse-square force”, Physical Review **107**, 1 (1957).

[44] S. V. Kasilov, *Direct evaluation of Beliaev/Budker*, Personal communication, 2016.

[45] The HDF Group, *Hierarchical Data Format, version 5*, (1997-2016) `http://www.hdfgroup.org/HDF5/`.

[46] G. Kapper, “Development of a library for parallel computation of physical problems and its application to plasma physics”, Master Thesis (Graz University of Technology, 2013).

[47] Message Passing Interface Forum, *MPI: A Message-Passing Interface Standard*, tech. rep. (Version 2.2, September 2009).

[48] G. M. Amdahl, “Validity of the Single Processor Approach to Achieving Large Scale Computing Capabilities”, in Proceedings of the April 18-20, 1967, Spring Joint Computer Conference, AFIPS ’67 (Spring) (1967), pp. 483–485.

[49] X.-H. Sun and Y. Chen, “Reevaluating Amdahl’s law in the multicore era”, Journal of Parallel and Distributed Computing **70**, 183–188 (2010).

[50] C. D. Beidler, K. Allmaier, M. Y. Isaev, S. V. Kasilov, W. Kernbichler, G. O. Leitold, H. Maaßberg, D. R. Mikkelsen, S. Murakami, M. Schmidt, D. A. Spong, V. Tribaldos, and A. Wakasa, “Benchmarking of the mono-energetic transport coefficients-results from the International Collaboration on Neoclassical Transport in Stellarators (ICNTS)”, Nuclear Fusion **51**, 076001 (2011).

[51] K. C. Shaing and J. D. Callen, “Neoclassical flows and transport in nonaxisymmetric toroidal plasmas”, Phys. Fluids **28**, 3315–3326 (1983).

[52] N. Nakajima, M. Okamoto, J. Todoroki, Y. Nakamura, and M. Wakatani, “Optimization of the bootstrap current in a large helical system with $L = 2$”, Nuclear Fusion **29**, 605–616 (1989).

[53] A. H. Boozer and H. J. Gardner, “The bootstrap current in stellarators”, Phys. Fluids B **2**, 2408–2421 (1990).

[54] L. Spitzer Jr., “The Stellarator Concept”, The Physics of Fluids **1**, 253–264 (1958).

[55] G. Grieger, W. Lotz, P. Merkel, J. Nührenberg, J. Sapper, E. Strumberger, H. Wobig, R. Burhenn, V. Erckmann, U. Gasparino, L. Giannone, H. J. Hartfuss, R. Jaenicke, G. Kühner, H. Ringler, A. Weller, F. Wagner, the W7–X Team, and the W7–AS Team, “Physics optimization of stellarators”, Physics of Fluids B **4**, 2081–2091 (1992).

[56] T. Rummel, K. Ribe, G. Ehrke, K. Rummel, A. John, T. Monnich, K. P. Buscher, W. H. Fietz, R. Heller, O. Neubauer, and A. Panin, “The Superconducting Magnet System of the Stellarator Wendelstein 7-X”, IEEE Transactions on Plasma Science **40**, 769–776 (2012).

[57] T. Sunn Pedersen, M. Otte, S. Lazerson, P. Helander, S. Bozhenkov, C. Biedermann, T. Klinger, R. Wolf, H.-S. Bosch, and the Wendelstein 7-X team, “Confirmation of the topology of the Wendelstein 7-X magnetic field to better than 1: 100,000”, Nature Communications **7** (2016).

[58] A. Dinklage, A. Alonso, J. Baldzuhn, C. Beidler, C. Biedermann, B. Blackwell, S. Bozhenkov, R. Brakel, B. Buttenschön, Y. Feng, et al., “Core Confinement in Wendelstein 7-X Limiter Plasmas”, in 43rd EPS Conference on Plasma Physics (European Physical Society, 2016), O2.107.

[59] Y. Feng, M. Kobayashi, T. Lunt, and D. Reiter, “Comparison between stellarator and tokamak divertor transport”, Plasma Physics and Controlled Fusion **53**, 024009 (2011).

[60] M. Romé, V. Erckmann, U. Gasparino, and N. Karulin, “Electron cyclotron resonance heating and current drive in the W7-X stellarator”, Plasma Physics and Controlled Fusion **40**, 511 (1998).

[61] V. Erckmann, P. Brand, H. Braune, G. Dammertz, G. Gantenbein, W. Kasparek, H. P. Laqua, H. Maaßberg, N. B. Marushchenko, G. Michel, M. Thumm, Y. Turkin, M. Weissgerber, A. Weller, and the W7–X ECRH–teams at IPP Greifswald, FZK Karlsruhe and IPF Stuttgart, “Electron cyclotron heating for W7-X: physics and technology”, Fusion Science and Technology **52**, 291–312 (2007).

[62] Y. Turkin, C. D. Beidler, H. Maaßberg, S. Murakami, V. Tribaldos, and A. Wakasa, “Neoclassical transport simulations for stellarators”, Physics of Plasmas **18**, 022505 (2011).

[63] S. P. Hirshman and J. C. Whitson, “Steepest-descent moment method for three-dimensional magnetohydrodynamic equilibria”, Physics of Fluids **26**, 3553–3568 (1983).

[64] N. B. Marushchenko, C. D. Beidler, S. V. Kasilov, W. Kernbichler, H. Maaßberg, R. Prater, and R. W. Harvey, “Electron cyclotron current drive in low collisionality limit: On parallel momentum conservation”, Physics of Plasmas **18**, 032501 (2011).

[65] M. Bornatici, R. Cano, O. D. Barbieri, and F. Engelmann, “Electron cyclotron emission and absorption in fusion plasmas”, Nuclear Fusion **23**, 1153 (1983).

[66] S. P. Hirshman, K. C. Shaing, W. I. van Rij, C. O. Beasley, and E. C. Crume, “Plasma transport coefficients for nonsymmetric toroidal confinement systems”, Physics of Fluids **29**, 2951–2959 (1986).

[67] N. Marushchenko, C. Beidler, V. Erckmann, J. Geiger, P. Helander, H. Laqua, H. Maassberg, and Y. Turkin, "ECRH and ECCD scenarios for W7-X", in EPJ Web of Conferences, Vol. 32 (EDP Sciences, 2012), p. 01004.

[68] R. H. Cohen, "Effect of trapped electrons on current drive", Physics of Fluids **30**, 2442–2449 (1987).

[69] T. Ohkawa, "Steady state operation of tokamaks by RF heating", General Atomics Report GA-A13847 (1976).

[70] P. Strand and W. Houlberg, "Magnetic flux evolution in highly shaped plasmas", Physics of Plasmas **8**, 2782–2792 (2001).

[71] T. Sunn Pedersen, A. Dinklage, Y. Turkin, R. Wolf, S. Bozhenkov, J. Geiger, G. Fuchert, H.-S. Bosch, K. Rahbarnia, H. Thomsen, U. Neuner, T. Klinger, A. Langenberg, H. T. Mora, P. Kornejew, J. Knauer, M. Hirsch, and N. Pablant, "Key results from the first plasma operation phase and outlook for future performance in Wendelstein 7-X", Physics of Plasmas **24**, 055503 (2017).

[72] V. Erckmann, W. Kasparek, G. Müller, P. Schüller, M. Thumm, et al., "Electron cyclotron resonance heating transmission line and launching system for the Wendelstein VII-AS stellarator", Fusion Science and Technology **17**, 76–85 (1990).

[73] V. Erckmann and U. Gasparino, "Electron cyclotron resonance heating and current drive in toroidal fusion plasmas", Plasma physics and controlled fusion **36**, 1869 (1994).

[74] V. Erckmann, H. Laqua, H. Maassberg, J. Geiger, G. Dammertz, W. Kasparek, M. Thumm, et al., "Electron cyclotron resonance heating and EC-current drive experiments at W7-AS, status at W7-X", Fusion engineering and design **53**, 365–375 (2001).

[75] N. J. Fisch, "Theory of current drive in plasmas", Reviews of Modern Physics **59**, 175 (1987).

[76] J. D. Jackson, *Classical Electrodynamics*, Second (Wiley, 1999).

[77] E. W. Hobson, *The theory of spherical and ellipsoidal harmonics* (CUP Archive, 1931).

[78] S. K. Wong, "Matrix elements of the linearized Fokker–Planck operator", Physics of Fluids **28**, 1695–1701 (1985).